UPPSALA
UNIVERSITET

Topological superconductivity in multiorbital materials

JOHANN SCHMIDT

Dissertation presented at Uppsala University to be publicly examined in Häggsalen, Ångströmlaboratoriet, Lägerhyddsvägen 1, Uppsala, Friday, 20 November 2020 at 13:15 for the degree of Doctor of Philosophy. The examination will be conducted in English. Faculty examiner: Professor Karyn Le Hur (Ecole Polytechnique, CNRS).

Abstract
Schmidt, J. 2020. Topological superconductivity in multiorbital materials. *Digital Comprehensive Summaries of Uppsala Dissertations from the Faculty of Science and Technology* 1973. 137 pp. Uppsala: Acta Universitatis Upsaliensis. ISBN 978-91-513-1022-0.

Multiorbital materials add a new intricacy to the already complex phenomenon of superconductivity. The additional orbital degree of freedom requires leaving behind the established band picture, but also opens the possibility of more complicated order parameters with new properties. This thesis summarizes theoretical studies of two examples of multiorbital superconductors.

The first part focuses on superconductivity in Kitaev materials. The unusual interactions in these materials are shown to give rise to spin triplet superconducting pairing on both two-and three-dimensional lattice structures. A symmetry characterization enables the analysis of the stable superconducting order parameters, revealing several nodal states on the 3D harmonic honeycomb lattices and a competition between nematic and chiral superconductivity on the 2D honeycomb lattice. The following topological classification uncovers a number of topologically non-trivial superconducting states protected by various symmetries, giving rise to flat bands, Fermi arcs, or dispersing Majorana excitations on their surface.

The thesis' second part spotlights odd-frequency superconductivity in a doped topological insulator. An experimentally supported uncommon interorbital order parameter gives rise to large intraorbital odd-frequency pairing. A calculation of the Meissner effect unveils an unexpected diamagnetic odd-frequency Meissner response, stabilizing superconductivity.

The results of this thesis highlight the diverse nature of superconductivity in multiorbitalmaterials and stimulate further research on its topological properties and stability.

Keywords: Superconductivity, Kitaev materials, Odd-frequency superconductivity, Topological superconductivity

Johann Schmidt, Department of Physics and Astronomy, Materials Theory, Box 516, Uppsala University, SE-751 20 Uppsala, Sweden.

*It is invaluable to have a friend who shares your interests
and helps you stay motivated.*
Maryam Mirzakhani

List of papers

This thesis is based on the following papers, which are referred to in the text by their Roman numerals.

I **From chiral d-wave to nodal line superconductivity in the harmonic honeycomb lattices**
Johann Schmidt, Adrien Bouhon, and Annica M. Black-Schaffer
*Physical Review B **94**, 104513 (2016)*

II **Topological superconductivity in the extended Kitaev-Heisenberg model**
Johann Schmidt, Daniel D. Scherer, and Annica M. Black-Schaffer
*Physical Review B **97**, 014504 (2018)*

III **Topological nodal superconducting phases and topological phase transition in the hyperhoneycomb lattice**
Adrien Bouhon, Johann Schmidt, and Annica M. Black-Schaffer
*Physical Review B **97**, 104508 (2018)*

IV **Odd-frequency superconductivity and Meissner effect in the doped topological insulator Bi_2Se_3**
Johann Schmidt, Fariborz Parhizgar, and Annica M. Black-Schaffer
*Physical Review B **101**, 180512(R) (2020)*

V **Topological nodal superconductivity arising from the extended Kitaev-Heisenberg interaction on the hyperhoneycomb lattice**
Johann Schmidt and Annica M. Black-Schaffer
In manuscript

Reprints were made with permission from the publishers.

Author's contributions

   I   Derived the self-consistency equations, wrote the code and ran the numerical calculations, performed the symmetry analysis, interpreted the data with input from the co-authors, main contributor to writing the article.

  II   Formulated the research question with input from co-authors, derived mean-field decoupling and self-consistency equations, wrote the numerical code and performed calculations, carried out symmetry classification and topological analysis, main contributor to writing the article.

 III   Contributed to the symmetry classification and detection of nodal structures, participated in the writing of the article.

 IV   Collaboratively with second author identified odd-frequency pairing correlations and derived equations for the Meissner effect, major contributions to writing the code and running numerical integrations, collaborative interpretation of data, equally contributed to writing of the article.

  V   Contributed to design of the study, derived self-consistency equations, wrote the code and ran numerical calculations, performed symmetry analysis and topological classification, main contributor to writing the article.

Contents

Summary in English

The exciting phenomenon of superconductivity, where a material loses its resistance below a certain critical temperature, has been an active research field for more than 100 years now. Thanks to breakthroughs in the 1950s, simple superconductors in pure metals, such as aluminum or lead, are relatively well understood. Superconductivity in these materials appears from two electrons forming a so-called Cooper pair when a small attraction exists between them. When a large number of Cooper pairs is created, they behave as if they are all coordinated, such that they can be described mathematically by one single wave function. In this sense, superconductivity is a macroscopic manifestation of a microscopic quantum effect. Because all the Cooper pairs act in unison, they can flow without resistance which would appear from the scattering of individual electrons. The combined Cooper pairs also expel an applied magnetic field, something which is known as the Meissner effect. In simple metals, the attraction between two electrons comes from interactions with the vibrations of the crystal lattice, which can overcome the usual electrostatic repulsion. In this case, the two electrons that form the Cooper pair have the same energy, but opposite momentum and spin, which is the microscopic magnetic moment of the electrons.

Things become more complicated in more complex materials. In the high-temperature superconductors found in certain Copper ceramics, for example, the Cooper pairs are believed to be formed by other interactions. Even further complications appear when several orbitals or atomic shells contribute the electrons making up the Cooper pairs, such as in iron-based superconductors. In these cases, the interactions that bind the Cooper pairs together need to be described from a more local viewpoint and need to take into account the orbitals of the electrons. The Cooper pairs arising from such interactions can be more intricate: They will still have opposite momentum, but could involve different orbitals and different combinations of spins. This leads to distinctive properties of the superconductors, such as a special sensitivity to applied fields or defects, or to higher critical temperatures.

When two electrons are bound together in a Cooper pair, a finite energy is required to overcome that attraction and to excite a single electron. In physics, this is called an energy gap, which can be mathematically described by a gap function. The energy gap encompasses the properties of the Cooper pairs in the superconductor and is therefore a key quantity in the physical and mathematical description of superconductivity. In particular, classifying the symmetries of the gap function yields a lot of information about the superconducting

order and the underlying interactions. Symmetries in physics are transformations that leave a system unchanged, just like a clover leaf looks the same when rotated by 120 degrees. For a superconductor the key question is which of the symmetries of the material that becomes superconducting does the gap function retain, and which ones does it break. The breaking of symmetries can have essential outcomes: The energy gap can disappear for certain directions, it can have an angle dependence that is different from that of the underlying material, or it can break time-reversal symmetry, giving rise to small magnetic fields.

In addition to the symmetry of the gap function, recent developments have highlighted the additional importance of the topology of the wave function describing the superconductor. Topology is a mathematical field which classifies which objects can be transformed into each other, and which cannot. A classic example is that a cube can be transformed into a sphere, simply by squeezing it a little, but it cannot be transformed into a torus (the shape of a donut or swim ring), without poking a hole or gluing together some ends. In terms of topology, the cube and the sphere belong to the same class, whereas a cube and a torus belong to different classes. Similarly, superconductors can be in different topological classes, which means that the wave functions describing them cannot be transformed into each other without closing the energy gap or breaking a symmetry. This abstract mathematical concept leads to an important effect: When two superconductors of different topological classes form an interface, the energy gap needs to close on the boundary, because the wave functions cannot be transformed into each other without closing the gap. The same is true for a boundary of a superconductor with any other material in a different topological class, like the vacuum or air. So even though it requires a finite energy to excite a single electron inside a superconductor, topological superconductors will have excitations on the surface that do not cost any energy, because the energy gap is closed on the boundary. These excitations are in some cases envisioned as building blocks for quantum computers insensitive to disturbances, giving a technological motivation to the study of topological superconductors.

In this thesis I theoretically modeled superconductivity arising in certain multiorbital materials. I then analyzed what kind of Cooper pairs are formed, what symmetries they break, and what their topological properties are. The first part focuses on a material class called Kitaev materials. Their defining feature is a special interaction between electrons, that depends strongly on the direction in which two electrons interact. Such peculiar interactions can arise, because some of the atoms in these materials (Iridium or Ruthenium) are so heavy, that effects of the theory of relativity need to be taken into account. This leads to very complex magnetism in the Kitaev materials. Another interesting aspect of Kitaev materials is that they can appear in a layered, effectively two-dimensional structure, or in complex three-dimensional crystals. Together with my co-authors we found that Cooper pairs in Kitaev materials

would be made up of electrons with the same spin of orbitals from neighboring sites. In the three-dimensional lattice structures, the energy gap can disappear for either a whole range of directions, forming so-called nodal lines, or only for specific directions, in nodal points. In the layered two-dimensional structures we discovered a competition of two kinds of superconductivity. Either the energy gap breaks a rotational symmetry (called nematic superconductivity), meaning the gap is larger in only one specific direction, or the gap function breaks time-reversal symmetry (so-called chiral superconductivity), where small magnetic fields would appear. Different topological classes can be assigned to those two cases, giving rise to either pairwise or individual excitations on the surface of the superconductor, respectively.

The second part of the thesis summarizes a work on the material Bi_2Se_3. Experiments found that it becomes superconducting upon doping with certain metals and that the Cooper pairs are most likely formed between two electrons of equal spin coming from different orbitals. In this case we searched for Cooper pairs that are formed between electrons separated in time and are forbidden to exist at equal time. These so-called odd-frequency pairs are known to quite often exist in superconductors with several orbitals when there is also superconductivity from Cooper pairs forming at equal times. Odd-frequency Cooper pairs are in general more complicated than the equal time pairs. In some situations, for example, odd-frequency pairs could form between electrons of equal spins, when the equal time pairs are made from electrons of opposite spin. In our work we predict odd-frequency Cooper pairs to appear in Bi_2Se_3 which are formed between electrons of the same spin in the same orbital, which would be in some sense simpler than the equal time pairs. An unsolved question is how the odd-frequency pairs affect the superconducting pairing of the equal time pairs. One proposal is the paramagnetic Meissner effect, where an external magnetic field is not suppressed, but enhanced. This would be detrimental to superconductivity, because strong magnetic fields break up the Cooper pairs. In Bi_2Se_3 we find that the odd-frequency Cooper pairs also suppress an external magnetic field, which means they are not as bad for superconductivity as previously thought.

Sammanfattning på svenska

Topologisk supraledning i multiorbitala material

Det fascinerande fenomenet supraledning, där ett material tappar sin resistivitet under en viss kritisk temperatur, har varit ett aktivt forskningsfält i mer än 100 år. Tack vare flera genombrott på 1950-talet är enkla supraledare i rena metaller, såsom aluminium eller bly, relativt väl förstådda. Supraledning i dessa material uppstår när två elektroner bildar ett så kallat Cooper-par genom att det finns en liten attraktion mellan dem. När ett stort antal Cooper-par skapas, får de ett samordnat beteende så att de kan beskrivas matematiskt med en enda vågfunktion. Supraledning är därmed en makroskopisk manifestation av en mikroskopisk kvanteffekt. Eftersom alla Cooper-paren agerar ihop, kan de flöda utan det motstånd som annars skulle uppstå vid spridning av enskilda elektroner. De kombinerade Cooper-paren motverkar också ett applicerat magnetfält, något som kallas Meissner-effekten. I enkla metaller uppstår attraktionen mellan två elektroner från interaktioner med kristallgitterets vibrationer, vilket kan övervinna den vanliga elektrostatiska repulsionen. I detta fall har de två elektronerna som bildar Cooper-paret samma energi, men motsatt momentum och spinn, varav det senare är elektronernas mikroskopiska magnetiska moment.

Saker blir mer komplicerade i mer komplexa material. I högtemperatursupraledare som bildas i kopparkeramik antas Cooper-paren till exempel bildas av andra interaktioner. Ytterligare komplikationer uppträder när flera orbitaler eller atomskal bidrar till de elektroner som utgör Cooper-paren, såsom i järnbaserade supraledare. I dessa fall måste interaktionerna som binder ihop Cooper-paren beskrivas från en mer lokal synvinkel och ta hänsyn till elektronernas orbital. Cooper-paren som härrör från sådana interaktioner kan vara mer invecklade: De kommer fortfarande att ha motsatt rörelsemängd, men kan ha olika orbitaler och olika kombinationer av spinn. Detta leder till särskiljande egenskaper hos supraledaren, som exempelvis en annan känslighet för applicerade fält eller defekter, eller högre kritiska temperaturer.

När två elektroner är sammanbundna i ett Cooper-par krävs en ändlig energi för att övervinna denna attraktion och för att excitera en enstaka elektron. I fysik kallas detta ett energigap, vilket matematiskt kan beskrivas av en gapfunktion. Energigapet återspeglar Cooper-parens egenskaper i supraledaren och är därför en huvudkomponent i den fysiska och matematiska beskrivningen av supraledning. I synnerhet ger klassificering av gapfunktionens symmetrier mycket information om supraledningsförmågan och de underliggande interaktionerna. Symmetrier i fysik är transformationer som lämnar ett system

oförändrat, precis som ett klöverblad ser detsamma ut när det roteras 120 grader. För en supraledare är det av stor vikt vad händer med materialets symmetrierna, vilka av dem behåller gapfunktionen och vilka bryter den. Brott av symmetrier kan ha väsentliga resultat: Energigapet kan försvinna i vissa riktningar, det kan ha ett vinkelberoende som skiljer sig från det underliggande materialet, eller det kan bryta tidsomvandlingssymmetrin, vilket ger upphov till små magnetfält.

Förutom symmetrin för gapfunktionen har den senaste utvecklingen framhävt den vikten av topologin för supraledarens vågfunktionen. Topologi är ett matematiskt fält som klassificerar vilka objekt som kan omvandlas till varandra och vilka inte. Ett klassiskt exempel är att en kub kan förvandlas till en sfär, helt enkelt genom att pressa den lite, men den kan inte förvandlas till en torus (formen på en munk eller simring) utan att sticka ett hål i den eller limma ihop några ändar. När det gäller topologi tillhör kuben och sfären samma klass, medan en kub och en torus tillhör olika klasser. På samma sätt kan supraledare ha olika topologiska klasser, vilket innebär att vågfunktionenerna som beskriver dem inte kan omvandlas till varandra utan att stänga energigapet eller bryta en symmetri. Detta abstrakta matematiska koncept leder till en viktig effekt: När två supraledare av olika topologiska klasser ligger bredvid varandra, måste energigapet stängas på gränsen, eftersom de inte kan omvandlas till varandra utan att gapet försvinner. Detsamma gäller för en supraledarens yta vilken gränsar till vakuum eller luft, som är material av annan topologisk klass. Så även om det kräver en ändlig energi för att excitera en enstaka elektron inuti en supraledare, kommer topologiska supraledare att ha excitationer på ytan som inte kostar energi eftersom energigapet är stängt på gränsen. Dessa excitationer ses i vissa fall som byggstenar för kvantdatorer som är okänsliga för störningar, vilket ger en teknologisk motivation för studien av topologiska supraledare.

I denna avhandling modellerade jag teoretiskt supraledningsförmåga som uppstår i vissa multiorbitala material. Jag analyserade sedan vilken typ av Cooper-par som bildas, vilka symmetrier de bryter och vilka topologiska egenskaper de har. Den första delen fokuserar på en materialklass som kallas Kitaev-material. Deras definierande kännetecknet är en speciell interaktion mellan elektroner, som beror starkt på i vilken riktning två elektroner interagerar. Sådana märkliga interaktioner kan uppstå på grund av att vissa av atomerna i dessa material (Iridium eller Ruthenium) är så tunga att effekterna av relativitetsteorin måste iakttas. Detta leder till mycket komplex magnetism i Kitaev-materialen. En annan intressant aspekt av Kitaev-material är att de kan bildas i en skiktad, tvådimensionell struktur eller i komplexa tredimensionella kristaller. Tillsammans med mina medförfattare upptäckte vi att Cooper-par i Kitaev-material skulle bildas av elektroner med samma spinn mellan orbitaler från olika atomer. I de tredimensionella gitterstrukturerna kan energigapet försvinna för en hel rad riktningar och bilda så kallade nod-linjer eller bara för specifika riktningar i nod-punkter. I de skiktade tvådimensionella strukturerna

upptäckte vi en konkurrens mellan två typer av supraledning. Antingen bryter energigapet en rotationssymmetri (kallad nematisk supraledare), vilket betyder att gapet är större i endast en specifik riktning, eller tidsomvandlingssymmetrin (så kallad kiral supraledare), där små magnetfält skulle bildas. I båda fallen är supraledaren också i olika topologiska klasser, vilket ger upphov till parvisa eller individuella excitationer på ytan.

Den andra delen av avhandlingen består av ett arbete om materialet Bi_2Se_3. Experiment har visat att materialet blir supraledande och att Cooper-paren sannolikt bildas mellan två elektroner med samma spinn som kommer från olika orbitaler. I det här fallet sökte vi efter Cooper-par som bildas mellan elektroner vid olika tidpunkter vilka är förbjudna att existera vid samma tidpunkt. Dessa så kallade udda-frekvens Cooper-par förekommer generellt i supraledare med flera orbitaler när det också finns supraledningsförmåga från Cooper-par som bildas vid lika tidpunkter. Udda-frekvens Cooper-par är i allmänhet mer komplicerade än lika tidspar. I vissa situationer kan exempelvis udda-frekvenspar bildas mellan elektroner med lika spinn, när lika tidspar bildas av elektroner med motsatt spinn. I vårt arbete förutsäger vi att udda-frekvens Cooper-par i Bi_2Se_3 ska bildas mellan elektroner av samma spinn i samma orbital, vilket i någon mening skulle vara enklare än lika tidsparen. En olöst fråga är hur udda-frekvenspar påverkar supraledningsförmågan. Ett förslag är den paramagnetiska Meissner-effekten, där ett yttre magnetfält inte motverkas utan förstärks. Detta skulle vara skadligt för supraledningen, eftersom starka magnetfält bryter upp Cooper-paren. I Bi_2Se_3 upptäckte vi att de udda-frekvens Cooper-paren också motverkar ett externt magnetfält, vilket innebär att de inte är så skadliga för supraledningen som tidigare trott.

Deutsche Zusammenfassung

Topologische Supraleitung in multiorbitalen Materialien

Das ungewöhnliche Phänomen der Supraleitung, bei dem ein Material unterhalb einer bestimmten kritischen Temperatur seinen Widerstand verliert, ist seit mehr als 100 Jahren ein aktives Forschungsgebiet. Dank einiger bahnbrechender Forschungsergebnisse in den 1950er Jahren sind einfache Supraleiter in reinen Metallen wie Aluminium oder Blei relativ gut erklärt. Die Supraleitung in diesen Materialien entsteht dadurch, dass zwei Elektronen ein sogenanntes Cooper-Paar bilden, wenn zwischen ihnen eine geringe Anziehungskraft besteht. Wenn eine große Anzahl von Cooper-Paaren gebildet wird, verhalten diese sich so, als wären sie alle miteinander koordiniert. Sie können dann durch eine einzige Wellenfunktion mathematisch beschrieben werden. In diesem Sinne ist Supraleitung ein makroskopischer Quanteneffekt. Da alle Cooper-Paare gemeinsam wirken, können sie ohne Widerstand fließen, der durch die Streuung einzelner Elektronen entstehen würde. Die kombinierten Cooper-Paare wirken auch einem angelegten Magnetfeld entgegen, was als Meissner-Effekt bekannt ist. Bei einfachen Metallen beruht die Anziehungskraft zwischen zwei Elektronen auf Wechselwirkungen mit den Schwingungen des Kristallgitters, wodurch die übliche elektrostatische Abstoßung überwunden werden kann. In diesem Fall haben die beiden Elektronen, die das Cooper-Paar bilden, die gleiche Energie, aber entgegengesetzten Impuls und Spin, das mikroskopische magnetische Moment der Elektronen.

In komplexeren Materialien ist die Situation nicht abschließend geklärt. In den in Kupferkeramiken gebildeten Hochtemperatursupraleitern wird beispielsweise angenommen, dass die Cooper-Paare durch andere Wechselwirkungen gebildet werden. Weitere Komplikationen treten beispielsweise in den eisenhaltigen Supraleitern auf, wenn die Elektronen, aus denen die Cooper-Paare bestehen, aus mehreren Orbitalen bzw. Atomschalen stammen. Dann müssen die Wechselwirkungen, die die Elektronen aneinander binden, auf lokaler Ebene beschrieben und das Orbital der Elektronen berücksichtigt werden. Die Cooper-Paare, die sich aus solchen Wechselwirkungen ergeben, können deutlich vielfältiger sein: Sie haben immer noch einen entgegengesetzten Impuls, können jedoch unterschiedliche Orbitale und unterschiedliche Kombinationen von Spins beinhalten. Dies führt zu charakteristischen Eigenschaften der Supraleiter, wie zum Beispiel zu höheren kritischen Temperaturen oder einer besonderen Empfindlichkeit gegenüber angelegten Feldern oder Kristalldefekten.

Wenn zwei Elektronen in einem Cooper-Paar miteinander verbunden sind, ist eine endliche Energie erforderlich, um diese Anziehung zu überwinden und ein einzelnes Elektron anzuregen. In der Physik wird dies als Energielücke bezeichnet, die durch eine Energielückenfunktion mathematisch beschrieben werden kann. Die Energielücke spiegelt direkt die Cooper-Paare im Supraleiter wider und ist daher eine wichtige Größe für die physikalische und mathematische Beschreibung der Supraleitung. Insbesondere die Klassifizierung der Symmetrien der Lückenfunktion liefert viele Informationen über die Supraleitung und die zugrunde liegenden Wechselwirkungen. Symmetrien in der Physik sind dabei Transformationen, die ein System unverändert lassen. Zum Beispiel sieht ein Kleeblatt nach einer Drehung um 120 Grad unverändert aus. Für einen Supraleiter ist dabei eine wichtige Frage, welche der Symmetrien des Materials, das supraleitend wird, die Lückenfunktion beibehält und welche sie bricht. Das Brechen von Symmetrien kann dabei wesentliche Folgen haben: Die Energielücke kann für bestimmte Richtungen verschwinden, eine vom ursprünglichen Material abweichende Winkelabhängigkeit aufweisen oder die Zeitumkehrsymmetrie aufbrechen, wodurch kleine Magnetfelder entstehen.

Neben der Symmetrie der Lückenfunktion wurde in den letzten Jahren die zusätzliche Bedeutung der Topologie der Supraleiterwellenfunktion entdeckt. Die Topologie ist ein mathematisches Feld, das klassifiziert welche Objekte ineinander umgewandelt werden können und welche nicht. Ein klassisches Beispiel ist, dass ein Würfel leicht in eine Kugel verformt werden kann, aber nicht in einen Torus (die Form eines Schwimmrings) ohne ein Loch zu stechen oder offene Enden zusammenzukleben. In Bezug auf die Topologie gehören der Würfel und die Kugel der selben Klasse an, während ein Würfel und ein Torus zu verschiedenen Klassen gehören. In ähnlicher Weise können Supraleiter in verschiedene topologische Klassen eingeteilt werden, in denen die entsprechenden Wellenfunktionen nicht ineinander transformiert werden können, ohne die Energielücke zu schließen oder eine Symmetrie zu brechen. Dieses abstrakte mathematische Konzept führt zu einem wichtigen Effekt: Wenn zwei Supraleiter unterschiedlicher Klassen aneinander grenzen, muss sich die Energielücke an der Grenzfläche schließen, da die Wellenfunktionen nicht ineinander umgewandelt werden können, ohne die Lücke zu schließen. Gleiches gilt für die Grenze eines Supraleiters zum Vakuum oder zur Luft ist, also seiner Oberfläche. Obwohl die Anregung eines einzelnen Elektrons innerhalb des Supraleiters eine gewisse Energie erfordert, weisen topologische Supraleiter daher an der Oberfläche spezielle Anregungen auf, die keine Energie kosten, da die Energielücke geschlossen ist. Einige dieser Anregungen gelten als potenzielle Bausteine für Quantencomputer, da sie unempfindlich gegenüber Störungen sind.

In dieser Arbeit habe ich Supraleitung in bestimmten multiorbitalen Materialien theoretisch modelliert. Ich habe analysiert, welche Art von Cooper-Paaren gebildet werden, welche Symmetrien sie brechen und welche topo-

logischen Eigenschaften sie haben. Der erste Teil konzentriert sich auf eine Materialklasse namens Kitaev-Materialien. Ihr bestimmendes Merkmal ist eine spezielle Wechselwirkung zwischen Elektronen, die stark von der Richtung abhängt, in der zwei Elektronen miteinander interagieren. Solche besonderen Wechselwirkungen können auftreten, weil einige der Atome in diesen Materialien (Iridium oder Ruthenium) so schwer sind, dass die Auswirkungen der Relativitätstheorie berücksichtigt werden müssen. Dies führt zu einem sehr komplexen Magnetismus in den Kitaev-Materialien. Ein weiterer interessanter Aspekt von Kitaev-Materialien ist, dass sie entweder in einer geschichteten, effektiv zweidimensionalen Struktur oder in komplexen dreidimensionalen Kristallen auftreten können. Zusammen mit meinen Co-Autoren fand ich heraus, dass Cooper-Paare in Kitaev-Materialien von Elektronen mit demselben Spin aus Orbitalen benachbarter Gitteratome gebildet werden. In den dreidimensionalen Gitterstrukturen kann die Energielücke dabei entweder für eine ganze Reihe von Richtungen verschwinden und sogenannte Knotenlinien bilden, oder nur für bestimmte Richtungen in einzelnen Knotenpunkten. In den geschichteten zweidimensionalen Strukturen entdeckten wir zwei Arten von Supraleitung, die miteinander konkurrieren. Entweder bricht die Energielücke die Rotationssymmetrie (sogenannte nematische Supraleitung), was bedeutet, dass die Energielücke in einer bestimmten Richtung größer ist. Oder die Lückenfunktion bricht die Zeitumkehrsymmetrie (sogenannte chirale Supraleitung), so dass kleine Magnetfelder auftreten würden. Die beiden Fälle gehören zu unterschiedlichen topologischen Klassen, was entweder zu paarweisen oder zu einzelnen Anregungen auf der Oberfläche des Supraleiters führt.

Der zweite Teil der Dissertation fasst eine Studie am Material Bi_2Se_3 zusammen. Supraleitung wurde dort experimentell nachgewiesen und theoretische Betrachtungen ergaben, dass die Cooper-Paare höchstwahrscheinlich zwischen zwei Elektronen gleichen Spins gebildet werden, die aus verschiedenen Orbitalen stammen. In diesem Fall haben wir nach Cooper-Paaren gesucht, in denen die beiden Elektronen zu unterschiedlichen Zeiten in das Paar eingehen. Gleichzeitig verschwindet die Anziehung, wenn man beide Elektronen zum gleichen Zeitpunkt betrachtet. Es ist bekannt, dass diese sogenannten ungeraden Frequenzpaare häufig in Supraleitern mit mehreren Orbitalen existieren, wenn auch Supraleitung von gewöhnlichen Cooper-Paaren vorliegt, in denen sich Elektronen zum gleichen Zeitpunkt verbinden. Cooper-Paare mit ungerader Frequenz sind im Allgemeinen komplizierter als die gewöhnlichen Paare. In einigen Situationen können sich beispielsweise ungerade Frequenzpaare zwischen Elektronen mit gleichem Spin bilden, wenn die gewöhnlichen Cooper-Paare aus Elektronen mit entgegengesetztem Spin bestehen. In unserer Arbeit sagen wir voraus, dass Cooper-Paare mit ungerader Frequenz in Bi_2Se_3 auftreten und sich aus Elektronen mit gleichen Spins im selben Orbital bilden. Sie wären damit in gewisser Weise einfacher als die gewöhnlichen Cooper-Paare. Eine ungelöste Frage ist, wie die ungeraden Frequenzpaare die

supraleitenden Eigenschaften beeinflussen. Eine in anderen Situationen bereits nachgewiesene Auswirkung der ungeraden Frequenzpaare ist der paramagnetische Meißner-Effekt, bei dem ein angelegtes Magnetfeld nicht unterdrückt, sondern verstärkt wird. Dies würde sich nachteilig auf die Supraleitung auswirken, da starke Magnetfelder die Cooper-Paare aufbrechen. In Bi_2Se_3 entdeckten wir, dass die ungeraden Frequenzpaare überraschenderweise ein externes Magnetfeld letztlich doch unterdrücken, und damit nicht so schädlich für die Supraleitung sind wie bisher angenommen.

1. Introduction

In the more than one hundred years since its discovery in ultracold mercury [1], superconductivity has blossomed into a wide-ranging and diverse research field. Even though a detailed understanding of the phenomenon has been formed on the basis of BCS theory [2, 3], continued developments in experimental and theoretical physics regularly shed new light on the limits of our knowledge. The complexity of the field is built on the many different materials that have been found to superconduct, which is consequently reflected in the variety of interactions proposed to give rise to superconductivity, in the unconventional symmetries of the order parameter, and in the different combinations of the properties of the electrons making up the Cooper pairs at the heart of the superconducting state. Three rather recent developments in this field of study and their interplay are touched on in this thesis: Superconductivity emerging in multiorbital systems, the topological nature of the superconducting state, and the appearance of odd-frequency pairing.

Superconductivity in multiorbital materials goes beyond the situation in simple superconductors, which can usually be described by electrons with a single band degree of freedom in addition to spin [4]. Having to involve instead several orbitals contributing to the formation of the Cooper pairs leads to distinct changes in the theoretical description of superconductivity. Most importantly, it requires to abandon the band picture, where phonon interactions are easily implemented and the energetics of different order parameters are easily analyzed. Working in an orbital picture leads to a more local formulation, which proves valuable when including for example strong local repulsions. The additional orbital degree of freedom also allows the formation of more complex order parameters, that go beyond the simple classification in terms of parity and spin. Questions of stability and the influence of external fields or defects, however, become harder to answer when leaving behind well established results from the single band formulation [5, 6, 7, 8].

A second paradigm change during the past 15 years has been to include the topological properties of the wave function describing the superconductor [9]. Classifying the topology of the superconductor adds another layer of complexity on top of describing the symmetries of the order parameter, while displaying completely new properties such as Majorana excitations appearing on the surface or in vortex cores [10]. The extensive range of possible topological superconducting states has been meticulously studied and classified in recent years [11, 12]. Nevertheless, the search for realizations of topological superconductivity continues, aiming to find interactions in specific materials

giving rise to topologically non-trivial superconducting order. The multiplicity of possible order parameters arising in multiorbital materials could prove a helpful ingredient for this endeavor.

The final development that underlies the works in this thesis, odd-frequency pairing, can be argued to actually be very old, as it has been proposed for the first time already in the 1970s [13] and has played an important role in understanding superconducting heterostructures [14]. Its importance for the description of multiorbital superconductors, however, has not been recognized until rather recently [15, 16]. An important aspect of odd-frequency pairing in heterostructures is the appearance of a paramagnetic Meissner effect [17, 18, 19], which does not suppress, but attract external magnetic fields [20]. The generalization of this effect to multiorbital superconductors could prove detrimental to the formation of superconductivity [21, 16].

The articles summarized in this thesis are contributing to two research fields relating these developments: Superconductivity in Kitaev materials and odd-frequency superconductivity in the doped topological insulator Bi_2Se_3. The Kitaev materials are characterized by the interplay of electronic interactions, spin-orbit coupling, and crystal field of similar energy scale [22, 23]. The combination of these effects gives rise to the namesake electronic interactions described by the extended Kitaev-Heisenberg model [24, 25, 26]. These unusual, bond-dependent, highly frustrated interactions are known to underlie complex magnetic ordering [27, 28, 29, 30, 31] and have been predicted to lead to spin triplet topologically non-trivial superconducting states [32, 33]. Our work builds on previous results in several steps. First, we highlight the influence of the complex 3D lattices of some of the Kitaev materials on the superconducting states by using a simplified interaction in Paper I and III. In a second stage, we analyze the role of the off-diagonal exchange in the extended Kitaev-Heisenberg model in superconducting pairing on the 2D honeycomb lattice in Paper II. Finally, the superconducting states appearing when combining the extended Kitaev-Heisenberg model and the 3D hyperhoneycomb lattice are discussed in Paper V. The findings are detailed in this thesis and include topologically protected nodal phases supported by the lattice symmetries of the harmonic honeycomb lattices, and nematic, chiral, and time-reversal symmetric superconducting states in several topological classes originating from the unusual interactions on the honeycomb lattice.

The second focus of the thesis is a study of the experimentally established toological superconductivity in doped Bi_2Se_3 [34, 35]. The multiorbital nature of this material, which leads to the unusual nematic superconductivity [36, 37], also makes this material a likely example of an odd-frequency superconductor. In our work summarized in Paper IV we confirm the presence and importance of the odd-frequency pairing induced by the unusual interorbital order parameter. We then proceed to calculate the Meissner response of the material and discover that the odd-frequency contribution is actually diamagnetic and thereby less detrimental than proposed.

This thesis is made up of a comprehensive summary preceding the mentioned articles, which is meant to both introduce the relevant methods for the studies and review the obtained results. To achieve this, I have decided to deviate from the usual structure of first exhaustively introducing all methods and approaches before moving on to summarize the results for each work. Instead, each chapter of this thesis contains the introduction of a specific method and the results obtained from its application. The whole thesis is thus structured as follows:

Part I of the thesis opens with an introduction of the Kitaev materials in Chapter 2. I first discuss the characteristic interactions and then go over the different lattices realized in the Kitaev materials. Thereafter, I introduce different approaches to model doping of the materials with strong correlations before going over the existing literature on superconductivity in the Kitaev materials.

Chapter 3 focuses on obtaining superconductivity from the Kitaev interactions. After going over the generalized mean-field theory for a single band superconductor, I review the intricacies added by abandoning the band picture and working instead with several orbitals. Applying these approaches, I compile the derivations of the superconducting order parameters for the three different Kitaev materials we studied. In Section 3.3 I derive the Hamiltonian and self-consistency equations for spin singlet pairing on the harmonic honeycomb lattices. Then I focus on the extended Kitaev-Heisenberg interactions on the honeycomb lattice, before combining the two in the derivations for spin triplet pairing arising from the extended Kitaev-Heisenberg interaction on the hyperhoneycomb lattice.

The symmetry classification of the order parameter is at the center of Chapter 4. After reviewing some mathematical background and introducing several relevant symmetries, I present in more detail the derivation of the basis functions of the irreducible representations needed to analyze the symmetries of the order parameter. Working again system for system, I present the relevant point group, obtain the basis functions, and then discuss the classification of the solutions identified from the self-consistency equations. As in the previous chapter, I begin with the singlet pairing on the harmonic honeycomb lattices, before looking at triplet pairing on the honeycomb and hyperhoneycomb lattice, respectively.

The final chapter of the first part is dedicated to discussing the topological aspects of superconductivity in the Kitaev materials. It opens with a general introduction to the topological classification of Hamiltonians, using an illustrative example. The next section, 5.2 discusses the importance of the symmetries on the topological classification, including the periodic table of topological insulators and superconductors, and crystalline topological phases. I then shift focus to the topological invariants, introducing them mathematically in Sec. 5.3 before discussing ways to obtain them that we use in our studies in Sec. 5.4. The introductory part of the chapter concludes with a short section on

the bulk-boundary correspondence and Majorana fermions. The chapter then goes over the detailed discussion of the results obtained in the papers making up the thesis: The twist states obtained at the boundary of the $d \pm \mathrm{i}d'$ states on the harmonic honeycomb lattices, the time-reversal symmetric and time-reversal breaking states on the honeycomb lattice, and the nodal phases found in the triplet pairing on the hyperhoneycomb lattice.

The second part is based on the work on doped Bi_2Se_3 in Paper IV. Chapter 6 introduces the concept of odd-frequency superconductivity first in general terms and then highlights how multiorbital superconductors are found to generally host odd-frequency pairing. After introducing doped Bi_2Se_3 by summarizing recent research results, I present the pairing correlations obtained by determining the anomalous Green's function.

The last chapter of the second part, Chapter 7, revolves around the Meissner effect. A quick phenomenological introduction is followed by details on the microscopic approach to calculating the Meissner response. This includes a short overview of the role of the Meissner effect for odd-frequency pairing. Thereafter, I present the calculations performed for doped Bi_2Se_3, detailing the role of the linear dispersion, the splitting into intra- and interband processes and the Matsubara summation. A short rundown of the calculated Meissner response closes the chapter. The thesis then concludes with a summary.

Part I:
Topological superconductivity in Kitaev
materials

2. Kitaev materials

The Kitaev materials are mostly known for promising spin-liquid physics [38, 39], but have also been demonstrated to host topologically non-trivial superconducting phases upon doping [32, 33]. The key ingredient are in both cases the unusual bond-dependent interactions which appear from a complex interplay of crystal field, spin-orbit coupling, and electronic correlations, which are all of about the same order of magnitude [23]. In this chapter I introduce at first the interactions arising in these materials summarized in the extended Kitaev-Heisenberg model and then detail how the different lattices of the Kitaev materials can be constructed in Sec. 2.2. Thereafter, Sec. 2.3 discusses approaches to model doping while taking into account the strong correlations. Finally, I review earlier studies on superconductivity in the Kitaev materials and lay out how the works in Papers I-III, and V contribute to the field.

2.1 Extended Kitaev-Heisenberg interaction

The basic building block of all Kitaev materials consists of a d^5 ion exposed to the crystal field of a surrounding octahedral cage, as illustrated in Fig. 2.1 a). The central ion can be iridium ($5d^5$) or ruthenium ($4d^5$), while the octahedral cage is made up of oxygen (in the case of iridium) or chlorine (for ruthenium), respectively. Fig. 2.1 b) shows a schematic level diagram detailing the influence of the crystal field and spin-orbit coupling in forming effective spin $\frac{1}{2}$ degrees of freedom [40]. The crystal field splits the d-orbitals of the central ion into a lower-lying t_{2g} and a higher-energy e_g manifold. All five electrons then occupy the t_{2g} states. The strong spin-orbit coupling further splits the t_{2g} manifold and forms $j_{\text{eff}} = \frac{1}{2}$ and $j_{\text{eff}} = \frac{3}{2}$ states. For an explicit expression, the eigenstates of the $L \cdot S$ Hamiltonian are needed. The three t_{2g} orbitals are formed as linear combinations of the five $l = 2$ spherical harmonics Y_l^m,

$$d_{xy} = -\frac{\mathrm{i}}{\sqrt{2}}(Y_2^2 - Y_2^{-2}) \tag{2.1}$$

$$d_{yz} = \frac{\mathrm{i}}{\sqrt{2}}(Y_2^1 + Y_2^{-1}) \tag{2.2}$$

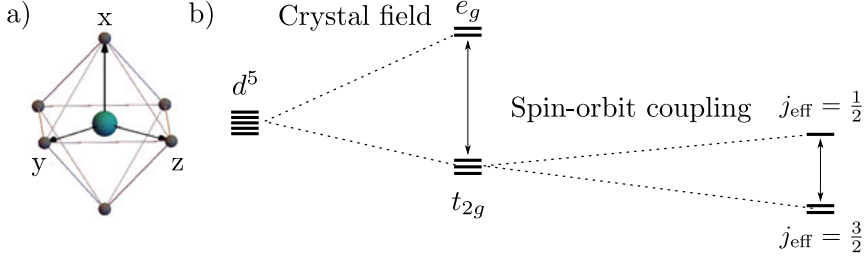$$d_{xz} = -\frac{1}{\sqrt{2}}(Y_2^1 - Y_2^{-1}), \tag{2.3}$$

Figure 2.1. a) The d^5 ion (cyan sphere) surrounded by an octahedral cage (black spheres) is the basic building block of the Kitaev materials and defines the spin quantization axes. b) Schematic of the level splitting leading to the creation of the j_{eff} orbitals. The crystal field splits the d^5 configuration into an e_g and a t_{2g} manifold. Subsequently, the spin-orbit coupling leads to the formation of the j_{eff} orbitals.

such that the angular momentum operators can be projected onto the t_{2g} basis (d_{yz}, d_{xz}, d_{xy}) to give

$$\hat{L}_x = \begin{pmatrix} 0 & 0 & 0 \\ 0 & 0 & -i \\ 0 & i & 0 \end{pmatrix}, \quad \hat{L}_y = \begin{pmatrix} 0 & 0 & -i \\ 0 & 0 & 0 \\ i & 0 & 0 \end{pmatrix}, \quad \hat{L}_z = \begin{pmatrix} 0 & 0 & 0 \\ 0 & 0 & -i \\ 0 & i & 0 \end{pmatrix}. \quad (2.4)$$

The spin-orbit coupling is then implemented by calculating

$$L \cdot S = \frac{1}{2} \left(\hat{L}_x \cdot \hat{\sigma}_x + \hat{L}_y \cdot \hat{\sigma}_y + \hat{L}_z \cdot \hat{\sigma}_z \right). \quad (2.5)$$

Importantly, this fixes the spin quantization axes to the coordinate system defined by the crystal field, which means the coordinate axes point to the corners of the octahedral cage, as depicted in Fig. 2.1 a). The $j_{\text{eff}} = \frac{1}{2}$ and $j_{\text{eff}} = \frac{3}{2}$ states then correspond to the eigenvectors of the $L \cdot S$ matrix, e.g.,

$$j_\uparrow = \frac{1}{\sqrt{3}} \left(-d_{yz\uparrow} - id_{xz\uparrow} + d_{xy\downarrow} \right) \quad (2.6)$$

$$j_\downarrow = \frac{1}{\sqrt{3}} \left(d_{yz\downarrow} - id_{xz\downarrow} + d_{xy\uparrow} \right), \quad (2.7)$$

which are separated by a gap proportional to the size of the spin-orbit coupling. Four of the five electrons then completely fill the lower-lying $j_{\text{eff}} = \frac{3}{2}$ states, which leaves one electron in the two isolated $j_{\text{eff}} = \frac{1}{2}$ states. For weak interactions, a half-filled band of effective spin $\frac{1}{2}$ would give rise to a metallic configuration, but in the Kitaev materials, strong electronic correlations lead to a Mott transition [40]. Because the $j_{\text{eff}} = \frac{1}{2}$ orbitals are a mixture of orbital and spin degrees of freedom, interactions between the pseudo-spins can easily become anisotropic.

The exact form of the interactions of the $j_{\text{eff}} = \frac{1}{2}$ moments are determined by projecting the electronic correlations and the possible hopping to nearest
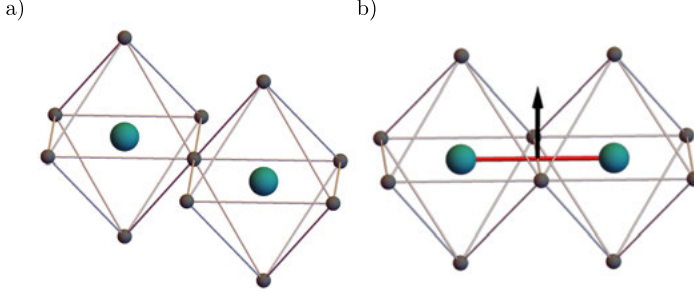
Figure 2.2. An illustration of the two ways of arranging two neighboring octahedral cages, which will lead to different interactions between the moments on the central sites in the strong coupling limit. a) Corner-sharing octahedra. b) Edge-sharing octahedra with the spin component perpendicular to the nearest neighbor bond and the shared edge pictured.

neighbor sites in the t_{2g} manifold onto the new degrees of freedom. Hopping between nearest neighbors involves direct overlaps of the d-orbitals and indirect processes through the cage ions. Consequently, the form of the interaction depends on how two nearest neighbors are arranged, specifically on whether the octahedra share a corner or an edge [24, 25]. In the case of corner-sharing, which is illustrated in Figure 2.2 a), there is only one corner ion, forming a single indirect hopping path. Projecting the interactions onto the $j_{\text{eff}} = \frac{1}{2}$ degrees of freedom and taking a limit of strong interactions yields to frozen spins $\boldsymbol{S}_i$, which interact through the isotropic Heisenberg interaction $H = J\boldsymbol{S}_i \cdot \boldsymbol{S}_j$. This situation is realized for example in Sr_2IrO_4 [40]. In the Kitaev materials, adjacent octahedra share an edge. In this situation, depicted in Fig. 2.2 b), neighboring central ions share two corners. There are then two indirect hopping paths, which lead to a destructive interference when projecting onto the $j_{\text{eff}} = \frac{1}{2}$ degrees of freedom and the resulting interaction in the strong coupling limit is of Ising type $H = IS_i^\gamma S_j^\gamma$ [24, 25]. Only the spin component S^γ perpendicular to both the shared edge and the vector connecting the central ions is active in this exchange, as schematically presented in Fig. 2.2 b).

In all Kitaev materials the lattice structure is tricoordinated, formed by arranging three edge-sharing octahedra around a central site as depicted in Fig. 2.3 b). Each nearest neighbor bond then features one particular spin component perpendicular to it, such that the Ising interaction involves different spin components S^γ on different nearest neighbor bonds $\langle i, j \rangle$ connecting sites i and j. This gives rise to the anisotropic Kitaev interaction [38]

$$H_{\text{K}} = K \sum_{\langle i,j \rangle} S_i^{\gamma(i,j)} S_j^{\gamma(i,j)}, \qquad (2.8)$$

which explains the name Kitaev materials. The function $\gamma(i,j)$ encodes the component active on each bond, correspondingly labeled as x,y,z-bond, respectively. A common representation is to color the bonds (red, blue, green) for an (x,y,z) bond, respectively, see Fig. 2.3.

The Kitaev interaction is, however, not the only interaction present in the materials. The presence of further hopping terms in the t_{2g} manifold, either through direct overlap or involving the e_g orbitals, leads to other interactions beyond the Kitaev term H_K, when projected onto the $j_{\text{eff}} = \frac{1}{2}$ states [26, 22]. The details will depend on a variety of parameters, such that a general approach is to include all interaction terms which are allowed by the local symmetry of two edge-sharing octahedra. This most generic nearest neighbor Hamiltonian for Kitaev materials in the absence of deformations is called the extended Kitaev-Heisenberg model and given by [26]

$$H_{\text{JK}\Gamma} = J \sum_{\langle i,j \rangle} \boldsymbol{S}_i \cdot \boldsymbol{S}_j + K \sum_{\langle i,j \rangle} S_i^{\gamma(i,j)} S_j^{\gamma(i,j)} + \Gamma \sum_{\langle i,j \rangle} \left(S_i^{\alpha(i,j)} S_j^{\beta(i,j)} + S_i^{\beta(i,j)} S_j^{\alpha(i,j)} \right).$$
(2.9)

In addition to the Kitaev exchange K, this Hamiltonian also contains the isotropic Heisenberg interaction J, and the symmetric off-diagonal exchange Γ. The last interaction couples the two spin components not involved in the Kitaev exchange $\alpha(i,j) \neq \beta(i,j) \neq \gamma(i,j)$ whose sum is perpendicular to both the bond and the Kitaev active spin component.

2.2 From honeycomb to harmonic honeycomb lattice

There are thus four ingredients for the appearance of the Hamiltonian Eq. (2.9): An octahedral crystal field, strong spin-orbit coupling, electronic correlations, and a tricoordinated lattice of edge-sharing octahedra. Three materials are known to exhibit these characteristics: Na_2IrO_3 [25, 27], Li_2IrO_3 [41], and α-$RuCl_3$ [42]. Whereas Na_2IrO_3 and α-$RuCl_3$ form structures consisting of weakly coupled honeycomb layers, Li_2IrO_3 exists in three different crystal structures labeled by α-,β-, and γ-Li_2IrO_3, respectively [43, 44]. The α polymorph is also of the layered honeycomb type, while β- and γ-Li_2IrO_3 form 3D tricoordinated lattices related to the honeycomb lattice. These lattices are called hyperhoneycomb and stripyhoneycomb, respectively, and form the two smallest members of the hypothetical harmonic honeycomb lattices. Here, I will detail how the lattices are built up from the three nearest neighbor bonds introduced in the previous section.

The easiest construction is the 2D honeycomb lattice. The three nearest neighbor bonds span the 2D plane of the honeycomb lattice, which is compactly expressed in terms of the lattice coordinate system $(\tilde{x}, \tilde{y}, \tilde{z})$ specified in
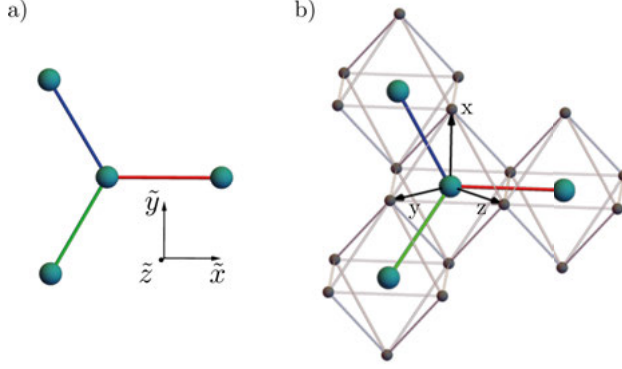
Figure 2.3. a) The three nearest neighbor bonds with the lattice coordinate system and b) the same structure including the surrounding octahedral cage and the corresponding local coordinate system. The spin component active in the Kitaev interaction on an (x, y, z) bond is marked by the colors (red, blue, green), respectively.

Fig. 2.3 a). In this basis, the nearest neighbor bonds are expressed as

$$\boldsymbol{a}_1 = (1, 0, 0), \quad \boldsymbol{a}_2 = \left(-\frac{1}{2}, \frac{\sqrt{3}}{2}, 0\right), \quad \boldsymbol{a}_3 = \left(-\frac{1}{2}, -\frac{\sqrt{3}}{2}, 0\right), \quad (2.10)$$

and the lattice is spanned by the vectors $\boldsymbol{v}_1 = \frac{1}{2}(3, \sqrt{3}, 0)$ and $\boldsymbol{v}_2 = (0, -\sqrt{3}, 0)$, all given in units of the nearest neighbor bond length. While this coordinate system is convenient for defining the lattice, it leads to a complicated form of the interaction, which is most easily expressed in terms of the local coordinate system (x, y, z) pointing to the corners of the octahedra, as defined in the construction of the j_{eff} states in the previous section and pictured in Fig. 2.3 b). In terms of the local coordinate system, the nearest neighbor vectors are given by

$$\boldsymbol{a}_1 = (0, -1, 1)_{loc}, \quad \boldsymbol{a}_2 = (1, 0, -1)_{loc}, \quad \boldsymbol{a}_3 = (-1, 1, 0)_{loc}, \quad (2.11)$$

where the subscript indicates the different coordinate system. In the local coordinate system it also becomes clear which spin component is perpendicular to the bonds and thus active in the Kitaev exchange: $\gamma(i, 1) = x$, $\gamma(i, 2) = y$, and $\gamma(i, 3) = z$. Correspondingly, the perpendicular spin components involved in the off-diagonal exchange are $\alpha(i, 1) = y$, $\beta(i, 1) = z$, $\alpha(i, 2) = x$, $\beta(i, 2) = z$, and $\alpha(i, 3) = x$, $\beta(i, 3) = y$.

When constructing the nearest neighbor bonds in the local coordinate system, a second possibility to arrange the octahedra becomes apparent. Interchanging which of the second and third neighbors sticks "backward" and "forward", respectively, results in the set

$$\boldsymbol{a}'_1 = (0, -1, 1)_{loc}, \quad \boldsymbol{a}'_2 = (1, 1, 0)_{loc}, \quad \boldsymbol{a}'_3 = (-1, 0, -1)_{loc}. \quad (2.12)$$

28
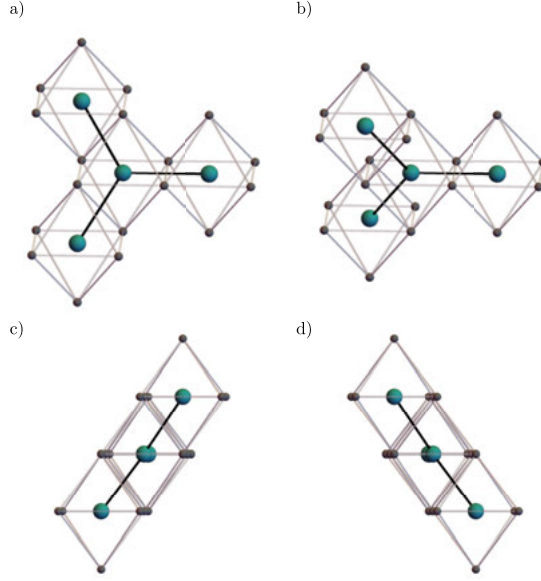
Figure 2.4. An illustration of the two different choices of nearest neighbor vectors. a) and c) show the unprimed vectors $\boldsymbol{a}_i$ while b) and d) show the structure arising from the rotated vectors $\boldsymbol{a}_i'$. Front view in panels a) and b) and side view in panels c) and d).

These three bonds can still be used to span a honeycomb lattice, but translate to the rotated vectors

$$\boldsymbol{a}_1' = (1,0,0), \qquad \boldsymbol{a}_2' = \frac{1}{2}\left(-1, \sqrt{3}\cos(\alpha), \sqrt{3}\sin(\alpha)\right),$$

$$\boldsymbol{a}_3' = \frac{1}{2}\left(-1, -\sqrt{3}\cos(\alpha), -\sqrt{3}\sin(\alpha)\right), \tag{2.13}$$

in the lattice coordinate system. The angle α is defined by the geometry of the octahedra and given by $\alpha = \arccos\left(\frac{1}{3}\right) \approx 70°$. Building a lattice from these rotated nearest neighbor vectors results in a honeycomb lattice that is rotated with respect to the unprimed nearest neighbor vectors. Figure 2.4 visualizes the difference between the two different sets of nearest neighbor bonds by showing both a front (panels a) and b)) and a side view (panels c) and d)) of them. An important aspect of the rotated nearest neighbor bonds is that now different spin components are perpendicular to the bonds, such that we have the following spin components active in the Kitaev exchange: $\gamma(i,1') = x$, $\gamma(i,2') = z$, and $\gamma(i,3') = y$. Correspondingly, the off-diagonal exchange will also be interchanged and picks up minus signs on several of the bonds: $\alpha(i,1') = y$, $\beta(i,1') = z$, $\alpha(i,2') = -x$, $\beta(i,2') = y$, and $\alpha(i,3') = x$, $\beta(i,3') = -z$.

Because both sets of nearest neighbor bonds are locally identical, it is possible to transition from one orientation to the other and construct 3D lattices. The series of lattices that can in this way be constructed from connecting stripes of consecutively rotated honeycomb lattices by a twist are then called the harmonic honeycomb lattices [43] and illustrated in Fig. 2.5. They are labeled by the number of honeycombs n in between twists as $\mathcal{H}\langle n\rangle$. The limiting case of $\mathcal{H}\langle\infty\rangle$ corresponds to a stack of infinite 2D honeycomb planes, as depicted in Fig. 2.5 a). Introducing a single twist, where the zigzag vectors change from $\boldsymbol{a}_{2/3}$ to $\boldsymbol{a}'_{2/3}$, forms a true 3D lattice shown in Fig. 2.5 b). In the harmonic honeycomb series, such a twist is repeatedly introduced after n full honeycombs. The two smallest members are the structures realized in Li_2IrO_3 and are named the stripy- and hyperhoneycomb lattice and pictured in Fig. 2.5 c) and d), respectively. As the smallest member of the harmonic honeycomb series, the hyperhoneycomb lattice is well suited to discuss the symmetries of the 3D lattices. As illustrated in Fig. 2.6, its unit cell consists of four lattice sites connected by six nearest neighbor bonds, of which three ($\boldsymbol{a}_{4-6}$) are rotated:

$$(1 \to 2) \qquad \boldsymbol{a}_1 = (1,0,0) \tag{2.14}$$

$$(1 \to 4) \qquad \boldsymbol{a}_2 = \frac{1}{2}(-1,\sqrt{3},0) \tag{2.15}$$

$$(1 \to 4) \qquad \boldsymbol{a}_3 = \frac{1}{2}(-1,-\sqrt{3},0) \tag{2.16}$$

$$(3 \to 4) \qquad \boldsymbol{a}_4 = (1,0,0) \tag{2.17}$$

$$(3 \to 2) \qquad \boldsymbol{a}_5 = \frac{1}{2}(-1,\sqrt{3}\cos(\alpha),\sqrt{3}\sin(\alpha)) \tag{2.18}$$

$$(3 \to 2) \qquad \boldsymbol{a}_6 = \frac{1}{2}(-1,-\sqrt{3}\cos(\alpha),-\sqrt{3}\sin(\alpha)). \tag{2.19}$$

This leads to a series of zigzag chains rotated against each other and bound together by the horizontal twist bonds $\boldsymbol{a}_1$ and $\boldsymbol{a}_4$. The symmetries of the lattice can be summarized by placing the lattice into a third, Cartesian, coordinate system $(\bar{x},\bar{y},\bar{z})$ (pictured in Fig. 2.6) and choosing the center of the twist bond $\boldsymbol{a}_1$ as the center of symmetry C. Then the lattice is symmetric under three C_2 rotations about the Cartesian axes, inversion, and three glide reflections with respect to the mirror planes perpendicular to the Cartesian axes. The glides are thus a non-symmorphic symmetry. The point group generated by these symmetries is D_{2h}. All larger harmonic honeycombs share the same symmetries.

2.3 Modeling doping

In their intrinsic form, the Kitaev materials are Mott insulators, where the strong interactions lead to the opening of an energy gap. In order to achieve
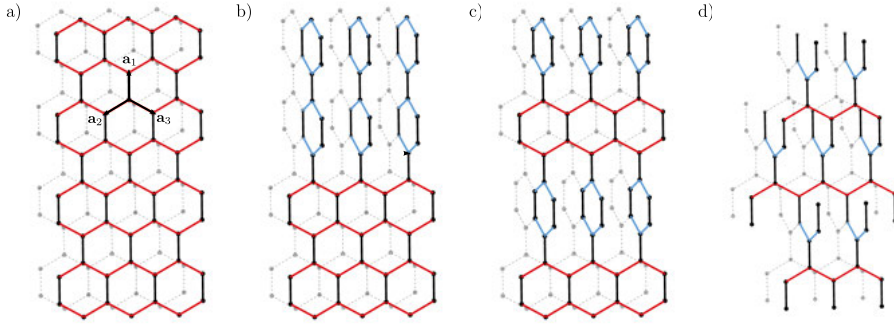
Figure 2.5. An illustration of the harmonic honeycomb lattice series. a) The $\mathcal{H}\langle\infty\rangle$ strucure, an infinite stack of 2D honeycomb sheets with the three nearest neighbor vectors $\boldsymbol{a}_1$, $\boldsymbol{a}_2$ and $\boldsymbol{a}_3$. b) Changing the zigzag nearest neighbor vectors from $\boldsymbol{a}_i$ (red) to $\boldsymbol{a}_i'$ (blue) creates the twist structure, which can be periodically repeated along the direction of $\boldsymbol{a}_1$. The two smallest members of the harmonic honeycomb series are the c) stripyhoneycomb ($\mathcal{H}\langle 1\rangle$) and d) hyperhoneycomb ($\mathcal{H}\langle 0\rangle$) lattices. In all structures the zigzag bonds $\boldsymbol{a}_2$ and $\boldsymbol{a}_3$ are drawn in red, rotated zigzag bonds $\boldsymbol{a}_2'$ and $\boldsymbol{a}_3'$ in blue, and additional honeycomb layers are depicted in grey. Figure taken from Paper I.
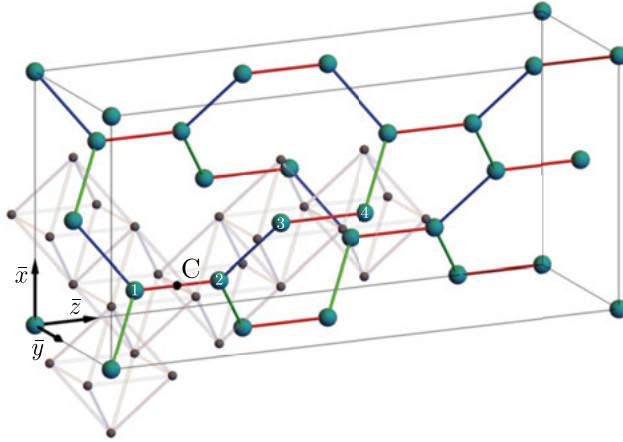
Figure 2.6. The hyperhoneycomb lattice placed in the cartesian coordinate system $(\bar{x}, \bar{y}, \bar{z})$. The cyan spheres are the Ir ions making up the lattice where the four lattice sites in the unit cell are labeled $1, \ldots, 4$. The bonds are again shaded in the colors (red, blue, green) to mark an (x, y, z) bond, respectively. The center of symmetry C lies at the center of the horizontal bond $\boldsymbol{a}_1$. The oxygen atoms (black) form the octahedral cages shown in grey.

superconductivity, doping has to introduce mobile charge carriers. At the same time, the strong correlations giving rise to the extended Kitaev-Heisenberg interactions will also influence these carriers. An intuitive approximation is that the correlations lead to an additional energy cost of a doubly occupied site due to a mutual on-site Coulomb repulsion U. In the limit of strong correlations $U \rightarrow \infty$, double occupancy of a site can be considered as forbidden.

A first approach to doping used in Paper I was to simply add fermionic carriers governed by a tight binding Hamiltonian without explicitly taking into account the strong correlations. The doping level is set through the chemical potential μ. Possible effects of the strong correlations can then be taken into account by considering the parameters of the model as phenomenological, such that a possible rescaling is already absorbed into the parameters. One downside of this simple approach is that it is not able to capture the Mott insulating state at zero doping.

2.3.1 Slave-boson mean-field theory

In slave-boson mean-field theory, used in Paper II, strong correlations are treated by enhancing the Hilbert space of the original problem through the introduction of the boson operators $b_i^\dagger$ and $d_i^\dagger$. These represent the empty and double occupation at site i, respectively. This gives the following four states for each site [45, 46]

$$|0\rangle = b^\dagger |vac\rangle \quad |\uparrow\rangle = f_\uparrow^\dagger |vac\rangle \quad |\downarrow\rangle = f_\downarrow^\dagger |vac\rangle \quad |\uparrow\downarrow\rangle = d^\dagger |vac\rangle, \quad (2.20)$$

where $|vac\rangle$ is then the vacuum state of the extended Hilbert space. The creation operator of the original Hilbert space is then mapped to [47]

$$c_{i\sigma}^\dagger = f_{i\sigma}^\dagger b_i + \varepsilon_{\sigma\bar{\sigma}} d_i^\dagger f_{i\bar{\sigma}}, \quad (2.21)$$

where $\varepsilon_{\uparrow\downarrow} = -\varepsilon_{\downarrow\uparrow} = 1$ is the antisymmetric tensor. The action of adding a particle of spin σ at site i is thus dependent on the state acted upon. For the empty site, $c_{i\sigma}^\dagger$ removes the empty site b_i and adds a fermion $f_{i\sigma}^\dagger$. When acting on a singly occupied site, it removes the fermion of opposite spin $f_{i\bar{\sigma}}$ and adds the doubly occupied site $d_i^\dagger$. The mapping is completed by the constraint that each site is either empty, singly occupied, or doubly occupied

$$b_i^\dagger b_i + f_{i\uparrow}^\dagger f_{i\uparrow} + f_{i\downarrow}^\dagger f_{i\downarrow} + d_i^\dagger d_i = 1. \quad (2.22)$$

The constraint in Eq. (2.22) ensures that the operators in the enhanced Hilbert space obey the same algebra as the original c operators [47]. Strong correlations are taken into account by removing the possibility of double occupancy by deleting the operators $d_i^\dagger$, d_i. This gives

$$c_{i\sigma}^\dagger = f_{i\sigma}^\dagger b_i \qquad \text{and} \qquad b_i^\dagger b_i + f_{i\uparrow}^\dagger f_{i\uparrow} + f_{i\downarrow}^\dagger f_{i\downarrow} = 1. \quad (2.23)$$

This is no longer an exact mapping, but rather the requirement that both expressions reproduce the same matrix elements in the Hilbert space without double occupancy [47]. A further approximation is to assume a uniform mean-field distribution of the bosons, which is appropriate for large enough doping, by replacing the remaining operators $b^\dagger$ and b by their expectation values $\langle b_i^\dagger \rangle = \langle b_i \rangle = \bar{b}$, where $\bar{b} \in \mathbb{R}$ and site independent. Denoting the amount of holes introduced by doping by $\delta = \bar{b}^2$, the filling at each site is given by

$$f_{i\uparrow}^\dagger f_{i\uparrow} + f_{i\downarrow}^\dagger f_{i\downarrow} = 1 - \delta, \tag{2.24}$$

which follows directly from Eq. (2.23). A hopping term of the form $t_{ij} c_{i\sigma}^\dagger c_{j\sigma'}$ will subsequently be replaced by

$$t_{ij} c_{i\sigma}^\dagger c_{j\sigma'} = t_{ij} f_{i\sigma}^\dagger b_i f_{j\sigma'} b_j \approx t_{ij} \bar{b}^2 f_{i\sigma}^\dagger f_{j\sigma'}, \tag{2.25}$$

which is equivalent to a rescaled hopping parameter $\tilde{t}_{ij} = \delta t_{ij}$. In this way slave-boson mean-field theory captures the Mott insulating state in the limit of $\delta \to 0$ as the hopping term will vanish. The quartic terms appearing in spin-spin interaction terms, however, can be rewritten completely in terms of the new fermion operators $f_i^\dagger$, such that the interaction parameters are not rescaled [48, 47]. Doping is then modeled by introducing a tight-binding Hamiltonian which is solved in the full fermionic Hilbert space of the f operators and the strong correlations are taken into account by rescaling the hopping amplitudes and adjusting the chemical potential accordingly to match the doping level set by δ.

Slave-boson theory can be further refined by using field-theoretical approaches to go beyond the mean-field approximation [46, 47] and by introducing more bosons capturing the symmetries of fluctuations [49, 47]. The approach can also be extended to several orbitals by introducing a slave-boson for each orbital [50].

2.3.2 Gutzwiller approximation

A third method, applied in Paper V, is the Gutzwiller approximation. In this approach, the effect of strong correlations are incorporated by removing the double occupancy through statistical weighing factors g. In this way an expectation value taken in a projected Hilbert space without double occupancy $\langle \ldots \rangle$ is approximated by the expectation value in the full Hilbert space $\langle \ldots \rangle_0$ multiplied by the statistical weighing factor [51, 52]

$$\langle \hat{O} \rangle \approx g_O \langle \hat{O} \rangle_0. \tag{2.26}$$

As a result, all calculations can be performed in the full Hilbert space with the strong correlation accounted for by renormalized parameters that depend on the doping level. The weighing factors g can be determined from counting

$S_i^+ S_j^+$

$S_i^- S_j^-$
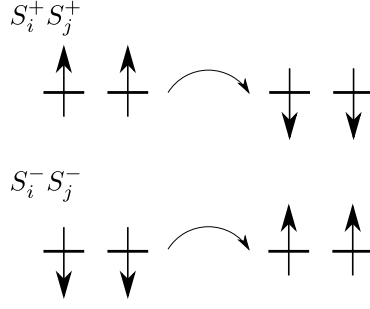
Figure 2.7. Schematic drawing of the exchange process contributing to the off-diagonal exchange. Both sites need to be singly occupied.

arguments, where the ratio between expectation values in the projected and full Hilbert spaces is determined by considering the different probabilities of a site being empty, singly, or doubly occupied. As an example, I want to present the derivation of the weighing factor g_Γ for the off-diagonal exchange

$$\Gamma\left(S_i^x S_j^y + S_i^y S_j^x\right) = \frac{\Gamma}{2i}\left(S_i^+ S_j^+ - S_i^- S_j^-\right).$$ (2.27)

In the second equality the raising and lowering operators are given $S_i^\pm = S_i^x \pm i S_i^y$. The off-diagonal exchange thus requires both sites to be singly occupied by the same spin, as depicted in Fig. 2.7. The probability of a site i being occupied by a single spin σ are then given by the density $n_{i\sigma}$ in the projected and by $n_{i\sigma}^0(1 - n_{i\bar\sigma}^0)$ in the unprojected space. The difference arises from having to explicitly rule out the double occupancy in the unprojected full Hilbert space. The weighing factor g_Γ is then given by

$$g_\Gamma = \frac{\langle S_i^+ S_j^+ \rangle}{\langle S_i^+ S_j^+ \rangle_0} = \frac{\left(n_{i\downarrow} n_{j\downarrow} n_{i\uparrow} n_{i\uparrow}\right)^{\frac{1}{2}}}{\left(n_{i\downarrow}^0(1 - n_{i\uparrow}^0) n_{j\downarrow}^0(1 - n_{j\uparrow}^0) n_{i\uparrow}^0(1 - n_{i\downarrow}^0) n_{j\uparrow}^0(1 - n_{j\downarrow}^0)\right)^{\frac{1}{2}}},$$ (2.28)

where the square roots appear because expectation values only give a probability density. The case for $S_i^- S_j^-$ actually gives the same probabilities, as it is the same process in reverse. The expression is simplified by assuming a homogeneous system without magnetic ordering, such that $n_{i\uparrow} = n_{i\downarrow} = \frac{n}{2}$ and $n_{i\uparrow}^0 = n_{i\downarrow}^0 = \frac{n}{2}$. This gives

$$g_\Gamma = \frac{1}{\left(1 - \frac{n}{2}\right)^2} = \frac{4}{(1 + \delta)^2},$$ (2.29)

where the density has been written in terms of the doping at each site $n = 1 - \delta$ for the last equation. Repeating similar arguments, the same factor is obtained

34

for the Heisenberg and Kitaev exchange, such that all interaction terms are rescaled by $g_\Gamma = g_K = g_J$. The rescaling for the hopping terms for the mobile carriers introduced by doping can similarly be determined to be [52]

$$g_t = \frac{2\delta}{1 + \delta}. \tag{2.30}$$

The Gutzwiller approximation then captures the Mott insulating state in the limit of $\delta \to 0$ by $g_t \to 0$ and $g_J \to 4$, effectively freezing out mobile carriers and enhancing the interactions.

2.4 Superconductivity in Kitaev materials

Before introducing the theoretical tools to determine and classify the superconducting phases found in Kitaev materials in the next chapters, I want to review the existing literature and identify where our works contribute.

The main current focus of research on Kitaev materials is the search for a quantum spin liquid [22, 53, 23]. The pure Kitaev model $K \neq 0$, $J = \Gamma = 0$ on the honeycomb lattice can be solved exactly by rewriting it in terms of Majorana fermions and has a quantum spin liquid ground state [38]. The presence of the other interactions terms in the Kitaev materials complicates the phase diagram, with multiple magnetically ordered phases possible, depending on the included interactions and the lattice in question [25, 26, 54, 55, 56, 57, 58, 59]. Experimentally, all known Kitaev materials display a magnetic ordering at low temperatures [27, 28, 29, 30, 31]. The honeycomb materials α-RuCl$_3$ and Na$_2$IrO$_3$ magnetize in an antiferromagnetic zigzag phase and Li$_2$IrO$_3$ displays complicated magnetic spiral phases both in the 2D honeycomb and 3D hyper- and stripyhoneycomb lattices. While the Kitaev spin liquid itself has not been found, unusual excitations seem to imply that the Kitaev materials are relatively close to it [60, 61, 62], and several other spin liquid candidates have been discovered by exchanging some Lithium in the hyperhoneycomb lattice by hydrogen [63], or by applying a strong magnetic field to α-RuCl$_3$ [64, 65, 66].

Considering that such prominent superconductors as the cuprates arise from doping Mott insulators [52, 47, 67], studying superconducting phases in doped Kitaev materials follows naturally. One of the main results of previous studies is that the Kitaev interaction leads to a spin triplet pairing [32, 33]. Both a time-reversal symmetry breaking or a time-reversal symmetric solution can be stabilized, depending on the doping level. The topological classification of these solutions yields a non-trivial Chern number for the time-reversal breaking state [32]. The time-reversal symmetric state, on the other hand, can be classified in terms of a $\mathbb{Z}_2$ invariant. Above a critical doping level this invariant takes a non-trivial value [33]. Below this critical doping, a symmetry-

protected topological state with finite spin Chern number appears [68]. A magnetic field can be used to tune between the different phases [68].

The extension to the Kitaev-Heisenberg model $K \neq 0$, $J \neq 0$, $\Gamma = 0$, has also been studied using several theoretical approaches, including slave-boson and functional renormalization group techniques [32, 33, 69, 70]. The spin triplet states driven by the Kitaev exchange are in competition with a spin singlet order caused by the Heisenberg interaction, where the spin triplet solution is favorable for $J \lesssim \frac{K}{2}$. The spin singlet state has been extensively studied in the limit $J \neq 0$, $K = \Gamma = 0$ and corresponds either to a chiral $d \pm \mathrm{i} d'$-wave state or to an extended s-wave solution, depending on the doping level [71]. An RPA analysis of the particle-hole fluctuations in the Kitaev-Heisenberg model also supports spin singlet pairing [72]. Other possible superconducting states include an FFLO state in a Kitaev-Heisenberg model with a spin-orbit coupled nearest neighbor hopping [73]. Finally, in a complementary approach to doping Kitaev materials, Kitaev-Kondo models have been proposed and shown to host nematic spin triplet superconductivity with point nodes [74] in addition to the previously mentioned spin triplet states [75].

So far, superconductivity has not been observed in any of the Kitaev materials, even though several attempts of doping have been made. Na_2IrO_3, for example, displays a shift in the chemical potential when adding potassium to cleaved surfaces [76]. The intercalation of potassium into $RuCl_3$ only yields one stable compound, $K_{0.5}RuCl_3$, which forms a static charge ordering [77]. The addition of potassium also gives rise to an additional density of states below the Fermi energy, as does doping by Rb ions [78]. Attempts to introduce non-magnetic Ir in place of Ru lead to a suppression of the magnetic ordering, but no mobile carriers [79, 80]. A study of hydrated and lithium intercalated $RuCl_3$, $Li_xRuCl_3 \cdot y\,H_2O$ found a decreased resistance and signatures of a charge ordering, but no superconductivity [81]. Theoretical calculations propose to make use of the layered structure of $RuCl_3$ by proximitizing a 2D film to graphene, which would lead to strong doping effects [82, 83]. This could be a promising route, as single layers of $RuCl_3$ have already been produced successfully [84] and stacked on graphene [85, 86, 87].

The works in this thesis complement the research on superconductivity in the Kitaev materials in two ways. First of all, we extend the study of superconductivity to the 3D Kitaev materials in Papers I, III, and V. We focus on the influence of the lattice geometry on the pairing function by restricting at first to spin singlet pairing from a Heisenberg interaction in Paper I and III. We then include the full extended Kitaev-Heisenberg interaction to make closer contact with the Kitaev materials in Paper V. Secondly, we augment earlier studies by considering the effect of the off-diagonal exchange on the superconducting pairing in the 2D honeycomb lattice (Paper II). The following chapters include the detailed derivations and results from these works.

3. Superconductivity

Having introduced the extended Kitaev-Heisenberg interaction in the previous chapter, in this chapter I present how to obtain the superconducting order parameters arising upon doping. At first I introduce the general mean-field framework of superconductivity for spin singlet and triplet pairing in the single band case, following closely the presentation in a popular review article by Sigrist and Ueda [4]. In Section 3.2, I extend this approach to the multiorbital case relevant for the Kitaev materials and briefly introduce the concept of superconducting fitness, useful for analyzing multiorbital pairing [5, 6]. In the last three sections I outline how to obtain the pairing Hamiltonian and the self-consistency equations necessary to calculate the superconducting order parameters for spin singlet pairing in the harmonic honeycomb lattices (Paper I), and spin triplet pairing from the extended Kitaev-Heisenberg interactions on the honeycomb lattice (Paper II) and the hyperhoneycomb lattice (Paper V).

3.1 Generalized mean-field theory

In the spirit of the original BCS discussion, I begin the derivation of the mean-field theory from a model Hamiltonian that couples electrons of opposite momenta, allowing, however, for a more general $\boldsymbol{k}$-dependent interaction V and Cooper pairs of arbitrary spins

$$H = \sum_{\boldsymbol{k},\sigma} h_0(\boldsymbol{k}) c^\dagger_{\boldsymbol{k}\sigma} c_{\boldsymbol{k}\sigma} + \sum_{\boldsymbol{k},\boldsymbol{k}'} \sum_{\sigma\bar{\sigma}\tau\bar{\tau}} V_{\sigma\bar{\sigma}\tau\bar{\tau}}(\boldsymbol{k},\boldsymbol{k}') c^\dagger_{\boldsymbol{k}\sigma} c^\dagger_{-\boldsymbol{k}\bar{\sigma}} c_{-\boldsymbol{k}'\tau} c_{\boldsymbol{k}'\bar{\tau}}. \qquad (3.1)$$

The operator $c^\dagger_{\boldsymbol{k}\sigma}$ creates electrons of wave vector $\boldsymbol{k}$ and spin σ. At first I will restrict to the single band picture, where the non-interacting or normal state Hamiltonian is diagonal and given by the degenerate band dispersion of the electrons $\hat{h}_0(\boldsymbol{k}) = \xi(\boldsymbol{k})\hat{\sigma}_0$, where $\hat{\sigma}_0$ is the 2×2 identity matrix. The scattering matrix elements in the interaction term are defined via

$$V_{\sigma\bar{\sigma}\tau\bar{\tau}}(\boldsymbol{k},\boldsymbol{k}') = \langle \boldsymbol{k},\sigma; -\boldsymbol{k},\bar{\sigma}| \hat{V} | \boldsymbol{k}',\bar{\tau}; -\boldsymbol{k}',\tau\rangle. \qquad (3.2)$$

The interaction must obey the fermionic anti-commutation relations, such that

$$V_{\sigma\bar{\sigma}\tau\bar{\tau}}(\boldsymbol{k},\boldsymbol{k}') = -V_{\bar{\sigma}\sigma\tau\bar{\tau}}(-\boldsymbol{k},\boldsymbol{k}') = -V_{\sigma\bar{\sigma}\bar{\tau}\tau}(\boldsymbol{k},-\boldsymbol{k}') = V_{\bar{\sigma}\sigma\bar{\tau}\tau}(-\boldsymbol{k},-\boldsymbol{k}') \quad (3.3)$$

As a next step, a mean-field decoupling is performed, which amounts to rewriting any general product of operators A and B with the help of their averages $\langle \ldots \rangle$ as

$$
\begin{aligned}
AB &= (A - \langle A \rangle + \langle A \rangle)(B - \langle B \rangle + \langle B \rangle) \\
&= A \langle B \rangle + \langle A \rangle B - \langle A \rangle \langle B \rangle + (A - \langle A \rangle)(B - \langle B \rangle).
\end{aligned} \tag{3.4}
$$

The last term $(A - \langle A \rangle)(B - \langle B \rangle)$ can be considered as a quadratic term of fluctuations around the mean-field value and can be neglected if those fluctuations are small, such that

$$
AB \approx A \langle B \rangle + \langle A \rangle B - \langle A \rangle \langle B \rangle. \tag{3.5}
$$

The crucial step for studying superconductivity is to use this decoupling with the pair operators, which amounts to assuming that there is a non-zero expectation value of Cooper pairs

$$
\langle A \rangle = \langle c_{k\sigma}^\dagger c_{-k\bar{\sigma}}^\dagger \rangle \qquad\qquad \langle B \rangle = \langle c_{k'\tau} c_{-k'\bar{\tau}} \rangle. \tag{3.6}
$$

The resulting mean-field Hamiltonian is then

$$
H_{\text{MF}} = \sum_{k\sigma} \xi_k c_{k\sigma}^\dagger c_{k\sigma} - \sum_{k} \sum_{\sigma\bar{\sigma}} \left(\Delta_{\sigma\bar{\sigma}}(k) c_{k\sigma}^\dagger c_{-k\bar{\sigma}}^\dagger + \Delta_{\sigma\bar{\sigma}}^*(k) c_{-k\bar{\sigma}} c_{k\sigma} \right) + \text{const.} \tag{3.7}
$$

The constant term arises from the product of the expectation values and is henceforth dropped, as it only shifts the overall energy. The gap function is defined via the expectation value:

$$
\Delta_{\sigma\bar{\sigma}}(k) = -\sum_{k'} \sum_{\tau\bar{\tau}} V_{\sigma\bar{\sigma}\tau\bar{\tau}}(k, k') \langle c_{-k'\tau} c_{k'\bar{\tau}} \rangle. \tag{3.8}
$$

As a result of this mean-field approximation, the Hamiltonian H_{MF} is now quadratic in fermion operators as opposed to the original Hamiltonian in Eq. (3.1), which contained a quartic interaction term.

The gap function is a matrix in spin space

$$
\hat{\Delta} = \begin{pmatrix} \Delta_{\uparrow\uparrow} & \Delta_{\uparrow\downarrow} \\ \Delta_{\downarrow\uparrow} & \Delta_{\downarrow\downarrow} \end{pmatrix} \tag{3.9}
$$

which has the property

$$
\hat{\Delta}(k) = -\hat{\Delta}^T(-k). \tag{3.10}
$$

As the gap function combines two spin-$\frac{1}{2}$ particles, it is useful to split it into spin singlet and triplet combinations, in analogy to the addition of two spins treated in quantum mechanics. The spin singlet gap function is

$$
\Delta = \frac{1}{2} \left(\Delta_{\uparrow\downarrow} - \Delta_{\downarrow\uparrow} \right) \tag{3.11}
$$

and the spin triplet order parameters are usually written as x,y, and z-components of the $\boldsymbol{d}$-vector

$$d_x = \frac{1}{2}\left(\Delta_{\downarrow\downarrow} - \Delta_{\uparrow\uparrow}\right) \tag{3.12}$$

$$d_y = \frac{i}{2}\left(\Delta_{\downarrow\downarrow} + \Delta_{\uparrow\uparrow}\right) \tag{3.13}$$

$$d_z = \frac{1}{2}\left(\Delta_{\uparrow\downarrow} + \Delta_{\downarrow\uparrow}\right). \tag{3.14}$$

With these definitions, the gap function can then be written in the more compact form [88],

$$\hat{\Delta}(\boldsymbol{k}) = (\Delta(\boldsymbol{k})\hat{\sigma}_0 + \boldsymbol{d}(\boldsymbol{k}) \cdot \hat{\boldsymbol{\sigma}})\,i\hat{\sigma}_y. \tag{3.15}$$

$\hat{\boldsymbol{\sigma}}$ is the vector containing the three Pauli matrices $\hat{\sigma}_{x,y,z}$ acting on spin.

An important aspect of the spin singlet and triplet classification is that the transformation in Eq. (3.10) can be applied to spin singlet and triplet components individually,

$$(\Delta(\boldsymbol{k})\hat{\sigma}_0 + \boldsymbol{d}(\boldsymbol{k}) \cdot \hat{\boldsymbol{\sigma}})\,i\hat{\sigma}_y = -i\hat{\sigma}_y^T\left(\Delta(-\boldsymbol{k})\hat{\sigma}_0^T + \boldsymbol{d}(-\boldsymbol{k}) \cdot \hat{\boldsymbol{\sigma}}^T\right)$$
$$= (\Delta(-\boldsymbol{k})\hat{\sigma}_0 - \boldsymbol{d}(-\boldsymbol{k}) \cdot \hat{\boldsymbol{\sigma}})\,i\hat{\sigma}_y, \tag{3.16}$$

which implies that the spin singlet gap function is even in reciprocal space, $\Delta(\boldsymbol{k}) = \Delta(-\boldsymbol{k})$, whereas the spin triplet order parameters are odd, $\boldsymbol{d}(\boldsymbol{k}) = -\boldsymbol{d}(-\boldsymbol{k})$.

The mean-field Hamiltonian is quadratic in fermion operators, but it contains pairs of creation or annihilation operators. It is therefore useful to go to the Nambu basis and write down the Bogoliubov-de-Gennes (BdG) Hamiltonian in the form

$$H_{\mathrm{MF}} = \sum_{\boldsymbol{k}} \frac{1}{2}\boldsymbol{\Psi}_{\boldsymbol{k}}^{\dagger}\begin{pmatrix} \xi(\boldsymbol{k})\hat{\sigma}_0 & \hat{\Delta}(\boldsymbol{k}) \\ \hat{\Delta}^{\dagger}(\boldsymbol{k}) & -\xi(\boldsymbol{k})\hat{\sigma}_0 \end{pmatrix}\boldsymbol{\Psi}_{\boldsymbol{k}} + \mathrm{const}, \tag{3.17}$$

with the four component Nambu spinor $\boldsymbol{\Psi}_{\boldsymbol{k}} = \left(c_{\boldsymbol{k}\uparrow}, c_{\boldsymbol{k}\downarrow}, c_{-\boldsymbol{k}\uparrow}^{\dagger}, c_{-\boldsymbol{k}\downarrow}^{\dagger}\right)^T$. One can consider this transformation as treating electron and hole degrees of freedom explicitly, leading to a doubling of the degrees of freedom, which is compensated by the requirement of particle-hole symmetry. Eq. (3.17) is then diagonalized by the Bogoliubov transformation

$$\boldsymbol{\Psi}_{\boldsymbol{k}} = \begin{pmatrix} \hat{u}_{\boldsymbol{k}} & \hat{v}_{\boldsymbol{k}} \\ \hat{v}_{-\boldsymbol{k}}^* & \hat{u}_{-\boldsymbol{k}}^* \end{pmatrix}\boldsymbol{A}_{\boldsymbol{k}}, \tag{3.18}$$

where $\hat{u}_{\boldsymbol{k}}$ and $\hat{v}_{\boldsymbol{k}}$ are 2×2 matrices in spin space. The new operators $\boldsymbol{A}_{\boldsymbol{k}}^{\dagger} = \left(\gamma_{\boldsymbol{k}\uparrow}^{\dagger}, \gamma_{\boldsymbol{k}\downarrow}^{\dagger}, \gamma_{-\boldsymbol{k}\uparrow}, \gamma_{-\boldsymbol{k}\downarrow}\right)$ create and annihilate the Bogoliubov quasiparticles, which

describe the excitations of the superconducting state. Inverting the unitary transformation in Eq. (3.18) reveals that the quasiparticles are formed by a linear combination of particles and holes. Their excitation energies $E_\pm(\boldsymbol{k})$ always come in pairs $E_\pm(\boldsymbol{k})$ and $-E_\pm(-\boldsymbol{k})$ due to particle-hole symmetry. The spectrum of the Bogoliobov excitations is given by

$$E(\boldsymbol{k}) = \sqrt{\xi(\boldsymbol{k})^2 + |\Delta(\boldsymbol{k})|^2}, \qquad (3.19)$$

for spin singlet pairing and

$$E(\boldsymbol{k})_\pm = \sqrt{\xi(\boldsymbol{k})^2 + |\boldsymbol{d}(\boldsymbol{k})|^2 \pm |\boldsymbol{d}(\boldsymbol{k}) \times \boldsymbol{d}^*(\boldsymbol{k})|} \qquad (3.20)$$

for spin triplet pairing. The degeneracy of the excitation energies in the spin triplet case is lifted when $\boldsymbol{d}(\boldsymbol{k}) \times \boldsymbol{d}^*(\boldsymbol{k})$ is nonzero, which requires $\boldsymbol{d}(\boldsymbol{k}) \neq \boldsymbol{d}^*(\boldsymbol{k})$. That case is called non-unitary pairing.

The unitary transformation matrix of the Bogoliubov transformation can be determined by requiring that the γ operators obey the fermionic anti-commutation relations and that it actually diagonalizes the Hamiltonian. Restricting to unitary pairing, the solution for $\hat{u}_{\boldsymbol{k}}$ and $\hat{v}_{\boldsymbol{k}}$ takes the form:

$$\hat{u}_{\boldsymbol{k}} = \frac{(E(\boldsymbol{k}) + \xi(\boldsymbol{k}))\hat{\sigma}_0}{\sqrt{2E(\boldsymbol{k})(E(\boldsymbol{k}) + \xi(\boldsymbol{k}))}} \qquad \hat{v}_{\boldsymbol{k}} = \frac{-\hat{\Delta}(\boldsymbol{k})}{\sqrt{2E(\boldsymbol{k})(E(\boldsymbol{k}) + \xi(\boldsymbol{k}))}}. \qquad (3.21)$$

To get a qualitative picture of the Bogoliubov quasiparticles and their excitation spectrum, it is useful to first consider the transformation in the absence of pairing. In that case, the Hamiltonian in Eq. (3.17) is already diagonal and represents a doubling of the band dispersion $\xi(\boldsymbol{k})$, where one copy is mirrored at the chemical potential. One branch describes holes, the other one electrons, and they cross at zero energy. The term $\hat{v}_{\boldsymbol{k}}$ is zero, and the Bogoliubov quasiparticles $\gamma^\dagger(\gamma)$ describe electrons (holes). A non-zero $\hat{\Delta}(\boldsymbol{k})$ then plays the role of a "hybridization" between the electron and hole bands and an excitation gap opens at the crossing. This excitation gap leads to a finite energy cost to create an excitation above the ground state. Inverting the Bogoliubov transformation in Eq. (3.18) reveals that the Bogoliubov quasiparticles now mix electrons and holes. When the band energy $\xi(\boldsymbol{k})$ is much larger than the gap $\Delta(\boldsymbol{k})$, the mixing is very small and the quasiparticles are almost purely electron- or hole-like. Close to zero energy the mixing is more pronounced.

One of the main goals in Papers I, II, and V in this thesis is to determine the gap function given a specific interaction. With the help of the quasiparticle operators it is possible to do just that. Making use of the definition in Eq. (3.8) and replacing the electron annihilation operators by the new quasiparticles

yields

$$
\Delta_{\sigma\bar{\sigma}}(\boldsymbol{k}) = -\sum_{\boldsymbol{k}'}\sum_{\tau\bar{\tau}}V_{\sigma\bar{\sigma}\tau\bar{\tau}}(\boldsymbol{k},\boldsymbol{k}')\langle c_{-\boldsymbol{k}',\tau}c_{\boldsymbol{k}',\bar{\tau}}\rangle
$$

$$
= -\sum_{\boldsymbol{k}'}\sum_{\tau\bar{\tau}}V_{\sigma\bar{\sigma}\tau\bar{\tau}}(\boldsymbol{k},\boldsymbol{k}')\times
$$

$$
\sum_{s\bar{s}}\left(-u_{\boldsymbol{k}'\bar{\tau}s}v_{-\boldsymbol{k}'\tau\bar{s}}\langle\gamma_{\boldsymbol{k}'s}\gamma^{\dagger}_{\boldsymbol{k}'\bar{s}}\rangle + v_{-\boldsymbol{k}'\tau s}u_{v\bar{\tau}s}\langle\gamma^{\dagger}_{\boldsymbol{k}'\bar{s}}\gamma_{\boldsymbol{k}'s}\rangle\right), \qquad (3.22)
$$

The expectation values of the quasiparticles are evaluated based on their fermionic nature. Using

$$
\langle\gamma^{\dagger}_{\boldsymbol{k}'s}\gamma_{\boldsymbol{k}'\bar{s}}\rangle = n_F(E(\boldsymbol{k}'))\delta_{s\bar{s}}, \qquad (3.23)
$$

where $n_F(E)$ is the Fermi-Dirac distribution and $\delta_{s,\bar{s}}$ a Kronecker delta, the expectation values can be evaluated to give

$$
\Delta_{\sigma\bar{\sigma}}(\boldsymbol{k}) = -\sum_{\boldsymbol{k}'}\sum_{\tau\bar{\tau}}V_{\sigma\bar{\sigma}\tau\bar{\tau}}(\boldsymbol{k},\boldsymbol{k}')\sum_{s}-u_{\boldsymbol{k}'\bar{\tau}s}v_{-\boldsymbol{k}'\tau s}\left(1-2n_F(E(\boldsymbol{k}'))\right) \qquad (3.24)
$$

$$
= -\sum_{\boldsymbol{k}'}\sum_{\tau\bar{\tau}}V_{\sigma\bar{\sigma}\tau\bar{\tau}}(\boldsymbol{k},\boldsymbol{k}')\left(-\frac{\Delta_{\tau\bar{\tau}}(-\boldsymbol{k}')}{2E(\boldsymbol{k}')}\tanh\left(\frac{E(\boldsymbol{k}')}{2k_BT}\right)\right), \qquad (3.25)
$$

where the solution for $\hat{u}_{\boldsymbol{k}}$ and $\hat{v}_{\boldsymbol{k}}$ in the case of unitary pairing was used to obtain Eq. (3.25).

This is the generalized gap equation that allows to solve for the order parameter. For numerical purposes, the order parameter is calculated from the more general Eq. (3.24). Starting from an initial guess of $\hat{\Delta}$ it is possible to diagonalize the mean-field Hamiltonian and obtain $\hat{u}_{\boldsymbol{k}}, \hat{v}_{\boldsymbol{k}}$ and $E(\boldsymbol{k})$, which in turn allows to calculate a new $\hat{\Delta}(\boldsymbol{k})$, taking into account the specific form of the interaction. This process can be iterated until the order parameter does no longer change between iterations, signaling conversion. The obtained order parameter then corresponds to a (possibly local) minimum of the free energy and care needs to be taken to identify the global stable solution.

3.2 Multiorbital superconductivity

The previous derivation relies on an interaction written in the band picture, where the normal state Hamiltonian $\hat{h}_0$ is diagonal and only has spin degrees of freedom. However, all the systems studied in this thesis are characterized by possessing several orbital (or sublattice) degrees of freedom with interactions $V^{l\bar{l}m\bar{m}}_{\sigma\bar{\sigma}\tau\bar{\tau}}\boldsymbol{k},\boldsymbol{k}'$ defined in an orbital basis with additional orbital labels l, $\bar{l}$, m, and $\bar{m}$.

In such multiorbital systems, the BdG Hamiltonian has to be extended to include orbital degrees of freedom in addition to the spin degrees of freedom.

The normal state Hamiltonian $\hat{h}_0(\boldsymbol{k})$ and the gap function $\hat{\Delta}(\boldsymbol{k})$ then consist of $2n \times 2n$ matrices, where n is the number of orbitals. The BdG Hamiltonian is consequently written as

$$H_{\mathrm{MF}} = \sum_{\boldsymbol{k}} \boldsymbol{\Psi}_{\boldsymbol{k}}^{\dagger} \begin{pmatrix} \hat{h}_0(\boldsymbol{k}) & \hat{\Delta}(\boldsymbol{k}) \\ \hat{\Delta}^{\dagger}(\boldsymbol{k}) & -\hat{h}_0^*(-\boldsymbol{k}) \end{pmatrix} \boldsymbol{\Psi}_{\boldsymbol{k}}, \tag{3.26}$$

in terms of the multiorbital Nambu spinor $\boldsymbol{\Psi}_{\boldsymbol{k}} = \left(\boldsymbol{\psi}_{\boldsymbol{k}}, \boldsymbol{\psi}_{-\boldsymbol{k}}^{\dagger} \right)^T$ with $\boldsymbol{\psi}_{\boldsymbol{k}} = \left(c_{\boldsymbol{k}1\uparrow}, c_{\boldsymbol{k}1\downarrow}, \ldots, c_{\boldsymbol{k}n\uparrow}, c_{\boldsymbol{k}n\downarrow} \right)^T$, where the creation operators $c_{\boldsymbol{k}m\sigma}^{\dagger}$ gained an additional orbital index $m = 1, \ldots, n$. One of the key differences to the band basis is that the normal state Hamiltonian $\hat{h}_0$ is no longer diagonal, but incorporates interorbital and spin-flip hopping terms. Likewise, the pairing matrix $\hat{\Delta}$ can include intra- and interorbital pairing terms of either spin singlet or triplet nature.

The gap functions are defined in a similar manner to Eq. (3.8),

$$\Delta_{\sigma\bar{\sigma}}^{l\bar{l}}(\boldsymbol{k}) = -\sum_{\boldsymbol{k}'} \sum_{\tau\bar{\tau}} \sum_{m\bar{m}} V_{\sigma\bar{\sigma}\tau\bar{\tau}}^{l\bar{l}m\bar{m}}(\boldsymbol{k},\boldsymbol{k}') \langle c_{-\boldsymbol{k}'m\tau} c_{\boldsymbol{k}'\bar{m}\bar{\tau}} \rangle. \tag{3.27}$$

Correspondingly, a generalization of the Bogoliubov transformation $\boldsymbol{\Psi}_{\boldsymbol{k}} = \hat{\mathcal{U}}_{\boldsymbol{k}} \mathcal{A}_{\boldsymbol{k}}$ diagonalizes the multiorbital BdG Hamiltonian and allows to define self-consistency equations of the form

$$\Delta_{\sigma\bar{\sigma}}^{l\bar{l}}(\boldsymbol{k}) = -\sum_{\boldsymbol{k}'} \sum_{\tau\bar{\tau}} V_{\sigma\bar{\sigma}\tau\bar{\tau}}^{l\bar{l}m\bar{m}}(\boldsymbol{k},\boldsymbol{k}') \sum_{s} \sum_{o} \mathcal{U}_{\boldsymbol{k}'\tau s}^{mo} \mathcal{U}_{\boldsymbol{k}'\bar{\tau}s}^{\bar{m}o\,*} \left(1 - n_F(E_{os}(\boldsymbol{k}')) \right). \tag{3.28}$$

In general, there exists another unitary transformation $\hat{U}_{\boldsymbol{k}}$ relating the orbital to the band basis. This transformation diagonalizes the normal state Hamiltonian $\hat{U}_{\boldsymbol{k}} \hat{h}_0(\boldsymbol{k}) \hat{U}_{\boldsymbol{k}}^{\dagger} = \hat{h}_0^B(\boldsymbol{k})$, where the superscript B signifies the diagonal band basis. It furthermore relates the spinors through the identity $\boldsymbol{\psi}_{\boldsymbol{k}}^B = \hat{U}_{\boldsymbol{k}} \boldsymbol{\psi}_{\boldsymbol{k}}$. The same transformation does, however, not automatically diagonalize the pairing matrix. Instead, the pairing matrix in the band basis

$$\hat{\Delta}^B(\boldsymbol{k}) = \hat{U}_{\boldsymbol{k}} \hat{\Delta}(\boldsymbol{k}) \hat{U}_{-\boldsymbol{k}}^T \tag{3.29}$$

generally features intra- and interband pairing.

Superconductivity arises as a Fermi surface instability where it is energetically favorable to form Cooper pairs from electrons of opposite momentum and small energies at the Fermi energy [2]. This is most naturally formulated in the band basis and is expressed as a band pairing matrix without interband terms. From a generic pairing matrix in the orbital basis it is not readily apparent, if interband pairing is present or not. A simple criterion to check this is the so-called superconducting fitness [89, 5, 6]. Here I want to present a heuristic definition of the superconducting fitness first detailed by Ramires

and Sigrist[5]. Given a simple spin degenerate two band model, defined by

$$\hat{h}_0^B = \begin{pmatrix} \varepsilon_1 \hat{\sigma}_0 & 0 \\ 0 & \varepsilon_2 \hat{\sigma}_0 \end{pmatrix} \qquad \text{and} \qquad \hat{\Delta}^B = \begin{pmatrix} \hat{\Delta}_1 & \hat{\Delta}_{12} \\ \hat{\Delta}_{21} & \hat{\Delta}_2 \end{pmatrix}, \qquad (3.30)$$

vanishing interband pairings $\hat{\Delta}_{12} = \hat{\Delta}_{21} = 0$ ensure that the normal state and the pairing Hamiltonian commute for any $\varepsilon_{1,2}$. Transforming this condition,

$$\hat{h}_0^B(\mathbf{k})\hat{\Delta}^B(\mathbf{k}) = \hat{\Delta}^B(\mathbf{k})\hat{h}_0^B(\mathbf{k}), \qquad (3.31)$$

back into the orbital basis using the inverse transformation $\hat{U}_{\mathbf{k}}^\dagger$ gives for the left hand side

$$\hat{U}_{\mathbf{k}}^\dagger \hat{h}_0^B(\mathbf{k})\hat{U}_{\mathbf{k}}\hat{U}_{\mathbf{k}}^\dagger\hat{\Delta}^B(\mathbf{k})\hat{U}_{-\mathbf{k}}^* = \hat{h}_0(\mathbf{k})\hat{\Delta}(\mathbf{k}). \qquad (3.32)$$

For the right hand side, the transformation relies on the fact that $\hat{h}_0^B$ is inversion symmetric (otherwise the eigenvalues would not be double degenerate) and that its eigenvalues are real to yield

$$\hat{U}_{\mathbf{k}}^\dagger \hat{\Delta}^B(\mathbf{k})\hat{U}_{-\mathbf{k}}^*\hat{U}_{-\mathbf{k}}^T\hat{h}_0^B(\mathbf{k})\hat{U}_{-\mathbf{k}}^* = \hat{\Delta}(\mathbf{k}) \left(\hat{U}_{-\mathbf{k}}^\dagger \hat{h}_0^B(-\mathbf{k})\hat{U}_{-\mathbf{k}} \right)^* = \hat{\Delta}(\mathbf{k})\hat{h}_0^*(-\mathbf{k}). \qquad (3.33)$$

Taken together, this gives the criterion that there exists no interband pairing, if the modified commutator vanishes

$$\hat{h}_0(\mathbf{k})\hat{\Delta}(\mathbf{k}) - \hat{\Delta}(\mathbf{k})\hat{h}_0^*(-\mathbf{k}) = \left[\hat{h}_0(\mathbf{k})\hat{\Delta}(\mathbf{k}) \right]^* = 0. \qquad (3.34)$$

The superconducting fitness function $\hat{F}_C(\mathbf{k})$ can be considered as a measure of the deviation from this pure intraband pairing state

$$\left[\hat{\tilde{h}}_0(\mathbf{k}), \hat{\Delta}(\mathbf{k}) \right]^* = \hat{F}_C(\mathbf{k})\mathrm{i}\hat{\sigma}_y, \qquad (3.35)$$

where the additional term $\mathrm{i}\hat{\sigma}_y$ is a convention to simplify calculations and $\hat{\tilde{h}}_0$ includes some additional normalizations[6].

Beyond this heuristic approach it has been shown, first using a perturbative approach[5] and later in a closed form[6], that a finite value of the superconducting fitness $\hat{F}_C(\mathbf{k})$ leads to a suppression of the critical temperature T_C proportional to the Fermi surface average $\langle \mathrm{Tr}(|\hat{F}_C|^2) \rangle_{FS}$. Furthermore, one can also use the anti-commutator

$$\left\{ \hat{\tilde{h}}_0(\mathbf{k}), \hat{\Delta}(\mathbf{k}) \right\}^* = \hat{F}_A(\mathbf{k})\mathrm{i}\hat{\sigma}_y \qquad (3.36)$$

to define a second superconducting fitness function $\hat{F}_A(\mathbf{k})$ which gives a non-zero contribution $\langle \mathrm{Tr}(|\hat{F}_A|^2) \rangle_{FS}$ only in the presence of intraband pairing[6].

The superconducting fitness functions thereby allow to check the compatibility of a certain pairing state with the normal state Hamiltonian in the orbital

basis. Any term in the normal state Hamiltonian that generates a non-zero $\hat{F}_C$ will be detrimental to pairing in that channel, whereas a finite $\hat{F}_A$ favors a certain pairing. Further extensions of the concept allow statements on the stability of a certain pairing state to disorder, even if the pairing generates nodes in the band basis [7, 8].

3.3 A block Hamiltonian for spin singlet pairing on the harmonic honeycomb lattices

In the harmonic honeycomb lattices studied in Paper I, we restrict the superconductivity to spin singlet pairing, which only leaves the sublattice degrees of freedom in the Hamiltonian. To study the whole range of harmonic honeycomb lattices on an equal footing, we consider only nearest neighbor hopping and pairing, which allows to express the Hamiltonian for all lattices in a similar block form. In this section, I present the mean-field decoupling of that Hamiltonian and introduce the self-consistency equations for the order parameter.

The derivation of the block Hamiltonian relies on some concepts of the lattice structure of the harmonic honeycomb lattices introduced in Sec. 2.2. Those lattices, labeled $\mathcal{H}\langle n \rangle$, can be considered as a series of strips of n complete honeycombs, or equivalently strips of $n+1$ zigzag chains, where the strips are periodically rotated against each other around the connecting twist bonds. The two different rotations of the honeycomb lattice correspond to the two different choices of zigzag nearest neighbor vectors, $\boldsymbol{a}_{2/3}$ for an unrotated and $\boldsymbol{a}'_{2/3}$ for a rotated honeycomb, as defined in Sec. 2.2. The horizontal bonds stay the same throughout $\boldsymbol{a}_1 = \boldsymbol{a}'_1$. The unit cell of these structures contains $2(n+1) \times 2$ sites, which is built up of two sites for $n+1$ zigzag strips of two different rotations. The idea for the block Hamiltonian is then to group all terms involving nearest neighbors vectors along one zigzag chain into a block, which is connected to other chains by blocks involving the horizontal bonds. To this end, the lattice sites are grouped into equally many a and b sites, where all nearest neighbor vectors point from an a to a b site. By this construction, each zigzag chain consists of exactly one a and one b site of the unit cell.

The Hamiltonian used as the starting point to model spin singlet superconductivity in the harmonic honeycomb lattices in Paper I consists of a nearest neighbor hopping of strength t, a chemical potential μ, and a nearest neighbor Heisenberg interaction of strength J,

$$H = -t \sum_{\langle i,j \rangle, \sigma} \left(b^{\dagger}_{j,\sigma} a_{i,\sigma} + h.c. \right) + \mu \sum_{i,\sigma} \left(a^{\dagger}_{i,\sigma} a_{i,\sigma} + b^{\dagger}_{i,\sigma} b_{i,\sigma} \right)$$

$$+ J \sum_{\langle i,j \rangle} \left(\boldsymbol{S}_i \cdot \boldsymbol{S}_j - \frac{1}{4} n_i n_j \right), \tag{3.37}$$

where electrons of spin σ on an a (b) site at position $\boldsymbol{r}_i$ are created by $a^\dagger_{i,\sigma}$ ($b^\dagger_{i,\sigma}$). $\langle i,j \rangle$ denotes a sum over nearest neighbors i and j. The interaction term can be rewritten in terms of a nearest neighbor spin singlet

$$
\begin{aligned}
\boldsymbol{S}_i \cdot \boldsymbol{S}_j - \frac{1}{4} n_i n_j &= \frac{1}{2} \left(-a^\dagger_{i,\uparrow} a_{i,\uparrow} b^\dagger_{j,\downarrow} b_{j,\downarrow} + a^\dagger_{i,\uparrow} a_{i,\downarrow} b^\dagger_{j,\downarrow} b_{j,\uparrow} \right. \\
&\qquad \left. + a^\dagger_{i,\downarrow} a_{i,\uparrow} b^\dagger_{j,\uparrow} b_{j,\downarrow} - a^\dagger_{i,\downarrow} a_{i,\downarrow} b^\dagger_{j,\uparrow} b_{j,\uparrow} \right) \\
&= -\frac{1}{\sqrt{2}} \left(a^\dagger_{i,\uparrow} b^\dagger_{j,\downarrow} - a^\dagger_{i,\downarrow} b^\dagger_{j,\uparrow} \right) \frac{1}{\sqrt{2}} \left(a_{i,\downarrow} b_{j,\uparrow} - a_{i,\uparrow} b_{j,\downarrow} \right) \\
&= -s^\dagger_{ij} s_{ij}
\end{aligned}
\tag{3.38}
$$

The system is periodic in all three directions, which allows to perform a Fourier transform with the convention

$$
c^\dagger_{\boldsymbol{r}_i,\sigma} = \frac{1}{\sqrt{N}} \sum_{\boldsymbol{k}} e^{i\boldsymbol{k}\cdot\boldsymbol{r}_i} c^\dagger_{l,\boldsymbol{k},\sigma} \qquad\qquad \delta_{\boldsymbol{k},\boldsymbol{k}'} = \frac{1}{N} \sum_{\boldsymbol{r}_i} e^{i(\boldsymbol{k}-\boldsymbol{k}')\cdot\boldsymbol{r}_i}, \tag{3.39}
$$

where c is either a or b, depending on the site, and l labels the zigzag chains within a unit cell, $l = 1, \ldots, n+1$. The normal state Hamiltonian then directly decouples into intra-zigzag and inter-zigzag terms

$$
\begin{aligned}
H^0_{intra} = &-t \sum_{\boldsymbol{k},l,\sigma} \sum_{j=2,3} \left(b^\dagger_{l,\boldsymbol{k},\sigma} a_{l,\boldsymbol{k},\sigma} e^{i\boldsymbol{k}\cdot\boldsymbol{a}_j} + h.c. \right) \\
&+ \mu \sum_{l,\boldsymbol{k},\sigma} \left(a^\dagger_{l,\boldsymbol{k},\sigma} a_{l,\boldsymbol{k},\sigma} + b^\dagger_{l,\boldsymbol{k},\sigma} b_{l,\boldsymbol{k},\sigma} \right),
\end{aligned}
\tag{3.40}
$$

$$
H^0_{inter} = -t \sum_{\boldsymbol{k},l,\sigma} \left(b^\dagger_{l+1,\boldsymbol{k},\sigma} a_{l,\boldsymbol{k},\sigma} e^{i\boldsymbol{k}\cdot\boldsymbol{a}_1} + h.c. \right)
\tag{3.41}
$$

where the nearest neighbor vectors $\boldsymbol{a}_j$ need to be adjusted to be either unrotated or rotated. The interaction Hamiltonian is simplified through the mean-field decoupling by defining the order parameters

$$
\Delta_{l,j} = -\frac{J}{2} \sum_{\boldsymbol{k}} e^{i\boldsymbol{k}\cdot\boldsymbol{a}_j} \langle a_{l,\boldsymbol{k},\downarrow} b_{l+\delta_{1,j},-\boldsymbol{k},\uparrow} - a_{l,\boldsymbol{k},\uparrow} b_{l+\delta_{1,j},-\boldsymbol{k},\downarrow} \rangle,
\tag{3.42}
$$

with the Kronecker delta $\delta_{i,j}$. Introducing the shorthand notations

$$
t'(\boldsymbol{k}) = -t \sum_{j=2,3} e^{i\boldsymbol{k}\cdot\boldsymbol{a}_j} \qquad\qquad t''(\boldsymbol{k}) = -t e^{i\boldsymbol{k}\cdot\boldsymbol{a}_1}
\tag{3.43}
$$

$$
\tilde{\Delta}_l(\boldsymbol{k}) = \sum_{j=2,3} \left(\Delta_{l,j} e^{-i\boldsymbol{k}\cdot\boldsymbol{a}_j} \right) \qquad\qquad \tilde{\Delta}_{l,1}(\boldsymbol{k}) = \left(\Delta_{l,1} e^{-i\boldsymbol{k}\cdot\boldsymbol{a}_1} \right)
\tag{3.44}
$$

then allows to define the full inter- and intra-zigzag Hamiltonians

$$H_l^{intra} = \boldsymbol{\psi}_l^\dagger \begin{pmatrix} \mu & t'^*(\boldsymbol{k}) & 0 & \tilde{\Delta}_l(\boldsymbol{k}) \\ t'(\boldsymbol{k}) & \mu & \tilde{\Delta}_l(-\boldsymbol{k}) & 0 \\ 0 & \tilde{\Delta}_l^*(-\boldsymbol{k}) & -\mu & -t'^*(\boldsymbol{k}) \\ \tilde{\Delta}_l^*(\boldsymbol{k}) & 0 & -t'(\boldsymbol{k}) & -\mu \end{pmatrix} \boldsymbol{\psi}_l, \qquad (3.45)$$

$$H_l^{inter} = \boldsymbol{\psi}_{l+1}^\dagger \begin{pmatrix} 0 & 0 & 0 & 0 \\ -t''(\boldsymbol{k}) & 0 & \tilde{\Delta}_{l,1}(-\boldsymbol{k}) & 0 \\ 0 & 0 & 0 & 0 \\ \tilde{\Delta}_{l,1}^*(\boldsymbol{k}) & 0 & t''(\boldsymbol{k}) & 0 \end{pmatrix} \boldsymbol{\psi}_l, \qquad (3.46)$$

where the Nambu spinor $\boldsymbol{\psi}_l^\dagger = \left(a_{l,\boldsymbol{k},\uparrow}^\dagger, b_{l,\boldsymbol{k},\uparrow}^\dagger, a_{l,-\boldsymbol{k},\downarrow}, b_{l,-\boldsymbol{k},\downarrow} \right)$ runs over the two sites making up each zigzag chain. Altogether, this achieves the aspired splitting of the full Hamiltonian into block form

$$H_{MF} = \left(\boldsymbol{\psi}_1^\dagger, \dots, \boldsymbol{\psi}_{n+1}^\dagger \right) \begin{pmatrix} \hat{h}_1^{intra} & \hat{h}_1^{inter\dagger} & 0 & \cdots & \hat{h}_{n+1}^{inter} \\ \hat{h}_1^{inter} & \hat{h}_2^{intra} & \hat{h}_2^{inter\dagger} & & 0 \\ 0 & \hat{h}_2^{inter} & \ddots & & \vdots \\ \vdots & & & \hat{h}_n^{intra} & \hat{h}_n^{inter\dagger} \\ \hat{h}_{n+1}^{inter\dagger} & 0 & \cdots & \hat{h}_n^{inter} & \hat{h}_{n+1}^{intra} \end{pmatrix} \begin{pmatrix} \boldsymbol{\psi}_1 \\ \vdots \\ \boldsymbol{\psi}_{n+1} \end{pmatrix}, \qquad (3.47)$$

where each $\hat{h}^{intra}$ block corresponds to one of the $n+1$ zigzag chains within each unit cell of the $\mathcal{H}\langle n\rangle$ lattice. In this way, the nearest neighbor vectors that differ between unrotated and rotated zigzag chains only enter in the $\hat{h}^{intra}$ blocks, such that a twist at site i is easily implemented by just changing the nearest neighbor vectors in the corresponding exponentials in $\hat{h}_{l>i}^{intra}$. The Hamiltonian in Eq. (3.47) is thus adaptable to study trends along the whole series of harmonic honeycomb lattices.

As detailed in section 3.2, the order parameter can be determined self-consistently by diagonalizing $\hat{h}_{MF}$ and expressing the expectation values in Eq. (3.42) in terms of the quasiparticle operators with the help of the unitary transformation $\hat{\mathcal{U}}$. As the order parameter splits into intra- and inter-zigzag chain pairing

$$\Delta_{l,j} = -\frac{J}{2} \sum_{\boldsymbol{k}} \sum_{j=2,3} \left(e^{-i\boldsymbol{k}\cdot\boldsymbol{a}_j} \langle a_{l,-\boldsymbol{k},\downarrow} b_{l,\boldsymbol{k},\uparrow} \rangle - e^{i\boldsymbol{k}\cdot\boldsymbol{a}_j} \langle a_{l,\boldsymbol{k},\uparrow} b_{l,-\boldsymbol{k},\downarrow} \rangle \right)$$

$$+ -\frac{J}{2} \sum_{\boldsymbol{k}} \left(e^{-i\boldsymbol{k}\cdot\boldsymbol{a}_1} \langle a_{l,-\boldsymbol{k},\downarrow} b_{l+1,\boldsymbol{k},\uparrow} \rangle - e^{i\boldsymbol{k}\cdot\boldsymbol{a}_j} \langle a_{l,\boldsymbol{k},\uparrow} b_{l+1,-\boldsymbol{k},\downarrow} \rangle \right), \qquad (3.48)$$

the self-consistency equations require slightly different entries of the unitary matrix. The intra-zigzag chain pairing on bonds $j = 2, 3$ is calculated from

$$\Delta_{l,j} = -\frac{J}{2} \sum_{\boldsymbol{k}} \left(e^{-i\boldsymbol{k}\cdot\boldsymbol{a}_j} \sum_m \mathcal{U}^*_{\boldsymbol{k}(4l-1)+3,m} \mathcal{U}_{\boldsymbol{k}(4l-1)+2,m} n_F(E_m(\boldsymbol{k})) \right.$$
$$\left. -e^{i\boldsymbol{k}\cdot\boldsymbol{a}_j} \sum_m \mathcal{U}_{\boldsymbol{k}(4l-1)+1,m} \mathcal{U}^*_{\boldsymbol{k}(4l-1)+4,m} (1 - n_F(E_m(\boldsymbol{k}))) \right), \qquad (3.49)$$

where $m = 1, \ldots, 4(n+1)$ runs over the full Hilbert space basis. The nearest neighbor vectors $\boldsymbol{a}_j$ must be adjusted depending on whether the zigzag chain is part of an unrotated or rotated sheet. The inter-zigzag chain pairing only involves bond $j = 1$, which requires no such considerations, such that

$$\Delta_{l,1} = -\frac{J}{2} \sum_{\boldsymbol{k}} \left(e^{-i\boldsymbol{k}\cdot\boldsymbol{a}_1} \sum_m \mathcal{U}^*_{\boldsymbol{k}(4l-1)+3,m} \mathcal{U}_{\boldsymbol{k}((4l-1)+6) \bmod 2(n+1),m} n_F(E_m(\boldsymbol{k})) \right.$$
$$\left. - e^{i\boldsymbol{k}\cdot\boldsymbol{a}_1} \sum_m \mathcal{U}_{\boldsymbol{k}(4l-1)+1,m} \mathcal{U}^*_{\boldsymbol{k}((4l-1)+8) \bmod 2(n+1),m} (1 - n_F(E_m(\boldsymbol{k}))) \right).$$
$$(3.50)$$

In total, there are therefore $3(n+1)$ spin singlet nearest neighbor order parameters on the $\mathcal{H}\langle n \rangle$ harmonic honeycomb lattice. When n is large, we group the three nearest neighbor bonds around each a site in the form $\boldsymbol{\Delta}_l = (\Delta_{l,1}, \Delta_{l,2}, \Delta_{l,3})$, similarly to the approach in describing superconductivity in graphene [90, 91, 92]. For the two smallest members of the series, $n = 0$ and $n = 1$, studied in more detail in Paper I, the number of zigzag chains is small enough to consider the whole $3(n+1)$ order parameters together. In particular, for the hyperhoneycomb lattice with $n = 0$, we group the order parameter as $\boldsymbol{\Delta}_{hyper} = (\Delta_{1,1}, \Delta_{1,2}, \Delta_{1,3}, \Delta_{2,1}, \Delta_{2,2}, \Delta_{2,3})$.

In summary, the block Hamiltonian in Eq. (3.47) can be easily adjusted to describe spin singlet superconductivity on all of the harmonic honeycomb lattices. This is possible due to the restriction to purely nearest neighbor hopping and pairing. The order parameters can be self-consistently calculated from equations Eqs. (3.49) and (3.50).

3.4 Spin triplet pairing from the extended Kitaev-Heisenberg model

In Paper II, we study the spin triplet superconductivity arising from the extended Kitaev-Heisenberg model on the honeycomb lattice. This means that while there are only two sublattice degrees of freedom, we now also include spin. In this section I detail the derivation of the pairing Hamiltonian and the self-consistency equations with a particular focus on the previously not considered off-diagonal exchange.

The interacting Hamiltonian for the extended Kitaev-Heisenberg model on the honeycomb lattice, as introduced in Sec. 2.1, reads

$$H_{JK\Gamma} = \sum_{\langle i,j \rangle} \left\{ J \left(\boldsymbol{S}_i \cdot \boldsymbol{S}_j - \frac{1}{4} n_i n_j \right) \right.$$
$$\left. + K S_i^{\gamma(i,j)} S_j^{\gamma(i,j)} + \Gamma \left(S_i^{\alpha(i,j)} S_j^{\beta(i,j)} + S_i^{\beta(i,j)} S_j^{\alpha(i,j)} \right) \right\}. \qquad (3.51)$$

$\boldsymbol{S}_i$ represents the effective spin moment $j_{\text{eff}} = \frac{1}{2}$ present at every site i of the honeycomb lattice. It can be written in terms of the fermionic creation and annihilation operators as $S_i^\gamma = c_{i\sigma o}^\dagger \hat{\sigma}_{\sigma\bar{\sigma}}^\gamma c_{i\bar{\sigma}o}$, where $\hat{\sigma}^\gamma$ represents the $\gamma = x, y, z$ Pauli matrices in spin space and $c_{i\sigma o}^\dagger$ creates an electron at site i on sublattice $o = a, b$ with (pseudo-)spin σ. The functions $\alpha(i,j)$, $\beta(i,j)$, and $\gamma(i,j)$ can be $\{x, y, z\}$, depending on the bond between nearest neighbor sites $\langle i, j \rangle$, where $\alpha(i,j) \neq \beta(i,j) \neq \gamma(i,j)$. This means that each bond $\langle i, j \rangle$ comes with a specific $\gamma \in \{x, y, z\}$ that enters in the Kitaev interaction. The off-diagonal interaction term then features the other two elements of the spin vector α and β, as detailed in Sec. 2.1.

The Heisenberg spin term can be rewritten in terms of a nearest neighbor spin singlet as shown in Sec. 3.3. The other two interactions can similarly be cast into a form involving the nearest neighbor spin singlet and triplet operators

$$s_{ij}^\dagger = \frac{1}{\sqrt{2}} \sum_{\sigma,\bar{\sigma}} c_{i\sigma a}^\dagger c_{j\bar{\sigma}b}^\dagger \mathrm{i} \left(\hat{\sigma}_y \hat{\sigma}_0 \right)_{\sigma\bar{\sigma}}, \qquad (3.52)$$

$$t_{ij}^{\alpha\dagger} = \frac{1}{\sqrt{2}} \sum_{\sigma,\bar{\sigma}} c_{i\sigma a}^\dagger c_{j\bar{\sigma}b}^\dagger \mathrm{i} \left(\hat{\sigma}_y \hat{\sigma}_\alpha \right)_{\sigma\bar{\sigma}}, \qquad (3.53)$$

where i and j belong to neighboring sites. In terms of these operators, the Kitaev term on a z-bond is written as [33]

$$-S_i^z S_j^z = \frac{1}{4} s_{ij}^\dagger s_{ij} - t_{ij}^{x\dagger} t_{ij}^x - t_{ij}^{y\dagger} t_{ij}^y + t_{ij}^{z\dagger} t_{ij}^z. \qquad (3.54)$$

The Kitaev terms for the other two bonds are of the same form, with the plus sign in front of the corresponding spin triplet operators. The off-diagonal in-

teraction can be reformulated purely in terms of the spin triplet operators:

$$S_i^x S_j^y + S_i^y S_j^x = \frac{i}{2}\left(c_{j\uparrow b}^\dagger c_{i\uparrow a}^\dagger c_{i\downarrow a} c_{j\downarrow a} - c_{j\downarrow b}^\dagger c_{i\downarrow a}^\dagger c_{i\uparrow a} c_{j\uparrow b}\right)$$
$$= \frac{1}{2}\left(t_{ij}^{x\dagger} t_{ij}^y + t_{ij}^{y\dagger} t_{ij}^x\right) \tag{3.55}$$

$$S_i^x S_j^z + S_i^z S_j^x = \frac{1}{4}\left(c_{j\uparrow b}^\dagger c_{i\uparrow a}^\dagger c_{i\downarrow a} c_{j\uparrow b} + c_{j\uparrow b}^\dagger c_{i\downarrow a}^\dagger c_{i\uparrow a} c_{j\uparrow b} - c_{j\downarrow b}^\dagger c_{i\uparrow a}^\dagger c_{i\downarrow a} c_{j\downarrow b}\right.$$
$$- c_{j\downarrow b}^\dagger c_{i\downarrow a}^\dagger c_{i\uparrow a} c_{j\downarrow b} + c_{j\uparrow b}^\dagger c_{i\uparrow a}^\dagger c_{i\downarrow a} c_{j\downarrow b} + c_{j\downarrow b}^\dagger c_{i\uparrow a}^\dagger c_{i\uparrow a} c_{j\uparrow b}$$
$$\left. - c_{j\uparrow b}^\dagger c_{i\downarrow a}^\dagger c_{i\downarrow a} c_{j\downarrow b} - c_{j\downarrow b}^\dagger c_{i\downarrow a}^\dagger c_{i\downarrow a} c_{j\uparrow b}\right)$$
$$= \frac{1}{2}\left(t_{ij}^{x\dagger} t_{ij}^z + t_{ij}^{z\dagger} t_{ij}^x\right) \tag{3.56}$$

$$S_i^y S_j^z + S_i^z S_j^y = \frac{i}{4}\left(-c_{j\downarrow b}^\dagger c_{i\downarrow a}^\dagger c_{i\uparrow a} c_{j\downarrow b} - c_{j\downarrow b}^\dagger c_{i\downarrow a}^\dagger c_{i\downarrow a} c_{j\uparrow b} - c_{j\uparrow b}^\dagger c_{i\uparrow a}^\dagger c_{i\uparrow a} c_{j\downarrow b}\right.$$
$$- c_{j\uparrow b}^\dagger c_{i\uparrow a}^\dagger c_{i\downarrow a} c_{j\uparrow b} - c_{j\downarrow b}^\dagger c_{i\uparrow a}^\dagger c_{i\downarrow a} c_{j\downarrow b} - c_{j\uparrow b}^\dagger c_{i\downarrow a}^\dagger c_{i\downarrow a} c_{j\downarrow b}$$
$$\left. - c_{j\downarrow b}^\dagger c_{i\uparrow a}^\dagger c_{i\uparrow a} c_{j\uparrow b} - c_{j\uparrow b}^\dagger c_{i\downarrow a}^\dagger c_{i\uparrow a} c_{j\uparrow b}\right)$$
$$= \frac{1}{2}\left(t_{ij}^{z\dagger} t_{ij}^y + t_{ij}^{y\dagger} t_{ij}^z\right). \tag{3.57}$$

Combining Eqs. (3.54)-(3.57), the interacting Hamiltonian takes the form

$$H_{JK\Gamma} = -J\sum_{\langle i,j\rangle} s_{ij}^\dagger s_{ij} - \frac{K}{4}\sum_{\langle i,j\rangle}\left(s_{ij}^\dagger s_{ij} + \varepsilon_{j,1} t_{ij}^{x\dagger} t_{ij}^x + \varepsilon_{j,2} t_{ij}^{y\dagger} t_{ij}^y + \varepsilon_{j,3} t_{ij}^{z\dagger} t_{ij}^z\right)$$
$$+ \frac{\Gamma}{2}\sum_i\left[\left(t_{i,a_1}^{z\dagger} t_{i,a_1}^y + t_{i,a_1}^{y\dagger} t_{i,a_1}^z\right) + \left(t_{i,a_2}^{x\dagger} t_{i,a_2}^z + t_{i,a_2}^{z\dagger} t_{i,a_2}^x\right) + \left(t_{i,a_3}^{y\dagger} t_{i,a_3}^x + t_{i,a_3}^{x\dagger} t_{i,a_3}^y\right)\right], \tag{3.58}$$

where $\varepsilon_{j,k} = 2\delta_{j,k} - 1$.

At half-filling, the ground state of the extended Kitaev-Heisenberg model is a magnetically ordered state for most parameters [25, 26]. To induce superconductivity, we model doping by adding mobile carriers moving according to the kinetic Hamiltonian

$$H_k = -t\sum_{\langle i,j\rangle,\sigma}\left(c_{i\sigma a}^\dagger c_{j\sigma b} + \text{H.c.}\right) + \mu\sum_{i\sigma o}\left(c_{i\sigma o}^\dagger c_{i\sigma o}\right), \tag{3.59}$$

which features nearest neighbor hopping t and a chemical potential μ. In a second step, we also consider the influence of an additional spin-orbit coupled hopping term t_{SO} in the kinetic energy,

$$H_{SO} = it_{SO}\sum_{\langle\langle i,j\rangle\rangle,\sigma,\bar\sigma,o}\left(c_{i\sigma o}^\dagger\left(\sigma_{\gamma(i,j)}\right)_{\sigma,\bar\sigma} c_{j\bar\sigma o} + \text{H.c.}\right), \tag{3.60}$$

to complement the interaction emanating from spin-orbit coupling. This hopping term is a second nearest neighbor Kane-Mele like term that involves different spin Pauli matrices $\hat{\sigma}_{\gamma(i,j)}$ on the different bonds, similar to the Kitaev interaction. The particular matrix $\gamma(i,j) = x,y,z$ is equal to the local coordinate axis whose projection onto the honeycomb plane aligns with the corresponding second nearest neighbor vector $\langle\langle i,j\rangle\rangle$ [93]. This term has first been discussed in the context of Na_2IrO_3 [93], where it arises from projecting a second nearest neighbor hopping between unlike t_{2g} orbitals via the Na ions in the center of the honeycombs onto the $j_{\text{eff}} = \frac{1}{2}$ states [94, 95]. The same underlying hopping process is also relevant in the other materials realizing the extended Kitaev-Heisenberg model [56]. The normal state Hamiltonian can be Fourier transformed and written with the help of the shorthand notation $T(\boldsymbol{k}) = -t\sum_j e^{i\boldsymbol{k}\cdot\boldsymbol{a}_j}$, and $T'_j(\boldsymbol{k}) = 2t_{SO}\sin(\boldsymbol{k}\cdot\boldsymbol{b}_j)$, where the three second nearest neighbor vectors are given by $\boldsymbol{b}_1 = \boldsymbol{a}_2 - \boldsymbol{a}_3$, $\boldsymbol{b}_2 = \boldsymbol{a}_3 - \boldsymbol{a}_1$, and $\boldsymbol{b}_3 = \boldsymbol{a}_2 - \boldsymbol{a}_1$. Writing $\boldsymbol{\psi}_{\boldsymbol{k}}^{\dagger} = \left(c_{\boldsymbol{k}\uparrow a}^{\dagger}, c_{\boldsymbol{k}\downarrow a}^{\dagger}, c_{\boldsymbol{k}\uparrow b}^{\dagger}, c_{\boldsymbol{k}\downarrow b}^{\dagger}\right)$, the kinetic Hamiltonian takes the form

$$H_0 = \sum_{\boldsymbol{k}} \boldsymbol{\psi}_{\boldsymbol{k}}^{\dagger}\hat{h}_0(\boldsymbol{k})\boldsymbol{\psi}_{\boldsymbol{k}}, \tag{3.61}$$

$$\hat{h}_0 = \begin{pmatrix} \mu + T'_3 & T'_1 - iT'_2 & T^* & 0 \\ T'_1 + iT'_2 & \mu - T'_3 & 0 & T^* \\ T & 0 & \mu - T'_3 & -T'_1 + iT'_2 \\ 0 & T & -T'_1 - iT'_2 & \mu + T'_3 \end{pmatrix}, \tag{3.62}$$

where the momentum dependence has been omitted for legibility reasons in the last equation. Performing likewise a Fourier transform of the interaction and introducing the mean-field approximation through nearest neighbor spin singlet and triplet order parameters for each of the three nearest neighbor bonds $\boldsymbol{a}_j$

$$\langle s_{\boldsymbol{a}_j}^{\dagger}\rangle = \frac{1}{\sqrt{2}}\sum_{\boldsymbol{k}}\sum_{\sigma,\bar{\sigma}}\langle c_{\boldsymbol{k}\sigma a}^{\dagger}c_{-\boldsymbol{k}\bar{\sigma}b}^{\dagger}\rangle e^{i\boldsymbol{k}\cdot\boldsymbol{a}_j}i(\hat{\sigma}_y\hat{\sigma}_0)_{\sigma\bar{\sigma}}, \tag{3.63}$$

$$\langle t_{\boldsymbol{a}_j}^{\alpha\dagger}\rangle = \frac{1}{\sqrt{2}}\sum_{\boldsymbol{k}}\sum_{\sigma,\bar{\sigma}}\langle c_{\boldsymbol{k}\sigma a}^{\dagger}c_{-\boldsymbol{k}\bar{\sigma}b}^{\dagger}\rangle e^{i\boldsymbol{k}\cdot\boldsymbol{a}_j}i(\hat{\sigma}_y\hat{\sigma}_\alpha)_{\sigma\bar{\sigma}}. \tag{3.64}$$

we can collect the spin triplet pairings in the $\boldsymbol{d}$-vector and write the pairing Hamiltonian

$$H_\Delta = \sum_{\boldsymbol{k}} \boldsymbol{\psi}_{\boldsymbol{k}}^{\dagger}\hat{\Delta}(\boldsymbol{k})\boldsymbol{\psi}_{-\boldsymbol{k}}^{*}, \tag{3.65}$$

where $\boldsymbol{\psi}_{\boldsymbol{k}}^{\dagger} = \left(c_{\boldsymbol{k}\uparrow a}^{\dagger}, c_{\boldsymbol{k}\downarrow a}^{\dagger}, c_{\boldsymbol{k}\uparrow b}^{\dagger}, c_{\boldsymbol{k}\downarrow b}^{\dagger}\right)$, and, using the shorthand expressions $\Delta(\boldsymbol{k}) = \sum_j \Delta_j e^{-i\boldsymbol{k}\cdot\boldsymbol{a}_j}$ and $d^i(\boldsymbol{k}) = \sum_j d^i_j e^{-i\boldsymbol{k}\cdot\boldsymbol{a}_j}$, the pairing matrix with suppressed mo-

mentum dependence finally takes the form

$$\hat{\Delta}(\boldsymbol{k}) = \begin{pmatrix} 0 & 0 & d^x + \mathrm{i}d^y & \Delta - d^z \\ 0 & 0 & -\Delta - d^z & -d^x + \mathrm{i}d^y \\ d^x + \mathrm{i}d^y & \Delta - d^z & 0 & 0 \\ -\Delta - d^z & -d^x + \mathrm{i}d^y & 0 & 0 \end{pmatrix}. \tag{3.66}$$

With the help of another set of Pauli matrices $\hat{v}_i$ acting on the sublattice subspace, the pairing matrix can be conveniently written as $\hat{\Delta}(\boldsymbol{k}) = (\Delta(\boldsymbol{k})\hat{\sigma}_0 + \boldsymbol{d}(\boldsymbol{k}) \cdot \hat{\boldsymbol{\sigma}})\mathrm{i}\hat{\sigma}_y \otimes \hat{v}_x$.

The self-consistency equations for the pairings are combined in a vector over the three nearest neighbor bonds to yield

$$\Delta = \frac{1}{\sqrt{2}} \left(-J - \frac{K}{4} \right) \left(\langle s_{\boldsymbol{a}_1} \rangle, \langle s_{\boldsymbol{a}_2} \rangle, \langle s_{\boldsymbol{a}_3} \rangle \right), \tag{3.67}$$

$$\boldsymbol{d}^x = \frac{1}{\sqrt{2}} \left(-\frac{K}{4} \langle t^x_{\boldsymbol{a}_1} \rangle, \frac{K}{4} \langle t^x_{\boldsymbol{a}_2} \rangle + \frac{\Gamma}{2} \langle t^z_{\boldsymbol{a}_2} \rangle, \frac{K}{4} \langle t^x_{\boldsymbol{a}_3} \rangle + \frac{\Gamma}{2} \langle t^y_{\boldsymbol{a}_3} \rangle \right), \tag{3.68}$$

$$\boldsymbol{d}^y = \frac{1}{\sqrt{2}} \left(\frac{K}{4} \langle t^y_{\boldsymbol{a}_1} \rangle + \frac{\Gamma}{2} \langle t^z_{\boldsymbol{a}_1} \rangle, -\frac{K}{4} \langle t^y_{\boldsymbol{a}_2} \rangle, \frac{K}{4} \langle t^y_{\boldsymbol{a}_3} \rangle + \frac{\Gamma}{2} \langle t^x_{\boldsymbol{a}_3} \rangle \right), \tag{3.69}$$

$$\boldsymbol{d}^z = \frac{1}{\sqrt{2}} \left(\frac{K}{4} \langle t^z_{\boldsymbol{a}_1} \rangle + \frac{\Gamma}{2} \langle t^y_{\boldsymbol{a}_1} \rangle, \frac{K}{4} \langle t^z_{\boldsymbol{a}_2} \rangle + \frac{\Gamma}{2} \langle t^x_{\boldsymbol{a}_2} \rangle, -\frac{K}{4} \langle t^z_{\boldsymbol{a}_3} \rangle \right). \tag{3.70}$$

In this form the role of the different interactions becomes clear. On the one hand, the Heisenberg interaction drives a spin singlet pairing, which can be enhanced by the Kitaev interaction. On the other hand, the same Kitaev interaction also contributes to spin triplet pairing, with different sign depending on the specific bond. The off-diagonal exchange, finally, supports solely spin triplet pairing and mixes $\boldsymbol{d}$-vector components between bonds.

Analogously to the discussion in prior sections, the self-consistency equations can be solved by invoking the unitary matrix $\hat{\mathcal{U}}$ that encapsulates the Bogoliubov transformation. Terms involved in $\langle s_{\boldsymbol{a}_j} \rangle$ and $\langle t^z_{\boldsymbol{a}_j} \rangle$ are expressed as

$$\langle c_{\boldsymbol{k}\downarrow a} c_{-\boldsymbol{k}\uparrow b} \rangle \mp \langle c_{\boldsymbol{k}\uparrow a} c_{-\boldsymbol{k}\downarrow b} \rangle = \sum_l \left(\mathcal{U}_{\boldsymbol{k}2,l} \mathcal{U}^*_{\boldsymbol{k}7,l} \mp \mathcal{U}_{\boldsymbol{k}1,l} \mathcal{U}^*_{\boldsymbol{k}8,l} \right) (1 - n_F(E_l(\boldsymbol{k}))), \tag{3.71}$$

while the terms involved in $\langle t^x_{\boldsymbol{a}_j} \rangle$ and $\langle t^y_{\boldsymbol{a}_j} \rangle$ can be calculated from

$$\langle c_{\boldsymbol{k}\downarrow a} c_{-\boldsymbol{k}\downarrow b} \rangle \mp \langle c_{\boldsymbol{k}\uparrow a} c_{-\boldsymbol{k}\uparrow b} \rangle = \sum_l \left(\mathcal{U}_{\boldsymbol{k}2,l} \mathcal{U}^*_{\boldsymbol{k}8,l} \mp \mathcal{U}_{\boldsymbol{k}1,l} \mathcal{U}^*_{\boldsymbol{k}7,l} \right) (1 - n_F(E_l(\boldsymbol{k}))). \tag{3.72}$$

Considering spin singlet and triplet pairing, there are in total 12 order parameters. For the analysis in Paper II we only focus on spin triplet pairing,

as the spin singlet pairing is equivalent to the case of superconductivity in graphene. We group the nine spin triplet order parameters in a matrix,

$$
\boldsymbol{d} = \begin{pmatrix} d_1^x & d_2^x & d_3^x \\ d_1^y & d_2^y & d_3^y \\ d_1^z & d_2^z & d_3^z \end{pmatrix},
\tag{3.73}
$$

where the rows correspond to the x, y, z components of the $\boldsymbol{d}$-vector and the columns to the three nearest neighbor bonds $\boldsymbol{a}_1, \boldsymbol{a}_2, \boldsymbol{a}_3$

Because of the simple orbital structure it is possible to find an expression for the conversion to the band basis mentioned in Sec. 3.2 in the case of pure nearest neighbor hopping, something that we use in Paper II to visualize the intraband order parameter. The necessary unitary transformation that diagonalizes the normal state Hamiltonian $\hat{h}_0(\boldsymbol{k})$ is given by

$$
\begin{pmatrix} c_{\boldsymbol{k}\sigma a} \\ c_{\boldsymbol{k}\sigma b} \end{pmatrix} = \frac{1}{\sqrt{2}} \begin{pmatrix} 1 & 1 \\ e^{-i\phi_{\boldsymbol{k}}} & -e^{-i\phi_{\boldsymbol{k}}} \end{pmatrix} \begin{pmatrix} b_{\boldsymbol{k}\sigma 1} \\ b_{\boldsymbol{k}\sigma 2} \end{pmatrix}.
\tag{3.74}
$$

Here, $b_{\boldsymbol{k}\sigma l}$ annihilates an electron in band l, while $\phi_{\boldsymbol{k}} = \arg(\sum_j e^{i\boldsymbol{k}\cdot\boldsymbol{a}_j})$. Introducing the shorthand notation $\varepsilon_{\boldsymbol{k}} = -t|\sum_j e^{i\boldsymbol{k}\cdot\boldsymbol{a}_j}|$, the kinetic part of the Hamiltonian in band space takes the diagonal form

$$
H_{\mathrm{k}} = \sum_{\boldsymbol{k},\sigma} \left((\varepsilon_{\boldsymbol{k}} + \mu) b_{\boldsymbol{k}\sigma 1}^\dagger b_{\boldsymbol{k}\sigma 1} + (-\varepsilon_{\boldsymbol{k}} + \mu) b_{\boldsymbol{k}\sigma 2}^\dagger b_{\boldsymbol{k}\sigma 2} \right).
\tag{3.75}
$$

Using the same transformation, the mean-field pairing Hamiltonian H_Δ can be transformed into the band basis, too. For the spin singlet order parameter this has been worked out before [90]. Therefore I present here only the transformation of the spin triplet pairing terms. Starting from the product of annihilation operators

$$
\begin{aligned}
& c_{\boldsymbol{k},\sigma,a}^\dagger c_{-\boldsymbol{k},\bar{\sigma},b}^\dagger e^{-i\boldsymbol{k}\cdot\boldsymbol{a}_j} \\
&= \frac{1}{2} \sum_{b_1,b_2} b_{\boldsymbol{k},\sigma,b_1}^\dagger b_{-\boldsymbol{k},\bar{\sigma},b_2}^\dagger e^{-i\boldsymbol{k}\cdot\boldsymbol{a}_j} e^{i\phi_{\boldsymbol{k}}} (\tau^z - i\tau^y)_{b_1,b_2} \\
&= \frac{1}{2} \sum_{b_1,b_2} \frac{1}{2} (b_{\boldsymbol{k},\sigma,b_1}^\dagger b_{-\boldsymbol{k},\bar{\sigma},b_2}^\dagger - b_{-\boldsymbol{k},\bar{\sigma},b_2}^\dagger b_{\boldsymbol{k},\sigma,b_1}^\dagger) e^{-i\boldsymbol{k}\cdot\boldsymbol{a}_j} e^{i\phi_{\boldsymbol{k}}} (\tau^z - i\tau^y)_{b_1,b_2} \\
&= \frac{1}{2} \sum_{b_1,b_2} b_{\boldsymbol{k},\sigma,b_1}^\dagger b_{-\boldsymbol{k},\bar{\sigma},b_2}^\dagger \frac{1}{2} (e^{-i\boldsymbol{k}\cdot\boldsymbol{a}_j} e^{i\phi_{\boldsymbol{k}}} + (-1)^{\delta_{b_1,b_2}} e^{i\boldsymbol{k}\cdot\boldsymbol{a}_j} e^{-i\phi_{\boldsymbol{k}}}) (\tau^z - i\tau^y)_{b_1,b_2} \\
&= \frac{1}{2} \sum_{b_1,b_2} b_{\boldsymbol{k},\sigma,b_1}^\dagger b_{-\boldsymbol{k},\bar{\sigma},b_2}^\dagger (-\sin(\boldsymbol{k}\cdot\boldsymbol{a}_j - \phi_{\boldsymbol{k}}) i\tau^z - \cos(\boldsymbol{k}\cdot\boldsymbol{a}_j - \phi_{\boldsymbol{k}}) i\tau^y)_{b_1,b_2},
\end{aligned}
\tag{3.76}
$$

where the matrices τ^γ act on band space and the indices b_i run over the two bands $b_i = 1, 2$. We can introduce the intra- and interband spin triplet order

52

parameters

$$d_{\text{intra}}^{\alpha}(\boldsymbol{k}) = -\mathrm{i} \sum_j d_j^{\alpha} \sin(\boldsymbol{k} \cdot \boldsymbol{a}_j - \phi_{\boldsymbol{k}}) \tag{3.77}$$

$$d_{\text{inter}}^{\alpha}(\boldsymbol{k}) = -\sum_j d_j^{\alpha} \cos(\boldsymbol{k} \cdot \boldsymbol{a}_j - \phi_{\boldsymbol{k}}) \tag{3.78}$$

and rewrite the spin triplet pairing as

$$\left(\sum_j \boldsymbol{d}_j \cdot \hat{\boldsymbol{\sigma}} \right) \mathrm{i}\hat{\sigma}_y \otimes \hat{v}_x = (\boldsymbol{d}_{intra} \cdot \hat{\boldsymbol{\sigma}}) \mathrm{i}\hat{\sigma}_y \otimes \tau_z + (\boldsymbol{d}_{inter} \cdot \hat{\boldsymbol{\sigma}}) \mathrm{i}\hat{\sigma}_y \otimes \mathrm{i}\tau_y. \tag{3.79}$$

As expected from the general discussion in Sec. 3.2, an interband pairing is naturally generated upon the transformation, similarly to the spin singlet case [90]. Notably, the sin and cos terms are exchanged between the spin singlet and triplet case, which preserves the even- and oddness properties.

The extended Kitaev-Heisenberg interaction thus allows spin triplet pairing, where the off-diagonal exchange, in particular, leads to a mixing of $\boldsymbol{d}$-vector components. The resulting order parameters transformed to the band basis split into intra- and interband pairing, as expected from the multiorbital structure.

3.5 Combining interaction and lattice: Spin triplet pairing on the hyperhoneycomb lattice

For Paper V we combine aspects of Sections 3.3 and 3.4 to study the spin triplet superconductivity arising from extended Kitaev-Heisenberg interactions on the hyperhoneycomb lattice. This extends the degrees of freedom to four sublattice sites times spin. Because we focus on the hyperhoneycomb lattice only, we use the four lattice sites in the unit cell, introduced in Sec. 2.2, as the basis states and move away from the block form of the Hamiltonian derived in Sec. 3.3.

For the doped carriers away from half-filling, we again include at first only nearest neighbor hopping with a constant hopping amplitude t and a chemical potential μ,

$$H_k = -t \sum_{\langle i,j \rangle, \sigma, \langle o,o' \rangle} \left(c_{j\sigma o}^{\dagger} c_{i\sigma o'} + h.c. \right) + \mu \sum_{i,\sigma,o} \left(c_{i\sigma o}^{\dagger} c_{i\sigma o} \right), \tag{3.80}$$

where $o = a, b, c, d$. The system is periodic in all three directions, such that a Fourier transform can be performed,

$$H_k(\boldsymbol{k}) = -t \sum_{\boldsymbol{k} j \sigma \langle o,o' \rangle} \mathrm{e}^{\mathrm{i}\boldsymbol{k} \cdot \boldsymbol{a}_j} \left(c_{\boldsymbol{k}\sigma o}^{\dagger} c_{\boldsymbol{k}\sigma o'} + h.c. \right) + \mu \sum_{\boldsymbol{k},\sigma,o} \left(c_{\boldsymbol{k}\sigma o}^{\dagger} c_{\boldsymbol{k}\sigma o} \right). \tag{3.81}$$

In the basis $\Psi = (c_{\boldsymbol{k}\sigma a}, c_{\boldsymbol{k}\sigma b}, c_{\boldsymbol{k}\sigma c}, c_{\boldsymbol{k}\sigma d})^T$ this takes the matrix form

$$H_k = \begin{pmatrix} \mu & T^1 & 0 & T^{2,3} \\ T^{1*} & \mu & T^{5,6*} & 0 \\ 0 & T^{5,6} & \mu & T^4 \\ T^{2,3*} & 0 & T^{4*} & \mu \end{pmatrix}, \tag{3.82}$$

with the shorthand notation $T^j = -t \sum_j e^{-i\boldsymbol{k}\cdot\boldsymbol{a}_j}$. Apart from the nearest neighbor hopping, there are further, second nearest neighbor spin-orbit coupled hopping terms. Here we only consider the largest of these [96],

$$H_{SO} = \sum_{\langle\langle i,j \rangle\rangle} c_{i\sigma}^\dagger \left(i t_{KM} \frac{\hat{\boldsymbol{r}}_{ik} \times \hat{\boldsymbol{r}}_{kj}}{|\hat{\boldsymbol{r}}_{ik} \times \hat{\boldsymbol{r}}_{kj}|} \cdot \hat{\boldsymbol{\sigma}} \right)_{\sigma\bar{\sigma}} c_{j\bar{\sigma}}, \tag{3.83}$$

where $\hat{\boldsymbol{r}}_{ik}$ and $\hat{\boldsymbol{r}}_{kj}$ are the normalized nearest neighbor vectors making up the second nearest neighbor vector $\boldsymbol{b}_{ij}$. This hopping is another generalized Kane-Mele type hopping, where now the active spin component is the one that is perpendicular to the second nearest neighbor bond [96]. Due to the 3D nature of the lattice there are two different cases. The active component is either the $(1,1,1)$ component for the six second nearest neighbor bonds involving $\boldsymbol{a}_{2,3}$, or the $(-1,1,1)$ component for the remaining six second nearest neighbor bonds involving $\boldsymbol{a}_{5,6}$.

For the interaction, we are again considering the extended Kitaev-Heisenberg model, so the interacting Hamiltonian looks very similar to that in Sec. 3.4

$$H_{JK\Gamma} = \sum_{\langle i,j \rangle} \left\{ J \left(\boldsymbol{S}_i \cdot \boldsymbol{S}_j - \frac{1}{4} n_i n_j \right) + K S_i^{\gamma(i,j)} S_j^{\gamma(i,j)} \right.$$
$$\left. + \varepsilon_j \Gamma \left(S_i^{\alpha(i,j)} S_j^{\beta(i,j)} + S_i^{\beta(i,j)} S_j^{\alpha(i,j)} \right) \right\}, \tag{3.84}$$

except that there are now six nearest neighbor bonds $\langle i,j \rangle$ and that the sign of Γ changes on bonds $\boldsymbol{a}_5$ and $\boldsymbol{a}_6$, such that $\varepsilon_j = 1$ for $j \in \{1,\dots 4\}$ and $\varepsilon_j = -1$ for $j \in \{5,6\}$. Also, $\gamma(i,j) = \{x,y,z,x,z,y\}$, as explained in Sec. 2.1. Nevertheless, the interactions can be rewritten in terms of nearest neighbor spin singlet and triplet operators as defined in Eq. (3.53). We can then write the pairing matrix

$$H_\Delta = \boldsymbol{\psi}_k^\dagger \begin{pmatrix} 0 & \hat{\Delta}^1(-\boldsymbol{k}) & 0 & \hat{\Delta}^{2,3}(-\boldsymbol{k}) \\ \hat{\Delta}^1(\boldsymbol{k}) & 0 & \hat{\Delta}^{5,6}(\boldsymbol{k}) & 0 \\ 0 & \hat{\Delta}^{5,6}(-\boldsymbol{k}) & 0 & \hat{\Delta}^4(-\boldsymbol{k}) \\ \hat{\Delta}^{2,3}(\boldsymbol{k}) & 0 & \hat{\Delta}^4(\boldsymbol{k}) & 0 \end{pmatrix} \boldsymbol{\psi}_{-k}^* \tag{3.85}$$

with $\boldsymbol{\psi}_k^\dagger = \left(c_{\boldsymbol{k}\uparrow 1}^\dagger, c_{\boldsymbol{k}\downarrow 1}^\dagger, c_{\boldsymbol{k}\uparrow 2}^\dagger, \dots, c_{\boldsymbol{k}\downarrow 4}^\dagger \right)$ and the pairing block matrices $\hat{\Delta}^j(\boldsymbol{k}) = \sum_j (\Delta_j \hat{\sigma}_0 + \boldsymbol{d}_j \cdot \hat{\boldsymbol{\sigma}}) i\hat{\sigma}_y e^{-i\boldsymbol{k}\cdot\boldsymbol{a}_j}$.

The bond order parameters can be grouped into the horizontal bonds $j = 1, 4$

$$\Delta_j = \frac{1}{\sqrt{2}} \left(-J - \frac{K}{4} \right) \langle s_{\boldsymbol{a}_j} \rangle, \qquad d_j^x = \frac{1}{\sqrt{2}} \left(-\frac{K}{4} \right) \langle t_{\boldsymbol{a}_j}^x \rangle \tag{3.86}$$

$$d_j^x = \frac{1}{\sqrt{2}} \left(\frac{K}{4} \langle t_{\boldsymbol{a}_j}^y \rangle + \frac{\Gamma}{2} \langle t_{\boldsymbol{a}_j}^z \rangle \right), \qquad d_j^x = \frac{1}{\sqrt{2}} \left(\frac{K}{4} \langle t_{\boldsymbol{a}_1}^z \rangle + \frac{\Gamma}{2} \langle t_{\boldsymbol{a}_1}^y \rangle \right), \tag{3.87}$$

and the zigzag bonds

$$(\Delta_2, \Delta_3) = \frac{1}{\sqrt{2}} \left(-J - \frac{K}{4} \right) \left(\langle s_{\boldsymbol{a}_2} \rangle, \langle s_{\boldsymbol{a}_3} \rangle \right), \tag{3.88}$$

$$(d_2^x, d_3^x) = \frac{1}{\sqrt{2}} \left(\frac{K}{4} \langle t_{\boldsymbol{a}_2}^x \rangle + \frac{\Gamma}{2} \langle t_{\boldsymbol{a}_2}^z \rangle, \frac{K}{4} \langle t_{\boldsymbol{a}_3}^x \rangle + \frac{\Gamma}{2} \langle t_{\boldsymbol{a}_3}^y \rangle \right), \tag{3.89}$$

$$(d_2^y, d_3^y) = \frac{1}{\sqrt{2}} \left(-\frac{K}{4} \langle t_{\boldsymbol{a}_2}^y \rangle, \frac{K}{4} \langle t_{\boldsymbol{a}_3}^y \rangle + \frac{\Gamma}{2} \langle t_{\boldsymbol{a}_3}^x \rangle \right), \tag{3.90}$$

$$(d_2^z, d_3^z) = \frac{1}{\sqrt{2}} \left(\frac{K}{4} \langle t_{\boldsymbol{a}_2}^z \rangle + \frac{\Gamma}{2} \langle t_{\boldsymbol{a}_2}^x \rangle, -\frac{K}{4} \langle t_{\boldsymbol{a}_3}^z \rangle \right), \tag{3.91}$$

and

$$(\Delta_5, \Delta_6) = \frac{1}{\sqrt{2}} \left(-J - \frac{K}{4} \right) \left(\langle s_{\boldsymbol{a}_5} \rangle, \langle s_{\boldsymbol{a}_6} \rangle \right), \tag{3.92}$$

$$(d_5^x, d_6^x) = \frac{1}{\sqrt{2}} \left(\frac{K}{4} \langle t_{\boldsymbol{a}_5}^x \rangle - \frac{\Gamma}{2} \langle t_{\boldsymbol{a}_5}^y \rangle, \frac{K}{4} \langle t_{\boldsymbol{a}_6}^x \rangle - \frac{\Gamma}{2} \langle t_{\boldsymbol{a}_6}^z \rangle \right), \tag{3.93}$$

$$(d_5^y, d_6^y) = \frac{1}{\sqrt{2}} \left(\frac{K}{4} \langle t_{\boldsymbol{a}_5}^y \rangle - \frac{\Gamma}{2} \langle t_{\boldsymbol{a}_5}^x \rangle, -\frac{K}{4} \langle t_{\boldsymbol{a}_6}^y \rangle \right), \tag{3.94}$$

$$(d_5^z, d_6^z) = \frac{1}{\sqrt{2}} \left(-\frac{K}{4} \langle t_{\boldsymbol{a}_5}^z \rangle, \frac{K}{4} \langle t_{\boldsymbol{a}_6}^z \rangle - \frac{\Gamma}{2} \langle t_{\boldsymbol{a}_5}^x \rangle \right). \tag{3.95}$$

With the help of the Bogoliubov transformation matrix $\hat{\mathcal{U}}$ it is once more possible to calculate the expectation values self-consistently by using the expression

$$\langle c_{\boldsymbol{k}\sigma o} c_{-\boldsymbol{k}\bar{\sigma}\bar{o}} \rangle = \sum_l \mathcal{U}_{\boldsymbol{k}2(o-1)+\sigma,l} \mathcal{U}^*_{\boldsymbol{k}2(o-1)+\sigma,l} (1 - n_F (E_l(\boldsymbol{k}))), \tag{3.96}$$

where $o = 1, \dots, 4$ and, on the right hand side, $\sigma = 1, 2$ for $\uparrow, \downarrow$.

The derivation thus follows straightforwardly from the case of the extended Kitaev-Heisenberg interaction on the honeycomb lattice, but now involves a larger number of order parameters.

4. Symmetry classification

The self-consistency equations derived in the previous chapter allow to calculate the superconducting order parameters. The next step is a characterization of the obtained order in terms of its symmetries. In this chapter I compile at first some of the mathematical concepts of group theory that are important for the symmetry classification of superconductors. This is intended to only be an excerpt of the full mathematical theory and no proofs are presented. A more detailed introduction to group theory can be found in Refs. [97, 98]. Thereafter, in Sec. 4.2, I discuss some of the symmetries relevant for classifying superconducting order parameters. Finally, I present how we apply the symmetry classification to the order parameters obtained in Papers I-II, and V.

4.1 Background: Group theory

4.1.1 Groups, Subgroups, Classes

A symmetry operation is a transformation that returns the original state of a specific system. The system is then said to be invariant under the operation. Mirror symmetries, rotations, or translations are examples of such operations. Some objects can have several of such symmetries, such as the triangle depicted in Figure 4.1. It has the following symmetries: A rotation by $\frac{2\pi}{3}$ in either direction around a perpendicular axis, and rotations by π around the axes connecting the end points of the triangle with the centers of the opposite sides. Since each individual operation returns the initial object, it becomes clear that symmetries can be combined, i.e. applied after each other. The result will be another symmetry operation, since the sequential application also returns the system in its original state. This motivates the use of groups to describe symmetry operations. A group is defined as follows.

Definition 1. A *group* is a set G of objects together with a multiplication, which fulfills the following axioms:
   1. The group is closed under the application of the multiplication:

$$\forall g_1, g_2 \in G : g_1 g_2 \in G \qquad (4.1)$$

   2. The multiplication is associative:

$$\forall g_1, g_2, g_3 \in G : g_1(g_2 g_3) = (g_1 g_2) g_3 \qquad (4.2)$$
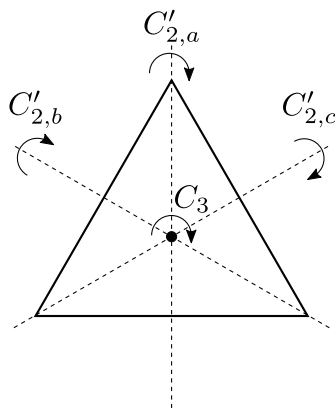
Figure 4.1. An illustration of the symmetries of an equilateral triangle. There is a three-fold rotation C_3 around the principal axis perpendicular to the triangle. The three two-fold rotations C_2' are around axes perpendicular to the principal axis. The symmetry elements form the group D_3.

3. The identity element E is part of the group:

$$\exists E \in G : \forall g \in G, Eg = gE = g \tag{4.3}$$

4. Every group element has an inverse that is also part of the group:

$$\forall g \in G, \exists g^{-1} \in G : gg^{-1} = g^{-1}g = E \tag{4.4}$$

In a finite group, the number of elements in the group is called the *order* of the group and denoted by $|G|$.

The definition of a group is general and does not only apply for symmetry operations, but it is easy to check that the symmetry operations of an object fulfill all the axioms. It is noteworthy that the definition of a group does not at all specify what the group objects act on. This will be of importance later on, when mapping different groups to each other is discussed.

The definition has several consequences and extensions. For example, the product of two operations $g_1 g_2$ does not need to be commutative. If $g_1 g_2 = g_2 g_1$ for any two group elements, the group is called *abelian*. Furthermore, the identity element and the inverse of an element are unique. Finally, the inverse of the inverse returns the original object, $(g^{-1})^{-1} = g$, as one might expect.

The group of the equilateral triangle contains the following elements: $D_3 = \{E, C_3, C_3^2, C_{2,a}', C_{2,b}', C_{2,c}'\}$, as pictured in Fig. 4.1. Here the notation C_n for an n-fold rotation is used. The axis with the highest-fold rotation is called the principal axis. The symbol C' specifies a rotation around an axis perpendicular to this principal axis. It is clear that the two-fold rotations are their own inverses, whereas the two three-fold rotations are each others inverse.

Some of the elements of the group can form a group by themselves, this is called a subgroup.

Definition 2. A *subgroup H* of *G* is a subset of *G*, that together with the multiplication of *G* forms a group in itself.

As an implication of this the identity *E* is part of every subgroup. In fact, the identity element by itself forms a so-called trivial subgroup. The group *G* itself is also a trivial subgroup of itself. All other subgroups are called proper subgroups. For the D_3 group, the set $C_3 = \{E, C_3, C_3^2\}$ makes up a proper subgroup.

Some group elements naturally resemble each other, like the $C'_{2,i}$ rotations of the example. Formally, this resemblance is captured by the equivalence relation conjugacy.

Definition 3. Two group elements g_1, g_2 are *conjugate* to each other if for

$$g_1, g_2 \in G, \exists h \in G : g_1 = h g_2 h^{-1}. \tag{4.5}$$

The set of all elements that are conjugate to each other is called a *(conjugacy) class*.

One can prove that all classes are disjoint and that every group element is in some class of the group. The classes of the example group D_3 are

$$\{E\}, \{C_3, C_3^2\}, \{C'_{2,a}, C'_{2,b} C'_{2,c}\}. \tag{4.6}$$

For example, a forward rotation by $\frac{2\pi}{3}$ is equal to a backward rotation around that angle, if it is preceded by a π rotation around a perpendicular axis and succeeded by the inverse π rotation: $C_3 = C'_{2,a} C_3^2 (C'_{2,a})^{-1}$.

Since groups are so general, it can be tricky to deal with the multiplication of group elements. An important kind of groups are therefore matrix groups, which allow for convenient algebraic expressions. In particular, $n \times n$ square matrices with non-zero determinants (such that the inverse matrix exists) allow for translation of multiplication, identity, and inverse into the corresponding matrix operations. Some of the most important matrix groups are listed below:

- The general linear group $GL(n, \mathbb{F})$ denotes the group of invertible $n \times n$ matrices with real ($\mathbb{F} = \mathbb{R}$) or complex entries ($\mathbb{F} = \mathbb{C}$).
- The special linear group $SL(n, \mathbb{F})$ is a subgroup of $GL(n, \mathbb{F})$, with the additional requirement that the determinant is always 1.
- The group of orthogonal matrices $O(n, \mathbb{R})$ requires that $\forall \hat{O} \in O, \hat{O}^T \hat{O} = \hat{O} \hat{O}^T = \hat{\mathbb{1}}$
- The special orthogonal group $SO(n, \mathbb{R})$ contains all orthogonal matrices with determinant 1.
- The unitary group $U(n)$ is the group of $n \times n$ matrices with complex entries that fulfills $\forall \hat{U} \in U(n), \hat{U}^\dagger \hat{U} = \hat{U} \hat{U}^\dagger = \hat{\mathbb{1}}$

- The special unitary group $SU(n)$ is the subgroup of the unitary group that contains unitary matrices with determinant 1.

With matrix groups it also becomes clearer what the group elements are applied to, because an $n \times n$ matrix requires some sort of n-dimensional vector space to act on.

4.1.2 Representations

An important concept in dealing with groups are mappings between different groups: $f : G \to G'$ maps an element from from group G to an element of G', i.e. $g' = f(g)$ for $g \in G, g' \in G'$. These mappings can be categorized as injective (one-to-one) and surjective (onto) like any other mapping. Important for mappings between groups is the preservation of the group multiplication:

Definition 4. A mapping $f : G \to G'$ is called a *homomorphism*, if it preserves the group multiplication:

$$\forall g_1, g_2 \in G, f(g_1)f(g_2) = f(g_1 g_2). \tag{4.7}$$

A homomorphism that is bijective (both in- and surjective) is called an *isomorphism*.

The groups G and G' that are connected by an isomorphism are then said to be isomorphic and share their properties, such as classes and subgroups. As a consequence, an abstract group can be mapped to a matrix group, which allows for convenient calculations, instead of dealing with the abstract operations. This mapping is called a representation.

Definition 5. A *representation* $\hat{\rho}$ of a finite group G is a homomorphism from G to the general linear group of matrices: $\hat{\rho} : G \to GL(n, \mathbb{C})$. The dimension of the matrices n is called the *dimension* of the representation.

A specific mapping to some representation is coupled to a choice of vector space that the matrices act on. An example of a homomorphic representation of D_3 is the mapping onto the following 1×1 matrices:

$$
\begin{array}{lll}
E \to (1), & C_3 \to (1), & C_3^2 \to (1), \\
C_{2,a}' \to (-1), & C_{2,b}' \to (-1), & C_{2,c}' \to (-1).
\end{array}
\tag{4.8}
$$

The group multiplication is preserved, but the mapping is not bijective, since several group elements are mapped onto the same matrix. An isomorphic

representation would be

$$
E \to \begin{pmatrix} 1 & 0 \\ 0 & 1 \end{pmatrix}, \qquad C_3 \to \begin{pmatrix} -\frac{1}{2} & -\frac{\sqrt{3}}{2} \\ \frac{\sqrt{3}}{2} & -\frac{1}{2} \end{pmatrix}, \qquad C_3^2 \to \begin{pmatrix} -\frac{1}{2} & \frac{\sqrt{3}}{2} \\ -\frac{\sqrt{3}}{2} & -\frac{1}{2} \end{pmatrix},
$$

$$
C_{2,a}' \to \begin{pmatrix} 1 & 0 \\ 0 & -1 \end{pmatrix}, \quad C_{2,b}' \to \begin{pmatrix} -\frac{1}{2} & -\frac{\sqrt{3}}{2} \\ -\frac{\sqrt{3}}{2} & \frac{1}{2} \end{pmatrix}, \quad C_{2,c}' \to \begin{pmatrix} -\frac{1}{2} & \frac{\sqrt{3}}{2} \\ \frac{\sqrt{3}}{2} & \frac{1}{2} \end{pmatrix}.
$$

$$
\tag{4.9}
$$

It is possible to check that both of these mappings reproduce the same classes discussed earlier. A general result apparent in these examples is that the representation of the identity element is always the $n \times n$ identity matrix.

Having a particular representation $\hat{\rho}$, it is possible to construct a new representation $\hat{\rho}'$, simply by defining $\hat{\rho}'(g) = \hat{A}\hat{\rho}(g)(\hat{A})^{-1}$ with some matrix $\hat{A} \in GL(n, \mathbb{C})$. Obviously, the new representation is in some sense equivalent to the original one.

Definition 6. A representation $\hat{\rho}'$ is *similar* to another representation $\hat{\rho}$, if

$$
\exists \hat{A} \in GL(n, \mathbb{C}) : \hat{\rho}'(g) = \hat{A}\hat{\rho}(g)(\hat{A})^{-1}. \tag{4.10}
$$

This corresponds to expressing the representation in another basis, where $\hat{A}$ is the transformation matrix. Another way of constructing a new representation is taking the direct sum

$$
(\hat{\rho} \oplus \hat{\rho}')(g) = \begin{pmatrix} \hat{\rho}(g) & \hat{0} \\ \hat{0} & \hat{\rho}'(g) \end{pmatrix}. \tag{4.11}
$$

The choice of representations is thus not unique. The notion of irreducible representation (irrep) allows to define the most basic representations.

Definition 7. A representation is called *irreducible*, if it is not similar to a direct product of representations. All other representations are *reducible*.

This definition is not easy to work with, since it is hard to see similarity of representations. A powerful tool in figuring out irreducibility is the character.

Definition 8. The *character* $\chi_\rho(g)$ of a representation $\hat{\rho}$ is given by the trace over the representation

$$
\chi_\rho(g) = \mathrm{Tr}\hat{\rho}(g). \tag{4.12}
$$

Due to the cyclic character of the trace, the character is the same for similar representations. All conjugate group elements also share the same character. It is also clear that the character of the identity operation is equal to the dimension of the irreducible representation. Finally, the character of the inverse of a

Irreducible Representation	E	$2C_3$	$3C_2'$
A_1	1	1	1
A_2	1	1	-1
E	2	-1	0

Table 4.1. *The character table for the group D_3. The first column contains the different irreducible representations. The header lists all conjugacy classes and the number of elements of each class. The table is filled with the characters of the irreducible representations.*

group element is the complex conjugate of the character of the group element for all applications within the scope of this thesis.

With the help of the character, it is possible to define an inner product of two representations.

Definition 9. The *inner product* of two representations $\hat{\rho}$ and $\hat{\rho}'$ is given by

$$\langle \rho | \rho' \rangle = \frac{1}{|G|} \sum_{g \in G} \chi_\rho(g) \chi_{\rho'}(g) *. \tag{4.13}$$

It can be shown that irreducible representations are orthonormal under this inner product. Thus the inner product of an irreducible representation with itself gives one, whereas the inner product of two different irreducible representations gives zero. The inner product can also be used to show that the number of irreducible representations is equal to the number of classes of the group.

For the example of the D_3 group, two representations have been presented in Eqs. (4.8) and (4.9) and their characters can be calculated. Using the inner product, it becomes clear that these representations of the D_3 group presented are, in fact, irreducible representations. Since there are three classes, there must be a third irreducible representation. Using the orthonormality of the irreducible representations, one can construct the missing irreducible representation, which turns out to have character 1 for all group elements. This so-called trivial irreducible representation is actually present for any group.

Even when no representation is constructed, the orthonormality of the irreducible representations allows to establish the characters of the group elements and to construct a so-called character table, which contains the most vital information about a group. Character tables contain the conjugacy classes of the group, the irreducible representations and their characters. The character table for the D_3 group is presented in Table 4.1.

4.1.3 Basis functions

Using a representation of a group, it is possible to consider the symmetry as acting on a particular vector space. For each vector space, there exist basis functions of the different irreducible representations.

Definition 10. The *basis functions* of an (irreducible) representation $\hat{\rho}$ of dimension n are the functions f_i, with $i = 1, \ldots, n$, that are mapped onto a linear combination of themselves under the application of the group elements

$$g(f_i) = \sum_{j=1}^{n} (\rho(g))_{n,j} f_j. \tag{4.14}$$

The coefficients correspond to the matrix elements of the representation. In particular, for a one-dimensional irreducible representation, f is mapped onto itself, multiplied by the character of the representation. It is said that f *transforms according to the (irreducible) representation* $\hat{\rho}$.

The precise form of basis function depends on the vector space chosen, i.e. on the representation used. Important examples are the coordinate functions x, y, z or wave functions in quantum mechanics. But they can be vectors in any other kind of vector space, as well.

An important feature of these basis functions is that they inherit the orthogonality of the irreducible representations under the corresponding inner product of the vector space. This can be used to project out the different basis functions from an arbitrary function with the help of the projection operators.

Definition 11. The *projection operator* of an irreducible representation $\hat{\rho}$ of dimension n of a group G is defined as

$$P_\rho = \frac{n}{|G|} \sum_{g \in G} \chi_\rho^*(g) g. \tag{4.15}$$

Importantly, these projection operators only involve the character and the group elements. This way it is possible to construct the projection operator without having to find an irreducible representation first. The basis functions of all the different irreducible representations of a group in a given vector space can then be projected out by applying the corresponding projection operators on an arbitrary vector f. The resulting vector $P_\rho f$ will then transform according to the irreducible representation $\hat{\rho}$. To obtain a set of orthonormal basis vectors of an n-dimensional irreducible representation, this procedure has to be repeated and the resulting vectors need to be orthonormalized by e.g. a standard Gram-Schmidt algorithm.

As an example, the basis functions for the D_3 group in the coordinate vector space can be constructed. The first step is to obtain the projection operators.

The effect of the group elements of the group D_3 on the coordinate functions can be figured out by placing the C_3 rotation axis along the z-axis of the coordinate system. The characters of the different irreducible representations is given in the character table in Tab. 4.1. Applying the projection operator P_{A_2} to the function z maps it onto itself. It remains invariant under the C_3 rotations, but changes sign under the application of any of the C'_2 operations, which is compensated by the character. This means the function z transforms according to the irreducible representation A_2 which was given in Eq. (4.8) and forms a basis function of this 1D irreducible representation. The functions x and y are mixed by the application of the group elements, with the exact action given by the representation presented in Eq. (4.9). x and y thus form two basis functions of the two-dimensional E irreducible representation.

4.2 Physical symmetries relevant for superconductors

After this general introduction to symmetry groups, I introduce the non-spatial and spatial symmetries important for classifying superconducting order parameters and determining the topological properties. Given a BdG Hamiltonian of the general form

$$H = \frac{1}{2}\mathbf{\Psi}^\dagger \hat{h}\mathbf{\Psi}, \qquad (4.16)$$

where $\mathbf{\Psi}$ are the Nambu spinors containing all essential degrees of freedom (spin, orbital, lattice site), in general symmetries act by transforming the Nambu spinor

$$g\mathbf{\Psi} = \mathbf{\Psi}' = \hat{U}_g\mathbf{\Psi} \qquad (4.17)$$

through a matrix representation of the symmetry $\hat{U}_g$. This implies that the system described by the Hamiltonian is invariant under the symmetry g, if

$$\hat{U}_g^\dagger \hat{h}\hat{U}_g = \hat{h}. \qquad (4.18)$$

Furthermore, $\hat{U}_g$ needs to preserve the norm of expectation values, which is the case if it is a unitary matrix. However, the norm can also be preserved by an anti-unitary symmetry, which can be represented by a combination of a unitary matrix and complex conjugation K.

4.2.1 Time-reversal symmetry (TRS)

Time-reversal symmetry $\mathcal{T}$ is an example of an anti-unitary symmetry. Expressing it as $\mathcal{T} = \hat{U}_T K$, a Hamiltonian is time-reversal symmetric, if [12]

$$\hat{U}_T^\dagger \hat{h}^*(\mathbf{k})\hat{U}_T = \hat{h}(-\mathbf{k}), \qquad (4.19)$$

which has two implications. If the system is time-reversal invariant, a state at $\boldsymbol{k}$ is accompanied by a state at $-\boldsymbol{k}$ with the same energy. If inversion symmetry is also present, this will lead to a double degeneracy of eigenstates at $\boldsymbol{k}$. Moreover, the transformation of the pairing matrix $\hat{\Delta}$ implies that a time-reversal invariant pairing must obey $\Delta_{\boldsymbol{k}}^* = \Delta_{-\boldsymbol{k}}$ and $\boldsymbol{d}_{\boldsymbol{k}}^* = \boldsymbol{d}_{-\boldsymbol{k}}$. This means that a system that is both inversion symmetric and time-reversal symmetric, must have a real pairing up to a phase that can be gauged away. Such a pairing will always be unitary. Only when the superconducting pairing also breaks the time-reversal symmetry can non-unitary pairing be present.

Time-reversal symmetry corresponds to inverting the arrow of time. Applying time-reversal twice should thus return the initial state (up to a phase), such that [99]

$$e^{i\phi} \overset{!}{=} \mathcal{T}^2 = \hat{U}_T \hat{U}_T^*, \tag{4.20}$$

implying $\hat{U}_T = e^{i\phi} \left(\hat{U}_T\right)^T$ and $\left(\hat{U}_T\right)^T = \hat{U}_T e^{i\phi}$. Combining these two yields $\hat{U}_T = e^{2i\phi} \hat{U}_T$. The time-reversal symmetry operator $\mathcal{T}$ thus squares to either plus or minus one, $\mathcal{T}^2 = \pm 1$. The time-reversal operator for spinful systems, usually represented by $\mathcal{T} = i\hat{\sigma}_y K$, is an example that squares to -1, while the time-reversal for spinless systems $\mathcal{T} = K$ squares to $+1$.

4.2.2 Particle-hole symmetry (PHS)

Another anti-unitary symmetry is particle-hole or charge conjugacy symmetry $\mathcal{C} = \hat{U}_C K$, which relates the creation and annihilation operators through [12]

$$\boldsymbol{\Psi}' = \hat{U}_C^* \boldsymbol{\Psi}^\dagger. \tag{4.21}$$

A system is said to be particle-hole symmetric, if the Hamiltonian obeys

$$\hat{U}_C^\dagger \hat{h}(\boldsymbol{k})^* \hat{U}_C = -\hat{h}(-\boldsymbol{k}). \tag{4.22}$$

This implies that the Hamiltonian is traceless $\text{Tr}\hat{h} = 0$ and that the spectrum is symmetric around zero. Similarly to time-reversal, the particle-hole operator squares to plus or minus one: $\mathcal{C}^2 = \pm 1$.

The introduction of the Nambu spinor in Eq. (3.17) is coupled to an intrinsic particle-hole symmetry $\mathcal{C}$ of the superconducting state. The particle-hole symmetry can be implemented through

$$\mathcal{C} = \hat{t}_x K, \tag{4.23}$$

where $\hat{t}_i$ are the Pauli matrices acting on the particle-hole space. $\mathcal{C}$ thus exchanges creation and annihilation operators and connects the interdependent degrees of freedom. A quick check reveals that this implementation of PHS fulfills $\mathcal{C}^2 = 1$

4.2.3 Chiral symmetry

The combination of TRS and PHS $\mathcal{S} = \mathcal{T}\mathcal{C}$ is called chiral or sublattice symmetry and is represented by a unitary matrix [12]

$$\hat{U}_S = \hat{U}_T^* \hat{U}_C^*. \tag{4.24}$$

This implies that the chiral symmetry always squares to plus one $\mathcal{S}^2 = +1$. A Hamiltonian that is chiral symmetric obeys

$$\hat{U}_S^\dagger \hat{h}(\boldsymbol{k}) \hat{U}_S = -\hat{h}(\boldsymbol{k}) \tag{4.25}$$

and can be written in the block off-diagonal form

$$\hat{h} = \begin{pmatrix} 0 & \hat{D} \\ \hat{D}^\dagger & 0 \end{pmatrix}, \tag{4.26}$$

in the basis where the chiral operator $\hat{U}_S$ is diagonal. A Hamiltonian is automatically symmetric under chiral symmetry, if it is both time-reversal and particle-hole symmetric. However, a Hamiltonian can also be chiral symmetric, if TRS and PHS are no symmetries of the Hamiltonian.

4.2.4 Point groups

The point group contains the set of all spatial symmetry operations of a lattice that leave one specific point unchanged. That means it includes all spatial symmetries of the lattice, excluding translations. Any point group element acts in two ways. Firstly, it transforms the $\boldsymbol{k}$ dependence of the Hamiltonian according to the representation $\hat{\rho}(g)$ of the group element g, and secondly it can act on the orbital structure of the Hamiltonian through a unitary matrix $\hat{U}_g$. A Hamiltonian that is invariant under a certain point group symmetry thus obeys

$$\hat{h}(\boldsymbol{k}) = \hat{U}_g^\dagger \hat{h}(\hat{\rho}(g)\boldsymbol{k}) \hat{U}_g. \tag{4.27}$$

For a particular momentum $\boldsymbol{k}_0$ invariant under g, the Hamiltonian thus commutes with the symmetry operator

$$\left[\hat{h}(\boldsymbol{k}_0), \hat{U}_g\right] = 0, \tag{4.28}$$

which means that the Hamiltonian can be block diagonalized in the eigenspaces of the symmetry operator.

When the studied Hamiltonian is characterized by strong spin-orbit coupling, the operations of the point group do not only act on the lattice degrees of freedom, but must be combined with a rotation of the spin degrees of freedom [4]. This has a particular consequence for the pairing matrix. Whereas

the spin singlet is invariant under such spin transformations, the $\boldsymbol{d}$-vector will transform as

$$g\boldsymbol{d}(\boldsymbol{k}) = \hat{\mathcal{U}}_g \boldsymbol{d}(\hat{\rho}(g)\boldsymbol{k}), \qquad (4.29)$$

where $\hat{\mathcal{U}}_g(\boldsymbol{k})$ is the representation of the group element in spin space. The symmetries of the point group are of importance when calculating the superconducting order from the self-consistency equation Eq. (3.25), which is essentially an eigenvalue equation. Such an eigenvalue equation exhibits the property that its eigenfunctions form basis functions of the irreducible representations of the symmetry group of the equation. For the case of the order parameter, this means that at T_C any superconducting order will transform according to certain irreducible representations of the point group of the lattice [4].

It is hence useful to construct the basis functions of the irreducible representations $\hat{\Delta}_\rho$ in the vector space of choice. At the critical temperature T_c, any solution of the gap equation Eq. (3.22) will then be a linear combination of basis functions of a particular irreducible representation:

$$\hat{\Delta} = \sum_i^n \eta_i \hat{\Delta}_\rho, \qquad (4.30)$$

where n is the dimension of the irreducible representation. For one-dimensional irreducible representations, there is thus only one superconducting state possible. In higher-dimensional irreducible representations, there can be different linear combinations of the basis functions. A mixing of irreducible representations can only occur, if the superconducting state breaks several symmetries in a series of transitions or if two irreducible representations share an accidental degeneracy.

A main focus of Papers I-II and V contained in this thesis is to find basis functions for the relevant point groups to identify the symmetry of the superconducting order. For that purpose I first construct a representation of the point group elements suitable for the chosen vector space by considering the action of the group elements on the pairing matrix $\hat{\Delta}$, by transforming the spin singlet and triplet order parameters Δ and $\boldsymbol{d}$, respectively. Then I use the character table to build the projection operator $\hat{P}_\rho$ for all irreducible representations of the point group as defined in Eq. (4.15). Next, there are two ways to proceed. In some cases I subsequently apply the projectors of all irreducible operations P_ρ on a general function $\boldsymbol{\Delta} = (\Delta_1, \ldots, \Delta_n)$ and extract the basis functions by requiring

$$\hat{P}_\rho \boldsymbol{\Delta}_\rho \overset{!}{=} \boldsymbol{\Delta}_\rho. \qquad (4.31)$$

Another approach builds on identifying Eq. (4.31) as an eigenvalue equation. This way calculating the eigenfunctions of the projection operators and identifying those with eigenvalue one also allows to retrieve the basis functions. For

a given order parameter, it is then useful to calculate the overlap with these basis functions

$$\frac{\mathbf{\Delta} \cdot \mathbf{\Delta}_\rho}{|\mathbf{\Delta}|} \tag{4.32}$$

to identify the symmetry. In the following sections I present the constructions in more detail and discuss how the basis functions shape the phase diagrams of superconductivity in the Kitaev materials.

4.3 Approximate six-fold symmetry on the large harmonic honeycomb lattices

In Paper I we first study the superconducting spin singlet pairing on the large members of the harmonic honeycomb series. Even though the point group of the harmonic honeycomb lattices is D_{2h}, at least the larger members of the series can be analyzed by using the point group of the hexagonal lattice D_{6h} instead. Because the irreducible representations of D_{6h} are not irreducible representations of the proper symmetry D_{2h}, the superconducting order will in general mix basis functions of different irreducible representations. At large enough spacing between twists, however, the additional six-fold symmetry will be almost recovered such that the mixing should be small. Another benefit is that the classification in terms of D_{6h} is well known from the case of superconducting graphene [90].

As we only take into account spin singlet pairing, we can further simplify the calculation by considering the group C_{6v} instead. It contains all the information apart from the even- or oddness under inversion. The character table of C_{6v} is given in Table 4.2. The order parameters of the three nearest neighbor bonds around an a site in the harmonic honeycomb lattice can be grouped into the vector $\mathbf{\Delta} = (\Delta_1, \Delta_2, \Delta_3)$. Choosing this as the vector space, a representation of C_{6v} is given by

$$\begin{aligned}
E &= \mathbb{1}, \quad C_6 = (1 \rightarrow 3, 2 \rightarrow 1, 3 \rightarrow 2), \quad C_3 = (1 \rightarrow 2, 2 \rightarrow 3, 3 \rightarrow 1), \\
C_2 &= \mathbb{1}, \quad \sigma_v = (1 \rightarrow 1, 2 \rightarrow 3, 3 \rightarrow 2), \quad \sigma_d = (1 \rightarrow 1, 2 \rightarrow 3, 3 \rightarrow 2),
\end{aligned} \tag{4.33}$$

where $\mathbb{1}$ is the identity and $i \rightarrow j$ means that Δ_i is mapped onto Δ_j. There are only two projection operators that have an eigenvalue of one,

$$\hat{P}_{A_1} = \frac{1}{6} \begin{pmatrix} 4 & 1 & 1 \\ 1 & 1 & 4 \\ 1 & 4 & 1 \end{pmatrix}, \quad \text{and} \quad \hat{P}_{E_2} = \frac{1}{3} \begin{pmatrix} 2 & -1 & -1 \\ -1 & 2 & -1 \\ -1 & -1 & 2 \end{pmatrix}. \tag{4.34}$$

The corresponding normalized eigenfunctions are given by the extended s-wave solution $\mathbf{\Delta}_s = \frac{1}{\sqrt{3}}(1, 1, 1)$ for the A_1 irreducible representation, and the

Irrep	E	$2C_6$	$2C_3$	C_2	$3\sigma_v$	$3\sigma_d$
A_1	1	1	1	1	1	1
A_2	1	1	1	1	-1	-1
B_1	1	-1	1	-1	1	-1
B_2	1	-1	1	-1	-1	1
E_1	2	1	-1	-2	0	0
E_2	2	1	-1	-2	0	0

Table 4.2. *The character table for the group C_{6v} used to construct the basis functions on the hexagonal lattice.*

two d-waves $\mathbf{\Delta}_{x^2-y^2} = \frac{1}{\sqrt{6}}(2,-1,-1)$ and $\mathbf{\Delta}_{xy} = \frac{1}{\sqrt{2}}(0,1,-1)$ for the two-dimensional E_2 irreducible representation.

At large enough distance between twists, we expect the spin singlet order parameter in the harmonic honeycomb lattices to be of the same form as in superconducting graphene, where the extended s-wave is found at high doping levels and a complex $d \pm id'$ linear combination $\mathbf{\Delta}_{x^2-y^2} \pm i\mathbf{\Delta}_{xy}$ at lower doping [90, 91]. From plotting the overlap of the calculated order parameter with the basis functions in Figure 4.2 this expectation is supported by the calculations. The twist acts as a boundary between $d \pm id'$ regions, where the sign of the linear combination can be chosen independently on either side. Close to the twist the six-fold symmetry is no longer realized even approximately and the order parameter mixes all basis functions. This is very similar to the behavior close to a zigzag edge of the honeycomb lattice [100].

Starting from this solution, we study the superconducting state with changing distance between twists. The influence of the twist becomes apparent when tracking the overlap with the two d-wave basis functions at the center of the honeycomb region between twists, as shown in Fig. 4.3. As long as the six-fold symmetry is approximately fulfilled, the two d-waves are degenerate and form a $d \pm id'$ state. As the symmetry is destroyed by the approaching twist, the d_{xy} solution is suppressed and finally vanishes completely. Even though the remaining order parameter in these lattices has a large overlap with the $d_{x^2-y^2}$ solution, it should instead be considered in terms of the basis functions of D_{2h}, as the six-fold symmetry is no longer realized even approximately.

The superconducting spin singlet state on the large members of the harmonic honeycomb series is thus reasonably close to that of single layer graphene, as long as the distance to the twist is large enough to approximately preserve a six-fold symmetry.
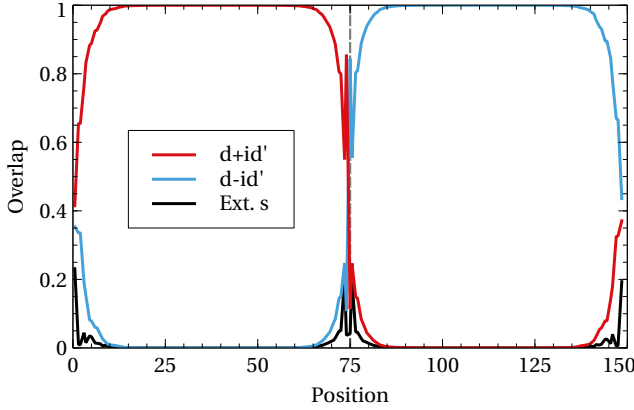
Figure 4.2. Plot of the overlap of the superconducting order parameter at each atomic site of a large harmonic honeycomb lattice with the $d + id'$, $d - id'$, and extended s-wave basis functions. The results known from the honeycomb lattice are recovered far away from the twist where the six-fold symmetry is approximately fulfilled. Figure taken from Paper I.

Irrep	E	$C_2(z)$	$C_2(y)$	$C_2(x)$
A	1	1	1	1
B_1	1	1	-1	-1
B_2	1	-1	1	-1
B_3	1	-1	-1	1

Table 4.3. *Character table for the group D_2 used to construct the basis functions on the smaller harmonic honeycomb lattices.*

4.4 Taking into account the accurate symmetries of the hyper- and stripyhoneycomb lattices

Similar to the the case for the large harmonic honeycomb lattices, classifying the spin singlet basis functions on the hyper- and stripyhoneycomb lattices is simplified by using a smaller point group. Instead of D_{2h}, which is the full point group, here I present the classification based on D_2. This is possible, because the behavior under inversion is already known. However, there is a small caveat in that the mirror symmetries of the harmonic honeycomb lattices are non-symmorphic symmetries. I will detail what this means for the basis functions below.

For the hyperhoneycomb lattice, the six nearest neighbor spin singlet order parameters can be grouped in the vector $\mathbf{\Delta} = (\Delta_1, \Delta_2, \Delta_3, \Delta_4, \Delta_5, \Delta_6)$. The character table of D_2 is given in Tab. 4.3 and the action of the group elements of
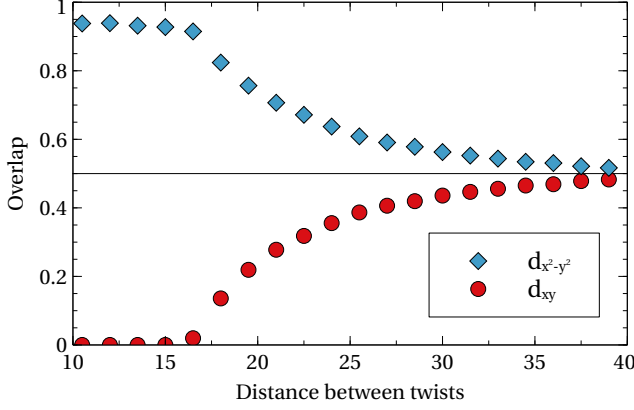
Figure 4.3. A decreasing distance between twists influences the overlap of the order parameter in the center of the regions between the twists with the two d-wave solutions. A perfect $d \pm id'$ state of degenerate d-waves is formed for large enough distances between twists. For smaller distances, the d_{xy}-state is suppressed. Figure taken from Paper I.

D_2 is captured by

$$E = \mathbb{1}, \tag{4.35}$$
$$C_2(z) = (1 \to 1, 2 \to 3, 3 \to 2, 4 \to 4, 5 \to 6, 6 \to 5), \tag{4.36}$$
$$C_2(y) = (1 \to 1, 2 \to 6, 3 \to 5, 4 \to 4, 5 \to 3, 6 \to 2), \tag{4.37}$$
$$C_2(x) = (1 \to 1, 2 \to 5, 3 \to 6, 4 \to 4, 5 \to 2, 6 \to 3). \tag{4.38}$$

Notably, the C_2 rotations leave the horizontal bonds untouched and project the zigzag bonds onto each other. This means the two groups of bonds decouple, which will lead to independent basis functions for the horizontal and zigzag bonds. Indeed, the projection operators for the four irreducible representations show the same behavior, forming block matrices of the form

$$
\hat{P}_A = \frac{1}{4}
\begin{pmatrix}
4 & 0 & 0 & 0 & 0 & 0 \\
0 & 1 & 1 & 0 & 1 & 1 \\
0 & 1 & 1 & 0 & 1 & 1 \\
0 & 0 & 0 & 4 & 0 & 0 \\
0 & 1 & 1 & 0 & 1 & 1 \\
0 & 1 & 1 & 0 & 1 & 1
\end{pmatrix},
\quad
\hat{P}_{B_1} = \frac{1}{4}
\begin{pmatrix}
0 & 0 & 0 & 0 & 0 & 0 \\
0 & 1 & 1 & 0 & -1 & -1 \\
0 & 1 & 1 & 0 & -1 & -1 \\
0 & 0 & 0 & 0 & 0 & 0 \\
0 & -1 & -1 & 0 & 1 & 1 \\
0 & -1 & -1 & 0 & 1 & 1
\end{pmatrix},
\tag{4.39}
$$

with similar projection operators for B_2 and B_3, which I omit here. The construction of the basis functions can be performed by applying the projection operators on the general function $\mathbf{\Delta}$ and requiring that Eq. (4.31) holds. For

70

the A irreducible representation this is fulfilled by the basis functions

$$\boldsymbol{\Delta}_A^{1a} = (1,0,0,0,0,0), \tag{4.40}$$

$$\boldsymbol{\Delta}_A^{1b} = (0,0,0,1,0,0), \tag{4.41}$$

$$\boldsymbol{\Delta}_{A_g}^2 = (0,1,1,0,1,1). \tag{4.42}$$

As expected, the horizontal and zigzag bonds decouple. In fact, there are independent basis functions for each of the two horizontal bonds. However, when taking into account the non-symmorphic mirror symmetries, the horizontal bonds will be mapped onto each other. A basis function that is also even under those mirror symmetries should therefore be the linear combination

$$\boldsymbol{\Delta}_{A_g}^1 = \boldsymbol{\Delta}_A^{1a} + \boldsymbol{\Delta}_A^{1b} = (1,0,0,1,0,0), \tag{4.43}$$

where the A_g label indicates a spin singlet basis function for the D_{2h} point group, which are the basis functions listed in Paper I and III. Because there are no symmetries relating the two remaining basis functions of the A irreducible representation, they can form a linear combination with arbitrary coefficient. The basis functions for the remaining irreducible representations only involve the zigzag bonds and are given by

$$\boldsymbol{\Delta}_{B_{1g}} = (0,1,-1,0,1,-1), \tag{4.44}$$

$$\boldsymbol{\Delta}_{B_{2g}} = (0,1,-1,0,-1,1), \tag{4.45}$$

$$\boldsymbol{\Delta}_{B_{3g}} = (0,1,1,0,-1,-1). \tag{4.46}$$

In Paper I we identify four different superconducting phases in the J-μ phase diagram of the hyperhoneycomb lattice pictured in Figure 4.4. At large doping, the two basis functions of the A irreducible representation form a linear combination of the form

$$\begin{aligned}\boldsymbol{\Delta}_g &= a\boldsymbol{\Delta}_{A_g}^1 + b\boldsymbol{\Delta}_{A_g}^2 \\ &= (a,b,b,a,b,b),\end{aligned} \tag{4.47}$$

where a and b are positive real numbers. The horizontal and zigzag bonds thus have different magnitude but the same phase. This state is related to an extended s-wave pairing at $a = b$ and leads to a fully gapped density of states (DOS) as shown in Figure 4.5. Another solution is found at lower doping levels, which is characterized by the linear combination

$$\begin{aligned}\boldsymbol{\Delta}_n &= a\boldsymbol{\Delta}_{A_g}^1 - b\boldsymbol{\Delta}_{A_g}^2 \\ &= (a,-b,-b,a,-b,-b).\end{aligned} \tag{4.48}$$

In this solution the order parameter obtains a phase of π on the zigzag bonds. Such a sign change hints at a nodal DOS, as is verified in Fig. 4.5. In Paper III
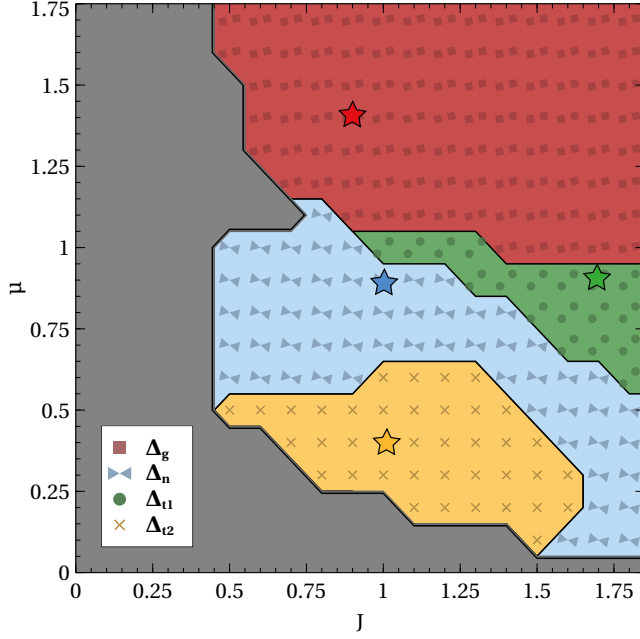
Figure 4.4. Phase diagram of spin singlet superconductivity on the hyperhoneycomb lattice at zero temperature. A nodal state $\mathbf{\Delta}_n$ (blue region) is stabilized at low doping, while the system is in the completely gapped state $\mathbf{\Delta}_g$ (red region) at higher doping. In between these two regions we find a completely gapped time-reversal symmetry breaking state $\mathbf{\Delta}_{t1}$ (green region). A fourth solution $\mathbf{\Delta}_{t2}$ breaks time-reversal symmetry and is characterized by nodal points (orange region). The stars mark the positions where the DOS in Fig. 4.5 is obtained. Figure taken from Paper I.
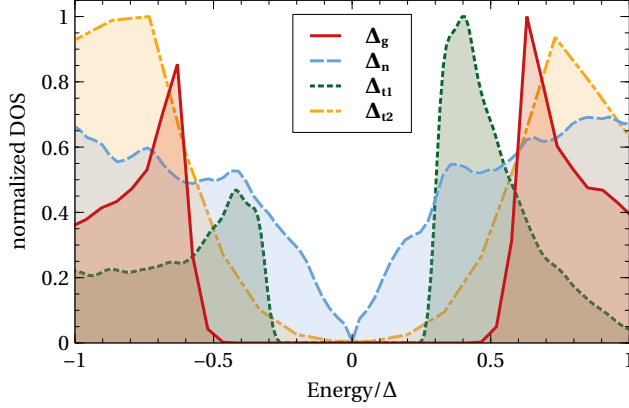
Figure 4.5. Normalized DOS as a function of energy taken at the four different points in the phase diagram marked by stars in Fig. 4.4. The characteristic behavior of each of the four solutions, fully gapped, nodal points or lines, is clearly visible. Figure taken from Paper I.

we explicitly identify the nodes as two lines of zeros. Both the extended *s*-wave and the nodal phase obey time-reversal symmetry. The two remaining solutions on the other hain turn form explicitly complex linear combinations which break time-reversal. An intermediate phase at larger interaction strengths is characterized by

$$\mathbf{\Delta}_{t_1} = a\mathbf{\Delta}_{A_g}^1 + b\mathrm{e}^{\mathrm{i}\phi}\mathbf{\Delta}_{A_g}^2$$
$$= (a, b\mathrm{e}^{\mathrm{i}\phi}, b\mathrm{e}^{\mathrm{i}\phi}, a, b\mathrm{e}^{\mathrm{i}\phi}, b\mathrm{e}^{\mathrm{i}\phi}), \tag{4.49}$$

where the relative phase ϕ is different from 0 and π. The DOS in Fig. 4.5 highlights that this state completely gaps out the Fermi surface, too. All three phases transform according to the trivial irreducible representation and the diverse structure of the solutions is enabled by the independence of horizontal and zigzag bonds. The final solution located in the zero temperature phase diagram at low doping values mixes the A and B_1 or B_2 irreducible representations

$$\mathbf{\Delta}_{t_2} = a\mathbf{\Delta}_{A_g}^1 - b\mathbf{\Delta}_{A_g}^2 + \mathrm{i}c\mathbf{\Delta}_{B_{1/2g}}$$
$$= (a, -b + \mathrm{i}c, -b - \mathrm{i}c, a, -b \mp \mathrm{i}c, -b \pm \mathrm{i}c), \tag{4.50}$$

which is equivalent to a linear combination of the form $\mathbf{\Delta}_n + \mathrm{i}c\mathbf{\Delta}_{B_{1/2g}}$, where c is also real and positive. This solutions gaps out the nodes of $\mathbf{\Delta}_n$ except for four points. This gives rise to the quadratic DOS evident in Fig. 4.5.

A similar classification can be performed for the stripyhoneycomb lattice. The results are very similar to the hyperhoneycomb lattice, so here I highlight only the differences. In the stripyhoneycomb lattice, the bonds split into

Irrep	E	$2C_3$	$3C_2'$	I	$2S_6$	$3\sigma_d$
A_{1g}	1	1	1	1	1	1
A_{2g}	1	1	-1	1	1	-1
E_g	2	-1	0	2	-1	0
A_{1u}	1	1	1	-1	-1	-1
A_{2u}	1	1	-1	-1	-1	1
E_u	2	-1	0	-2	1	0

Table 4.4. *Character table for the group D_{3d} applicable for determining the basis functions for pairing arising from the extended Kitaev-Heisenberg model on the honeycomb lattice.*

three groups, as there are now two different kinds of horizontal bonds: Those at a twist and those within a honeycomb sheet. This gives rise to three basis functions for the trivial irreducible representation, while the B irreducible representations still have only one basis function governing solely the zigzag bonds. The phase diagram shares many features with the hyperhoneycomb lattice and is extensively discussed in Paper I.

The symmetry classification of the spin singlet pairing on the small members of the harmonic honeycomb lattices thus reveals a rich phase diagram which is very similar for both members. It includes superconducting states giving rise to nodal lines that are connected to sign changes of the bond order parameters. The phase diagram furthermore displays some similarities to that of single layer graphene, like the extended s-wave phase stabilized at large doping.

4.5 The role of spin-orbit coupling in the classification of spin triplet pairing on the honeycomb lattice

In the extended Kitaev-Heisenberg model on the honeycomb lattice, the symmetry is reduced compared to the spin singlet pairing. Instead of a D_{6h} symmetry, the additional Kitaev and off-diagonal exchanges reduce the symmetry to D_{3d}, whose character table is shown in Tab. 4.4. A way to visualize the lowered symmetry is to embed the honeycomb lattice in the octahedral cages present in the material realizations of the model. While the classification of the spin singlet pairing for this point group is essentially analogous to that in the harmonic honeycomb lattices presented in Sec. 4.3, the basis functions for the spin triplet pairing determined in Paper II are more intricate.

As detailed in Sec. 3.4, the spin triplet order parameters are grouped into the $\boldsymbol{d}$-vector. Each component d^γ ($\gamma = x, y, z$) has three bond order parameters

d_i^γ ($i = 1, 2, 3$). For visualization, they are grouped in a matrix of the form

$$\boldsymbol{d} = \begin{pmatrix} d_1^x & d_2^x & d_3^x \\ d_1^y & d_2^y & d_3^y \\ d_1^z & d_2^z & d_3^z \end{pmatrix}. \tag{4.51}$$

When considering spin and orbital degrees of freedom independently, the action of symmetry operations in the point group leave the spin, and therefore the $\boldsymbol{d}$-vector, untouched. Then the three $\boldsymbol{d}$-vector components can be treated individually. This classification has been performed in the context of the pure Kitaev-Heisenberg model without the off-diagonal exchange [33] and yields three basis functions for each component of the $\boldsymbol{d}$-vector

$$d_{A_{1u}}^\gamma = (1,1,1), \qquad d_{E_u,1}^\gamma = (-1,0,1), \qquad d_{E_u,2}^\gamma = (-1,1,0). \tag{4.52}$$

When grouping the basis functions by irreducible representation, there are thus three basis functions for the one-dimensional A_{1u} irreducible representation and six basis functions for the two-dimensional E_u irreducible representation. This is similar to the situation in the harmonic honeycomb lattices, where there were several order parameter groups, that were not related by symmetry. In this case these groups correspond to the $\boldsymbol{d}$-vector components. This again allows for linear combinations of the basis functions of a certain irreducible representation, which is indeed what has been found in the Kitaev-Heisenberg model [33].

When including the strong spin-orbit coupling of the Kitaev materials in the classification, a rotation of the lattice must be coupled to a rotation of the $\boldsymbol{d}$-vector, as if it were frozen in the lattice. This will connect the different components and they are no longer independently classifiable. A representation of the D_{3d} point group is then characterized by

$$E = \mathbb{1}_s \otimes \mathbb{1}_o, \tag{4.53}$$
$$C_3 = (x \to y, y \to z, z \to x) \otimes (1 \to 2, 2 \to 3, 3 \to 1), \tag{4.54}$$
$$C_2' = (x \to -x, y \to -z, z \to -y) \otimes (1 \to 1, 2 \to 3, 3 \to 2), \tag{4.55}$$
$$I = -\mathbb{1}_s \otimes \mathbb{1}_o, \tag{4.56}$$
$$S_6 = (x \to z, y \to x, z \to y) \otimes (1 \to -3, 2 \to -1, 3 \to -2), \tag{4.57}$$
$$\sigma_d = (x \to -x, y \to -z, z \to -y) \otimes (1 \to -1, 2 \to -3, 3 \to -2), \tag{4.58}$$

where the first entry acts on the components of the $\boldsymbol{d}$-vector and the second transforms the nearest neighbor spin triplet order parameters. This means, for example, that the $\frac{2\pi}{3}$ rotation around the axis perpendicular to the honeycomb lattice is combined with a rotation around the $(1,1,1)$ axis in spin space, such that the three $\boldsymbol{d}$-vector components are cyclically permuted. The projection operators can be computed in accordance with Eq. (4.15) and mix the $\boldsymbol{d}$-vector components as expected. Calculating the eigenvectors with eigenvalue one

yields the following nine basis functions

$$d_{A_{1u}} = \begin{pmatrix} 0 & -1 & 1 \\ 1 & 0 & -1 \\ -1 & 1 & 0 \end{pmatrix}, \tag{4.59}$$

$$d_{A_{2u},1} = \begin{pmatrix} 1 & 0 & 0 \\ 0 & 1 & 0 \\ 0 & 0 & 1 \end{pmatrix}, \qquad d_{A_{2u},2} = \begin{pmatrix} 0 & 1 & 1 \\ 1 & 0 & 1 \\ 1 & 1 & 0 \end{pmatrix}, \tag{4.60}$$

$$d_{E_u,1} = \frac{1}{\sqrt{6}} \begin{pmatrix} 2 & 0 & 0 \\ 0 & -1 & 0 \\ 0 & 0 & -1 \end{pmatrix}, \qquad d_{E_u,2} = \frac{1}{\sqrt{2}} \begin{pmatrix} 0 & 0 & 0 \\ 0 & -1 & 0 \\ 0 & 0 & 1 \end{pmatrix}, \tag{4.61}$$

$$d_{E_u,3} = \frac{1}{\sqrt{6}} \begin{pmatrix} 0 & 2 & 0 \\ 0 & 0 & -1 \\ -1 & 0 & 0 \end{pmatrix}, \qquad d_{E_u,4} = \frac{1}{\sqrt{2}} \begin{pmatrix} 0 & 0 & 0 \\ 0 & 0 & -1 \\ 1 & 0 & 0 \end{pmatrix}, \tag{4.62}$$

$$d_{E_u,5} = \frac{1}{\sqrt{6}} \begin{pmatrix} 0 & 0 & -1 \\ -1 & 0 & 0 \\ 0 & 2 & 0 \end{pmatrix}, \qquad d_{E_u,6} = \frac{1}{\sqrt{2}} \begin{pmatrix} 0 & 0 & 1 \\ -1 & 0 & 0 \\ 0 & 0 & 0 \end{pmatrix}, \tag{4.63}$$

where I present a specific orthonomal form of the E_u basis functions that differs from that included in Paper II. Again, the six E_u basis functions consist of three different sets ($\{1,2\},\{3,4\},\{5,6\}$) that are not related by symmetry. These do not correspond directly to the d-vector components anymore. Instead, the different sets are made up from the diagonal and the two off-diagonals of the matrix presentation,

$$\begin{pmatrix} d_1^x & 0 & 0 \\ 0 & d_2^y & 0 \\ 0 & 0 & d_3^z \end{pmatrix}, \qquad \begin{pmatrix} 0 & d_2^x & 0 \\ 0 & 0 & d_3^y \\ d_1^z & 0 & 0 \end{pmatrix}, \qquad \begin{pmatrix} 0 & 0 & d_3^x \\ d_1^y & 0 & 0 \\ 0 & d_2^z & 0 \end{pmatrix}. \tag{4.64}$$

Notably, the C_3 operator, which simultaneously rotates the d-vector in spin space and the three nearest-neighbor bonds, links the elements of each of these (off-)diagonals, which explains intuitively why the resulting basis functions mix the components of the d-vector.

Having obtained the basis functions, it is possible to characterize the spin triplet phase diagram of the extended Kitaev-Heisenberg model calculated in Paper II and shown in Fig. 4.6. With only Kitaev and Heisenberg exchange, the spin triplet order parameters identified in self-consistency calculations transform according to the E_u irreducible representation of the classification without SOC [33]. Each d-vector component is made up of a linear combination of the two E_u basis functions for that component

$$d^x = (0,-1,1), \qquad d^y = (1,0,-1), \qquad d^z = (-1,1,0). \tag{4.65}$$
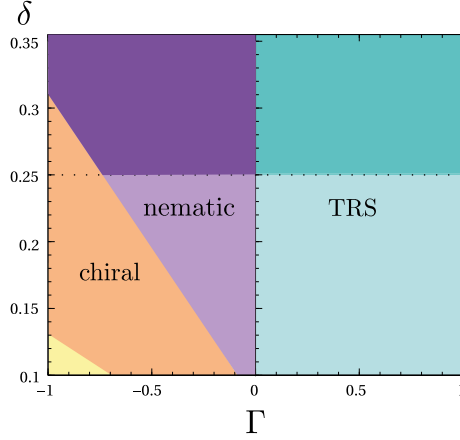
Figure 4.6. The phase diagram of the spin triplet order parameters arising from doping the extended Kitaev-Heisenberg model displays a multitude of phases. For $K = -t$, there is a clear distinction between positive and negative values of the symmetric off-diagonal exchange term Γ. A time-reversal symmetric solution $\boldsymbol{d}_{\Gamma>0}$ (cyan) is stable at all doping levels for $\Gamma > 0$. Another time-reversal symmetric solution that also breaks the C_3 symmetry, $\boldsymbol{d}_{\text{nematic}}$ (purple), is found for $\Gamma < 0$ at large doping. In the orange region at intermediate doping and $\Gamma < 0$ an order parameter $\boldsymbol{d}_{\text{chiral}}$ breaking time-reversal symmetry appears. Figure taken from Paper II

The total $\boldsymbol{d}$-vector is then formed by four different linear combinations of the individual components, which are all found to be degenerate

$$\boldsymbol{d}_{\Gamma=0} = |\boldsymbol{d}|(d^x\hat{\boldsymbol{e}}_x \pm d^y\hat{\boldsymbol{e}}_y \pm d^z\hat{\boldsymbol{e}}_z). \tag{4.66}$$

The degeneracy is due to a four-fold symmetry in choosing the spin quantization axes for the Kitaev interaction. As soon as a finite value of the off-diagonal exchange $\Gamma > 0$ is added, the quantization axes are fixed, the degeneracy is lifted, and only one self-consistent solution remains. It corresponds to the basis function of the A_{1u} irreducible representation of the classification with SOC

$$\boldsymbol{d}_{\Gamma>0} = |\boldsymbol{d}|\,\boldsymbol{d}_{A_{1u}} = |\boldsymbol{d}| \begin{pmatrix} 0 & -1 & 1 \\ 1 & 0 & -1 \\ -1 & 1 & 0 \end{pmatrix}, \tag{4.67}$$

which is equivalent to the linear combination with only plus signs $\boldsymbol{d} \propto d^x\hat{\boldsymbol{e}}_x + d^y\hat{\boldsymbol{e}}_y + d^z\hat{\boldsymbol{e}}_z$ observed at $\Gamma = 0$ in Eq. (4.66). A finite positive value of Γ thus locks the $\boldsymbol{d}$-vector along the $(1,1,1)$ direction, which is perpendicular to the honeycomb layer.

At negative values of Γ, there are two different solutions that each break further symmetries. For lower doping, we find a time-reversal symmetry breaking

solution of the form

$$d_{\text{chiral}} = |d| \left\{ (d_{E_u,3} + d_{E_u,5}) \pm i(d_{E_u,4} - d_{E_u,6}) \right\}$$
$$= |d| \begin{pmatrix} 0 & 1 & e^{\pm i2\pi/3} \\ e^{\mp i2\pi/3} & 0 & e^{\pm i2\pi/3} \\ e^{\mp i2\pi/3} & 1 & 0 \end{pmatrix}, \tag{4.68}$$

where the two solutions $\pm$ are degenerate and of opposite chirality. We note directly that this order parameter is non-unitary as $d_{\text{chiral}}* \neq d_{\text{chiral}}$ [4]. At higher doping levels, the order parameter preserves time-reversal symmetry, but breaks the rotational symmetry of the lattice by forming the real linear combination

$$d_{\text{nematic}} = |d| \left\{ (\cos(\alpha) d_{E_u,3} + \sin(\alpha) d_{E_u,4}) \pm (\cos(\beta) d_{E_u,5} + \sin(\beta) d_{E_u,6}) \right\}. \tag{4.69}$$

We find that the pairs $(\alpha, \beta) = (20° + n60°, -40° + n60°)$ with $n \in \{1, \ldots, 6\}$ and the different $\pm$ solutions are degenerate (up to numerical accuracy). They give an order parameter of the form

$$d_{\text{nematic}} = |d| \begin{pmatrix} 0 & a & \mp a \\ \mp b & 0 & \mp c \\ b & c & 0 \end{pmatrix}, \tag{4.70}$$

where $a, b, c \in \mathbb{R}$. This particular choice of the angles breaks the C_3 symmetry of the lattice, but remains symmetric under C_2'. Superconductors exhibiting this rotational symmetry breaking in their order parameter have been named "nematic" superconductors [101, 37]. The symmetry breaking is clearly visible when transforming the order parameter into the band picture, as detailed in Sec. 3.4. The intraband order parameter for the choice $(80°, 20°)$ is plotted in Fig. 4.7 and clearly demonstrates the nematicity.

In summary, the phase diagram of spin triplet pairing arising from the doping the extended Kitaev-Heisenberg model features a time-reversal symmetric solution transforming according to the A_{1u} irreducible representation of the point group D_{3d} at $\Gamma \geq 0$ and two solutions forming linear combinations of the basis functions of the E_u irreducible representation at $\Gamma < 0$. The complex linear combination stable at intermediate doping breaks time-reversal symmetry, while the real linear combination formed at larger doping levels leads to a nematic superconducting state that breaks the rotation symmetry of the lattice.

4.6 A first attempt at classifying spin triplet pairing on the hyperhoneycomb lattice

For Paper V, we perform a classification of the spin triplet pairing on the hyperhoneycomb lattice. Several results from the previous sections can be used
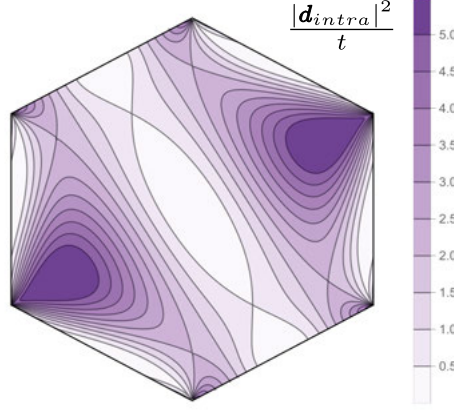
Figure 4.7. Plot of the square of the absolute value of the intraband spin triplet order parameter $|\boldsymbol{d}_{\text{intra}}(\boldsymbol{k})|^2$ in the first Brillouin zone for the time-reversal symmetric nematic order. The breaking of the C_3 symmetry is clearly visible. Figure taken from Paper II.

as stepping stones. First of all, it is reasonable to perform a classification with and without spin-orbit coupling, as in Sec. 4.5. Secondly, the classification can be based on the D_2 point group instead of the full D_{2h} group, taking into account the role of the non-symmorphic mirror symmetries, as discussed in Sec. 4.3. This section also contains the character table of D_2 in Tab. 4.3.

Without spin-orbit coupling, the group elements of the D_2 point group act on the individual $\boldsymbol{d}$-vector components and are summarized by

$$E_o = \mathbb{1}_o, \tag{4.71}$$
$$C_2(z)_o = (1 \to 1, 2 \to 3, 3 \to 2, 4 \to 4, 5 \to 6, 6 \to 5), \tag{4.72}$$
$$C_2(y)_o = (1 \to -1, 2 \to -5, 3 \to -6, 4 \to -4, 5 \to -2, 6 \to -3), \tag{4.73}$$
$$C_2(x)_o = (1 \to -1, 2 \to -6, 3 \to -5, 4 \to -4, 5 \to -3, 6 \to -2), \tag{4.74}$$

using the same notation as Eq. (4.38). In difference to the spin singlet classification in Sec. 4.4, some of the order parameters obtain a minus sign under some of the transformations due to the oddness of the order parameter. The choice of x, y, and z axes for the symmetry operators is also slightly different compared to the singlet classification, but consistent with the definitions in Sec. 2.2 and Fig. 2.6 to ensure the simple form of the Kitaev and off-diagonal exchanges. The projection operators are constructed as previously described and are very similar to the projection operators for the spin singlet classification. The basis functions correspond to the eigenvectors of the projection

operators with eigenvalue one, which are

$$d_{A_u} = \frac{1}{2}(0,-1,-1,0,1,1), \qquad d_{B_{1u}}^1 = (1,0,0,0,0,0), \qquad (4.75)$$

$$d_{B_{2u}} = \frac{1}{2}(0,-1,1,0,-1,1), \qquad d_{B_{1u}}^2 = (0,0,0,1,0,0), \qquad (4.76)$$

$$d_{B_{3u}} = \frac{1}{2}(0,1,-1,0,-1,1), \qquad d_{B_{1u}}^3 = \frac{1}{2}(0,1,1,0,1,1), \qquad (4.77)$$

Because these are spin triplet basis functions, which are odd under inversion, I added the corresponding u label to the basis functions. The basis functions $d_{B_{1u}}^1$ and $d_{B_{1u}}^2$ are no longer as easily combined under the action of the non-symmorphic symmetries as the spin singlet basis functions Δ_A^{1a} and Δ_A^{1b} in Sec. 4.4, because they do not belong to the trivial irreducible representation.

Once spin-orbit coupling is included, the group elements again act on both the sublattice degrees of freedom and spin. While the action on the sublattice degrees is the same as given above, the group elements act on spin in the following way

$$E_s = \mathbb{1}_s, \qquad (4.78)$$
$$C_2(z)_s = (x \to -x, y \to -z, z \to -y), \qquad (4.79)$$
$$C_2(y)_s = (x \to -x, y \to z, z \to y), \qquad (4.80)$$
$$C_2(x)_s = (x \to x, y \to -y, z \to -z). \qquad (4.81)$$

In total, the action of the group elements is then given by $g_s \otimes g_o$. While the x-axis of the local and Cartesian coordinate systems are identical, the y- and z-axes are rotated. The rotations then map the y and z-components of the d-vector onto each other. As in the discussion of the spin triplet pairing on the honeycomb lattice, this leads to basis functions mixing d-vector components, such that the d-vector is pinned along the symmetry axes of the three rotations. There are 18 different order parameters, which leads to a large number of basis functions. They are too lengthy to print here, particularly as I have not yet been able to use them to express the solutions discussed below in a concise way. Instead, I will attempt to classify all solutions found at zero temperature in terms of the non-spin-orbit coupled basis functions.

In the absence of the spin-orbit coupled hopping t_{KM}, we identify two different solutions. For small values of $|\Gamma|$, the d-vector points along the $\hat{y}$ direction, taking the form

$$\boldsymbol{d}_1 = (a,0,-b,a,-b,0)\hat{\boldsymbol{e}}_y, \qquad (4.82)$$

with $a,b \in \mathbb{R}$ and $a > b > 0$. In terms of the basis functions this can be represented as a linear combination of the form

$$d_1^y = a(d_{B_{1u}}^1 + d_{B_{1u}}^2) + b(d_{B_{1u}}^3 + d_{B_{3u}}). \qquad (4.83)$$
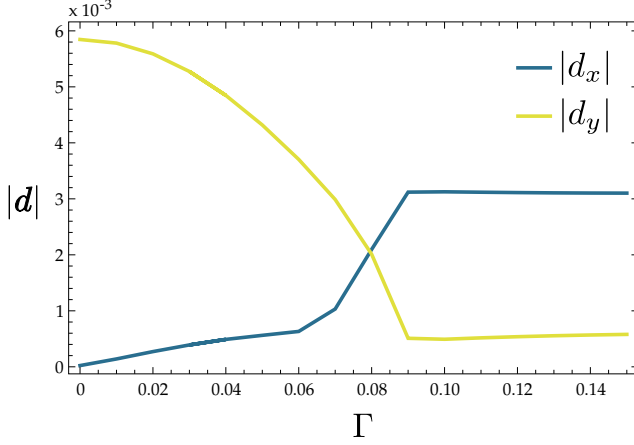
80

Figure 4.8. The off-diagonal exchange Γ drives a crossover between the two solutions $\boldsymbol{d}_1$ and $\boldsymbol{d}_2$ in the absence of the spin-orbit coupled hopping. The $\boldsymbol{d}_1$ solution is dominant at $\Gamma = 0$, as can be seen by the large y-component of the order parameter (yellow). Increasing Γ, it is rapidly decreased, while the x-component (blue) grows. $\Gamma \gtrsim 0.08$ gives rise to a stable $\boldsymbol{d}_2$ solution. The doping level is set to $\delta = 0.25$.

The solution thus mixes basis functions from different irreducible representations, which would be possible if the irreducible representations B_{1u} and B_{3u} are accidentally degenerate in the $\Gamma = 0$ limit at the critical temperature. This is supported by the observation that the state is strongest at $\Gamma = 0$ and decreases in size when increasing Γ. The ratio $\frac{a}{b}$ is furthermore strongly increased when adding an anisotropy between the horizontal and zigzag bonds in the interaction $\Delta K = \frac{K_z}{K_{x,y}}$, which could also lift the accidental degeneracy.

A second solution is found to be stable for $|\Gamma| \gtrsim 0.08$, where the $\boldsymbol{d}$-vector gradually rotates into the $\hat{x}$-direction,

$$\boldsymbol{d}_2 = (c, 0, 0, c, 0, 0)\hat{\boldsymbol{e}}_x, \tag{4.84}$$

where again $c \in \mathbb{R}$ and $c > 0$. This state corresponds to the linear combination

$$d_2^x = c(d_{B_{1u}}^1 + d_{B_{1u}}^2), \tag{4.85}$$

when using the classification without spin-orbit coupling and there is thus no mixing of irreducible representations in this solution. This supports the theory of accidental degeneracy at $\Gamma = 0$ supporting the $\boldsymbol{d}_1$ state, as increasing $|\Gamma|$ yields a slow crossover between the two solutions, as shown in Fig. 4.8. The y component of the $\boldsymbol{d}$ vector attributed to the $\boldsymbol{d}_1$ solutions is decreased, while the x component transforming as the $\boldsymbol{d}_2$ solution increases. This transition causes the overall size of the order parameter to be largest at $\Gamma = 0$, to decrease until the crossover to the $\boldsymbol{d}_2$ solution, and to finally plateau for further increase in Γ.
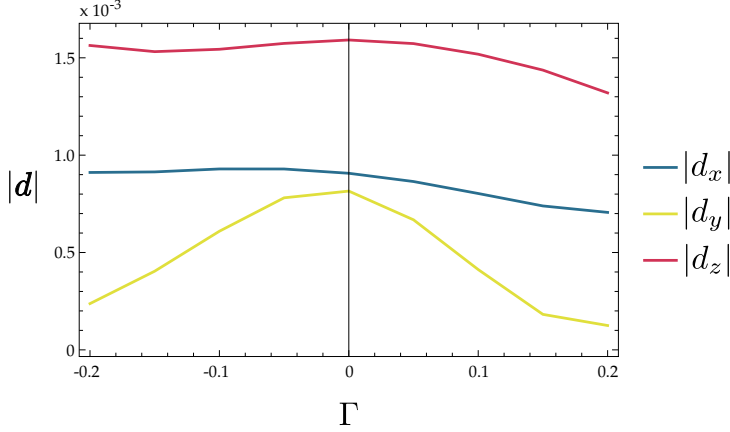
Figure 4.9. Suppression of the *y* component of the $\boldsymbol{d}$-vector by the off-diagonal exchange Γ when the spin-orbit coupled hopping is large, here $t_{KM} = 0.8$. The doping level is tuned to $\delta = 0.15$.

Even though the two solutions are different from their symmetry classification, both solutions are characterized by a nodal line, which gives rise to a characteristic v-shaped density of states.

Including a sizable spin-orbit coupled hopping $t_{KM} > 0.5t$ yields a different superconducting state, which includes all three components of the $\boldsymbol{d}$-vector

$$\boldsymbol{d}_{SO} = (a,0,0,a,0,0)\hat{\boldsymbol{e}}_x + (0,0,b,0,-b,0)\hat{\boldsymbol{e}}_y + (0,0,-c,0,c,0)\hat{\boldsymbol{e}}_z, \quad (4.86)$$

where again, *a*, *b*, and *c* are positive real numbers. In terms of the basis functions, this can be expressed as

$$\boldsymbol{d}_{SO} = a(d^1_{B_{1u}} + d^2_{B_{1u}})\hat{\boldsymbol{e}}_x + b(d_{B_{A_u}} - d_{B_{2u}})\hat{\boldsymbol{e}}_y - c(d_{B_{A_u}} - d_{B_{2u}})\hat{\boldsymbol{e}}_z, \quad (4.87)$$

which mixes three irreducible representations, A_u, B_{1u} and B_{2u}. This is highly unusual and an indication that the classification without spin-orbit coupling might not be enough to characterize the order parameter. The individual strength of the three $\boldsymbol{d}$-vector components are dependent on the off-diagonal exchange Γ. Fig. 4.9 shows especially how the parameter *b* is strongly suppressed for increasing Γ, here for $\delta = 0.15$ and $t_{KM} = 0.8$. This has the strange effect, that the overall size of the order parameter decreases when the interaction strength increases, as observed also without the spin-orbit coupled hopping. Both positive and negative values of Γ preserve the overall symmetry of the order parameter and only change the direction of the $\boldsymbol{d}$-vector.

The nodal lines characteristic for the solutions discussed in the absence of the spin-orbit coupled hopping are gapped out by the additional terms in $\boldsymbol{d}_{SO}$ in favor of individual point nodes.

The extended Kitaev-Heisenberg interactions on the hyperhoneycomb lattice thus give rise to distinct superconducting states in the absence or presence

of the spin-orbit coupled hopping. At $t_{KM} = 0$, we find a competition between two line nodal states, which can be tuned by the off-diagonal exchange or an anisotropy in the interactions. A possible explanation would be an accidental degeneracy in the limit of $\Gamma = 0$, although a more complete explanation might require an understanding in terms of the basis functions obtained when taking spin-orbit coupling into account. Similarly, the point nodal state found throughout for large values of the spin-orbit coupled hopping appears to be mixing several irreducible representations, which would require a series of transitions. It is more likely that a more thorough understanding of the basis functions in the presence of spin-orbit coupling will reveal a simpler explanation, as in the case on the honeycomb lattice discussed in Sec. 4.5.

5. Topological superconductors

Apart from the classification in terms of symmetries, superconducting states can also be studied from the viewpoint of topology. Indeed, several of the superconducting order parameters identified in the Kitaev materials display topologically non-trivial behavior, as discussed in Papers I-III and V. In this chapter I present an introduction to the topological classification of super-conductors, in large parts based on a number of reviews on the topic [9, 12, 99, 102]. To get a general idea of the concept, I introduce an example of topological phases outside of superconductors, before introducing the basics of classifying gapped Hamiltonians. The next section focuses on the role of symmetries on the classification, introducing the periodic table of topological insulators and superconductors as well as discussing symmetry-protected and nodal states. The topological invariants characterizing a number of topological phases in superconductors are introduced at first generally in Sec. 5.3, before actual approaches to calculate the invariants are presented in Sec. 5.4. After a brief discussion of bulk-boundary correspondence and Majorana fermions the chapter is concluded by presenting the results obtained in papers I-II and V.

5.1 General idea

An intuitive example of the kind of mapping that can be classified by topology is a one-dimensional chain of spins as pictured in Figure 5.1. Each position in real space r along the chain is assigned a spin of unit length that is constrained to a plane that includes the direction of the chain and winds continuously along the chain. Essentially, this corresponds to assigning each position an angle $\theta(r)$ between 0 and 2π. Considering periodic boundary conditions

Figure 5.1. Two 1D spin chains to illustrate the concept of nontrivial topological mappings. The chain in a) does not wind around the unit circle c) and is therefore topologically trivial, while the chain in b) winds once, as shown in d), and is therefore classified by a finite winding number.

and a continuous version of the chain, this is a mapping from the unit circle to the unit circle $\theta : S^1 \to S^1$. The different topological phases of this mapping distinguish different windings of the spin while going along the chain that cannot be continuously transformed into each other. The spins in the chain in Fig. 5.1 begin to rotate clockwise from the upwards state to the downwards state and then wind back counterclockwise. They thus only trace out the angles $[0, \pi]$ and do not wind around the full circle, as illustrated in Fig 5.1 c). It is possible to find a continuous mapping that rotates all spins into the upwards position, meaning this state is topologically trivial. The spins in the chain in Fig. 5.1 b), on the other hand, perform one full rotation when going along the chain and thereby trace out the full circle $[0, 2\pi]$, winding once (see Fig. 5.1 d)). A mapping that would transform this chain into the all up chain must have a discontinuity, for example at the center spin, where the spin on the left of it would need to be rotated by an angle of π and the angle to the right of it by $-\pi$. This chain is therefore representative of a different topological phase, where the spins wind once when going along the chain. It is directly clear that there must be an integer number of different phases, corresponding to the amount of windings the spins perform. These different topological phases or equivalence classes of the mapping $\theta : S^1 \to S^1$ are captured in the homotopy group $\pi_1(S^1) = \mathbb{Z}$. Another noteworthy fact is that this classification requires the spins to lie in the plane. As soon as they are allowed to point out of the plane, the two chains in Fig. 5.1 can be transformed into each other by winding into the third dimension.

Topologically classifying insulators and superconductors is less intuitive than the example of the spin chain. The classification is based on mappings from reciprocal space instead of real space and the target spaces are not as obvious. The principle can nevertheless be understood from a simple example [99, 9]: The starting point is a Hamiltonian defined in reciprocal space $\hat{h}(\boldsymbol{k})$ giving rise to a gapped spectrum at each momentum $\boldsymbol{k}$ in the periodic first Brillouin zone through the diagonalization

$$\hat{U}^\dagger(\boldsymbol{k})\hat{h}(\boldsymbol{k})\hat{U}(\boldsymbol{k}) = \mathrm{diag}\left(\varepsilon_{m+n}(\boldsymbol{k}), \ldots, \varepsilon_{n+1}(\boldsymbol{k}), \varepsilon_n, \ldots, \varepsilon_1(\boldsymbol{k})\right), \quad (5.1)$$

with the $n + m = N$ total energy bands ε_i sorted in descending order. Assuming a gap between the bands at n and $n+1$, $\varepsilon_{n+1}(\boldsymbol{k}) > 0 > \varepsilon_n(\boldsymbol{k})$ throughout the whole Brillouin zone, and the Hamiltonian can be to continuously transformed into the flat band form

$$\hat{\bar{h}}(\boldsymbol{k}) = \hat{U}^\dagger(\boldsymbol{k})\hat{h}(\boldsymbol{k})\hat{U}(\boldsymbol{k}) = \begin{pmatrix} \mathbb{1}_m & 0 \\ 0 & -\mathbb{1}_n \end{pmatrix}. \quad (5.2)$$

All bands below (above) the gap are thus assigned an energy $+1(-1)$, reflecting the splitting of the Hilbert space of $\hat{h}(\boldsymbol{k})$ by the gap. The flat band Hamiltonian $\hat{\bar{h}}(\boldsymbol{k})$ comes with an extra gauge symmetry: The $(n+m) \times (n+m)$ matrix $\hat{U}(\boldsymbol{k})$ that diagonalizes the Hamiltonian is an element of the unitary group

$U(n+m)$. However, the upper or lower band can be freely transformed by another $U(n)$ and $U(m)$ transformation, respectively. This means that $\hat{h}(\boldsymbol{k})$ defines a mapping from the Brillouin zone, which is a d dimensional torus T^d, to the space $C_0 := U(n+m)/(U(n) \times U(m))$

$$\hat{h} : T^d \to C_0. \tag{5.3}$$

The group of equivalence classes or topological phases of this mapping are then given by the homotopy group $\pi_d(C_0)$ [99, 9],

$$\pi_d(C_0) = \begin{cases} 0, & d = 1,3 \\ \mathbb{Z}, & d = 2. \end{cases} \tag{5.4}$$

This makes the importance of the dimensionality obvious. For two dimensions, similar to the case of the winding spin chain, there are an infinite amount of classes of Hamiltonians that cannot be continuously transformed into each other. In one and three dimensions, in contrast, all general gapped Hamiltonians are topologically trivial. It is also apparent that once the energy gap closes, the mapping is to a different target space and the classification is no longer valid, similarly to allowing the spins to rotate out of the plane. This implies that phase transitions between different topological phases require a gap closing somewhere in the Brillouin zone.

5.2 Role of symmetries

Another key ingredient when discussing topological phases are the symmetries of the Hamiltonian, as they can constrain the mapping to a different target space and thereby alter the topological classification. Hamiltonians belonging to different topological phases can then not be transformed into each other by a continuous transformation that obeys the symmetry, giving rise to the name symmetry-protected topological phases. Following Bernevig and Neupert [99], the example of a gapped Hamiltonian with an additional chiral symmetry can illustrate how the mappings are constrained. If the Hamiltonian $\hat{h}(\boldsymbol{k})$ commutes with the chiral symmetry operator $\hat{C}$, the spectrum must be symmetric and consists of $N = 2n$ bands with the gap in the middle. The flat band Hamiltonian $\hat{\tilde{h}}(\boldsymbol{k})$ can be expressed in the eigenbasis of the chiral symmetry operator C as

$$\hat{\tilde{h}}(\boldsymbol{k}) = \begin{pmatrix} 0 & \hat{q}(\boldsymbol{k}) \\ \hat{q}^\dagger(\boldsymbol{k}) & 0 \end{pmatrix}. \tag{5.5}$$

From the flat band form we get that $\hat{\tilde{h}}(\boldsymbol{k})^2 = \mathbb{1}$, implying that $\hat{q}(\boldsymbol{k})$ can be any arbitrary unitary matrix, which defines the mapping

$$\hat{q} : T^d \to U(n). \tag{5.6}$$

AZ class	TRS	PHS	C	1D	2D	3D
A	0	0	0	0	$\mathbb{Z}$	0
AIII	0	0	1	$\mathbb{Z}$	0	$\mathbb{Z}$
AI	1	0	0	0	0	0
BDI	1	1	1	$\mathbb{Z}$	0	0
D	0	1	0	$\mathbb{Z}_2$	$\mathbb{Z}$	0
DIII	-1	1	1	$\mathbb{Z}_2$	$\mathbb{Z}_2$	$\mathbb{Z}$
AII	-1	0	0	0	$\mathbb{Z}_2$	$\mathbb{Z}_2$
CII	-1	-1	1	$2\mathbb{Z}$	0	$\mathbb{Z}_2$
C	0	-1	0	0	$2\mathbb{Z}$	0
CI	1	-1	1	0	0	$2\mathbb{Z}$

Table 5.1. *The periodic table of topological insulators and superconductors for up to three dimensions. The first row specifies the Altland-Zirnbauer class, which is defined by the square of the operators implementing the time-reversal (TRS), particle-hole (PHS), and chiral (C) symmetry, respectively, presented in the next three columns. Finally, the group structure of the topological phases in 1, 2, and 3 spatial dimensions are given.*

The homotopy group $\pi_d(U(n))$ classifying this mapping now gives for three dimensions $\pi_3(U(n)) = \mathbb{Z}$ [99]. Gapped Hamiltonians obeying (only) a chiral symmetry can therefore be topologically nontrivial in three dimensions, while all gapped Hamiltonians without it cannot.

The example of the chiral symmetry can similarly be extended to include the other non spatial symmetries discussed in Sec. 4.2, giving rise to the so-called periodic table of topological insulators and superconductors [11, 103, 104, 12]. This table, shown in Tab. 5.1, lists the different topological classes a Hamiltonian obeying certain symmetries can have in certain dimensions. Based on the behavior under time-reversal, particle-hole, and chiral symmetry, the Hamiltonian can be part of one of ten Altland-Zirnbauer (AZ) classes [105, 11, 104]. The behavior under the symmetries is specified by the square of the operator implementing the symmetry, which is ± 1. The examples discussed above belong to the class A (no symmetries) and AIII (only a chiral symmetry).

Of particular interest for superconductors are the classes with particle-hole symmetry. Given that the particle-hole symmetry introduced through the Nambu spinors squares to $+1$ as detailed in Sec. 4.2.2, superconductors with spinful time-reversal symmetry squaring to -1 belong to class DIII. A time-reversal breaking superconductor is a member of class D, and will, for example, always be topologically trivial in 3D. When a superconductor possesses an additional $SU(2)$ spin symmetry, a rotation around the x or y axis in spin space can be formulated as a particle-hole transformation which squares to -1. The classes

in the periodic table with such a particle-hole symmetry are then C and CI for systems without and with time-reversal symmetry, respectively [11].

In addition to the general symmetries such as time-reversal, particle-hole or chiral symmetry, the presence of spatial symmetries also influences which topological invariants can be used to classify the system [12]. Writing the Hamiltonian in a block diagonal form corresponding to the eigenspaces of the point group symmetry, as introduced in Sec. 4.2.4, allows to perform a classification of each individual block. The general symmetries such as TRS and PHS can then either act within each of the blocks, or relate different eigenspaces to each other. The new block Hamiltonian can thus belong to a different symmetry class than the whole Hamiltonian. The resulting topological classification is then said to be protected by the crystalline symmetry. As the decomposition is only possible for values k_0 that are invariant under the point group symmetry, some of the invariants are only defined on the subplanes of the Brillouin zone that are invariant under the symmetry operation.

So far, the topological classification has relied on fully gapped Hamiltonians, however, several of the superconducting states discussed in the papers in this thesis are nodal. While this rules out bulk topological phases, the nodes themselves can be topologically protected [12]. The corresponding mappings are then performed on gapped surfaces enclosing the nodes, which are of lower dimension than the Brillouin zone. For a nodal point in 3D, this would be a sphere, while a nodal line in 3D can be enclosed by a circle. Topologically protected nodes always appear in pairs, such that the sum of their invariants gives zero, and can thus be gapped out by hybridization with each other. Nodes where the partners are mapped onto each other by the symmetries of the Hamiltonian are then classified differently from nodes that are mapped onto themselves by those symmetries. Another difference in the classification is whether the nodes appear at arbitrary positions of the Brillouin zone, when they are not protected by symmetry and also called accidental nodes, or on high symmetry lines or planes, when they are protected by symmetries. Accidental nodes can be classified according to the periodic table up to a dimensional shift corresponding to the reduced dimension of the enclosing space and depending on the behavior under the non-spatial symmetries [12]. The classification of nodes protected by spatial symmetries also proceeds analogously to the gapless phases protected by spatial symmetries, where invariants are only defined for the symmetry eigensectors of the Hamiltonian and on the high symmetric lines and planes [12].

5.3 Introducing topological invariants

Using the periodic table it is possible to determine how many different topological phases a Hamiltonian with certain symmetries can have. However, it contains no information whether a given Hamiltonian actually is topologically

nontrivial or not. This can be determined by calculating the corresponding topological invariant labeling the different phases.

As illustrated in the example of the spin chains in Sec. 5.1, the topological classification is based on some global properties (the winding) of the physical system made up of local degrees of freedom (the spins). This mirrors the mathematical distinction between topology, which is the global structure, and geometry, which denotes the local makeup of objects [99]. The two are linked by the Gauss-Bonnet theorem in differential geometry,

$$2 - 2g = \frac{1}{2\pi} \int_M \mathrm{d}^2 x \, F(x), \qquad (5.7)$$

which states that the integral over the Gaussian curvature $F(x)$ of a 2D Riemannian manifold M with boundary is integer and a topological invariant. The global topological property is given by the genus of the manifold g, which is $g = 0$ for a sphere and $g = 1$ for a torus. The local geometrical information is contained in the Gaussian curvature $F(x)$, which is a measure of how much a tangent vector to the plane is changed along an infinitesimal loop on M.

A similar concept can be constructed for a fully-gapped Hamiltonian defined in reciprocal space $\hat{h}(\boldsymbol{k})$ [9]. Diagonalization of the Hamiltonian yields the eigenenergies $E_{n,\boldsymbol{k}}$ and eigenvectors $|u_{n,\boldsymbol{k}}\rangle$ obeying the relation

$$\hat{h}(\boldsymbol{k}) |u_{n,\boldsymbol{k}}\rangle = E_{n,\boldsymbol{k}} |u_{n,\boldsymbol{k}}\rangle. \qquad (5.8)$$

where the eigenvectors and -states are considered functions of the parameter $\boldsymbol{k}$. They correspond to the tangent vectors on the manifold. Changing the parameter $\boldsymbol{k}$, i.e. going along some path in reciprocal space, the Berry connection of band n

$$\mathcal{A}_{\boldsymbol{k}}^{(n)} = \langle u_{n,\boldsymbol{k}} | \partial_{\boldsymbol{k}} u_{n,\boldsymbol{k}} \rangle \qquad (5.9)$$

measures a change of the wave function along such a path. It is well defined, as long as the band is non-degenerate. Equation 5.8 leaves a gauge freedom in the definition of the wave function

$$|u_{n,\boldsymbol{k}}\rangle \to \mathrm{e}^{\mathrm{i}\phi_{n,\boldsymbol{k}}} |u_{n,\boldsymbol{k}}\rangle, \qquad (5.10)$$

which requires that the Berry connection transforms as

$$\mathcal{A}_{\boldsymbol{k}}^{(n)} \to \mathcal{A}_{\boldsymbol{k}}^{(n)} - \partial_{\boldsymbol{k}} \phi_{n,\boldsymbol{k}}. \qquad (5.11)$$

This implies that the Berry connection cannot be a physical quantity, since it is not gauge invariant. A gauge invariant expression constructed from the connection is the Berry curvature, or field strength

$$\mathcal{F}_{\boldsymbol{k},i,j}^{(n)} = \partial_{k_i} \mathcal{A}_{\boldsymbol{k},j}^{(n)} - \partial_{k_j} \mathcal{A}_{\boldsymbol{k},i}^{(n)}. \qquad (5.12)$$

The Berry connection measures the change of the eigenstates along a closed infinitesimal path, similar to the Gaussian curvature in differential geometry. A physical interpretation is that the Berry connections acts like a vector potential, hence also the label $\mathcal{A}$. The Berry curvature corresponds then to the curl of the Berry connection, which makes it similar to a magnetic field.

A second gauge invariant quantity that can be defined is the Berry phase γ. It is given by a line integral along a closed contour in momentum space.

$$\gamma(\mathcal{C}) = \arg\left(e^{-\oint_{\mathcal{C}} d\boldsymbol{k} \cdot \mathcal{A}_{\boldsymbol{k}}^{(n)}} \right). \tag{5.13}$$

Under a gauge transformation the Berry connection still transforms as detailed in Eq. 5.11. However, an integration over $\partial_{\boldsymbol{k}} \phi_{n,\boldsymbol{k}}$ along a closed path gives an integer multiple of 2π, such that the Berry phase is indeed gauge invariant.

Even though the Berry curvature and Berry phase are gauge invariant, they are not in general quantized, but can take also non-integer values. They are thus not suited as topological invariants. However, topological invariants can be constructed from integrals over these quantities, just like from the integral over the Gaussian curvature, or by introducing additional symmetries. The most important invariant constructed like this is the Chern number of a band in 2D

$$C_n = \frac{i}{2\pi} \int_{BZ} dk_x dk_y \mathcal{F}_{\boldsymbol{k},x,y}^{(n)}. \tag{5.14}$$

It is possible to ascertain that the Chern number indeed takes integer values [9]. If the Berry connection has no singularity in the first Brillouin zone, then the integral vanishes. If there is a point $\boldsymbol{k}_0$, where $\mathcal{A}_{\boldsymbol{k}}^{(n)}$ has a singularity, a gauge transformation according to Eq. 5.11 can be performed in the region R that contains $\boldsymbol{k}_0$ to remove the singularity from that region. The integral over the Brillouin zone can then be translated into a contour integral along the boundary ∂R of the region R with the help of Stokes' theorem to give

$$C_n = \frac{i}{2\pi} \int_{\partial R} d\boldsymbol{k} \cdot \partial_{\boldsymbol{k}} \phi_{n,\boldsymbol{k}}. \tag{5.15}$$

Again, the closed contour integral yields $2\pi N$, such that the Chern number in 2D indeed is an integer number $N \in \mathbb{Z}$. For several occupied bands, it is thus useful to evaluate the Chern number for all occupied bands $C = \sum_{E_n < 0} C_n$.

Even though no additional symmetries were assumed in this discussion, the results hold for superconductors with particle-hole symmetry in 2D, i.e. classes D and C. If the superconductor also obeys time-reversal symmetry, the Berry connection and curvature of the occupied bands transform as

$$\sum_{E_n < 0} \mathcal{A}_{\boldsymbol{k}}^{(n)} \to \sum_{E_n < 0} \mathcal{A}_{-\boldsymbol{k}}^{(n)} \tag{5.16}$$

$$\sum_{E_n < 0} \mathcal{F}_{\boldsymbol{k},i,j}^{(n)} \to \sum_{E_n < 0} -\mathcal{F}_{-\boldsymbol{k},i,j}^{(n)}, \tag{5.17}$$

which is in line with the interpretation in terms of vector potential and magnetic field, respectively. This in turn implies for the Chern number

$$C = \frac{i}{2\pi} \sum_{E_n < 0} \int_{BZ} dk_x dk_y \mathcal{F}_{\boldsymbol{k},x,y}^{(n)}$$
$$= -\frac{i}{2\pi} \sum_{E_n < 0} \int_{BZ} dk_x dk_y \mathcal{F}_{-\boldsymbol{k},x,y}^{(n)} = -C, \qquad (5.18)$$

which necessarily requires $C = 0$. Thus, time-reversal needs to be broken to have a non-zero Chern number in 2D. However, the presence of time-reversal symmetry allows to define another topological invariant instead, the $\mathbb{Z}_2$ invariant. The definition introduced here is based on the Kramers degeneracy and follows the presentation by Sato and Ando [9, 106]. For a time-reversal symmetric Hamiltonian, each eigenstate $|u_{n,\boldsymbol{k}}^I\rangle$ has a Kramers partner $|u_{n,\boldsymbol{k}}^{II}\rangle$. They are related by the time-reversal operation $\mathcal{T}$ via

$$|u_{n,\boldsymbol{k}}^I\rangle = e^{i\phi_{n,\boldsymbol{k}}} \mathcal{T} |u_{n,-\boldsymbol{k}}^{II}\rangle. \qquad (5.19)$$

It is then possible to define a Berry connection of the occupied states for each of the two Kramers partners,

$$\mathcal{A}_{\boldsymbol{k}}^I = \sum_{E_n < 0} \langle u_{n,\boldsymbol{k}}^I | \partial_{\boldsymbol{k}} u_{n,\boldsymbol{k}}^I \rangle \qquad (5.20)$$

$$\mathcal{A}_{\boldsymbol{k}}^{II} = \sum_{E_n < 0} \langle u_{n,\boldsymbol{k}}^{II} | \partial_{\boldsymbol{k}} u_{n,\boldsymbol{k}}^{II} \rangle. \qquad (5.21)$$

Similar to the general case, the Chern number for each of the Kramers partners is then given by

$$C^{I/II} = \frac{i}{2\pi} \sum_{E_n < 0} \int_{BZ} dk_x dk_y \mathcal{F}_{x,y,\boldsymbol{k}}^{I/II}, \qquad (5.22)$$

where the definition of the Berry curvature of the Kramers partners $\mathcal{F}_{x,y,\boldsymbol{k}}^{I/II}$ follows straightforwardly from Eq. 5.12. Each of the two Kramers partner Chern numbers takes an integer value, but since the sum of the Chern numbers of the two Kramers pairs $C^I + C^{II} = C$ must be zero, it also holds $C^I = -C^{II}$. Now the definition of the two Kramers partners is in general not unique, since there is no a priori distinction between the two Kramers partners. It is therefore not possible to use $C^{I/II}$ as a topological invariant. However, the parity $(-1)^{C^{I/II}}$ is well-defined, since both Kramers partner Chern numbers are the same up to a minus sign. This introduces a $\mathbb{Z}_2$ invariant in 2D classifying superconductors in class DIII.

Another $\mathbb{Z}_2$ index can be introduced for a 1D superconductor without time-reversal symmetry [107, 9]. Starting again from the eigenstates of the Hamiltonian $|u_{n,k}\rangle$ with eigenvalue $E_{n,k} > 0$, PHS dictates that $\mathcal{C} |u_{n,-k}\rangle$ is also an

eigenstate with eigenvalue $E_{n,-k} < 0$. Labeling the positive (negative) eigenstates by a positive (negative) integer allows to write the action of particle-hole symmetry as

$$|u_{n,k}\rangle = \mathcal{C}\,|u_{-n,-k}\rangle\,. \tag{5.23}$$

The $\mathbb{Z}_2$ index is based on the Berry connections of the positive and negative bands

$$\mathcal{A}_k^{(+)} = \sum_{n>0} \langle u_{n,k}|\partial_k u_{n,k}\rangle \tag{5.24}$$

$$\mathcal{A}_k^{(-)} = \sum_{n<0} \langle u_{n,k}|\partial_k u_{n,k}\rangle\,, \tag{5.25}$$

and their sum $\mathcal{A}_k = \mathcal{A}_k^{(+)} + \mathcal{A}_k^{(-)}$. They are related by the particle-hole symmetry through

$$\mathcal{A}_k^{(+)} = \mathcal{A}_{-k}^{(-)}\,. \tag{5.26}$$

Representing the eigenvectors $|u_{n,k}\rangle$ in a matrix $\hat{U}(k)$, the Berry connection takes on the form

$$\begin{aligned}
\mathcal{A}_k &= \sum_n \langle u_{n,k}|\partial_k u_{n,k}\rangle \\
&= \mathrm{Tr}\left[\hat{U}(k)^\dagger \partial_k \hat{U}(k)\right] \\
&= \partial_k \left(\ln\det\hat{U}(k)\right)\,.
\end{aligned} \tag{5.27}$$

The Berry phase obtained from the occupied bands along the 1D Brillouin zone is then given by

$$\begin{aligned}
\gamma &= \int_{-\pi}^{\pi} \mathrm{d}k\, \mathcal{A}_k^{(-)} \\
&= \frac{1}{2} \int_{-\pi}^{\pi} \mathrm{d}k\, \mathcal{A}_k \\
&= \frac{1}{2} \int_{-\pi}^{\pi} \mathrm{d}k\, \partial_k \left(\ln\det\hat{U}(k)\right) \\
&= -\frac{1}{2}\theta\Big|_{-\pi}^{\pi}\,,
\end{aligned} \tag{5.28}$$

where θ is the phase angle of $\det\hat{U}(k)$, which is 2π-periodic in k. Consequently the Berry phase is quantized as $e^{i\gamma} = e^{i\pi N} = \pm 1$, defining the 1D $\mathbb{Z}_2$ index for class D. The addition of time-reversal symmetry trivializes this index, but using again the Kramers degeneracy of the occupied bands, it is possible to define a new 1D $\mathbb{Z}_2$ topological invariant for class DIII based on the Berry phase of one of the Kramers partners [9].

5.4 How to calculate topological invariants

While the equations given in the previous section are useful to define the different topological invariants, it is hard to use the definitions to calculate the actual invariant numerically. That is because of difficulties stemming from a discretized Brillouin zone, like defining a phase of the numerically evaluated eigenvalues, and continuously identifying the Kramers partners. To determine the topological invariants in the papers making up this thesis, we instead apply several different approaches suited for numerical purposes.

In Papers I and II, the Chern number is evaluated by a method based on a lattice field strength [108]. Introducing a discretized 2D Brillouin zone of $N_x \times N_y$ discrete points $\boldsymbol{k}_i = (k_{ix}, k_{iy})$, regularly spaced by $\boldsymbol{\delta}_x$ and $\boldsymbol{\delta}_y$, respectively, one can define a link variable from the eigenstates $|u_{n,\boldsymbol{k}_i}\rangle$:

$$U_j(\boldsymbol{k}_i) = \frac{\langle u_{n,\boldsymbol{k}_i} | u_{n,\boldsymbol{k}_i + \boldsymbol{\delta}_j} \rangle}{|\langle u_{n,\boldsymbol{k}_i} | u_{n,\boldsymbol{k}_i + \boldsymbol{\delta}_j} \rangle|}. \tag{5.29}$$

A possible singularity of the link variable at $|\langle u_{n,\boldsymbol{k}_i} | u_{n,\boldsymbol{k}_i + \boldsymbol{\delta}_j} \rangle| = 0$ can always be avoided by a small shift of the Brillouin zone grid. The lattice field strength is then given by

$$\tilde{F}_{12}(\boldsymbol{k}_i) = \ln\left(U_x(\boldsymbol{k}_i) U_y(\boldsymbol{k}_i + \boldsymbol{\delta}x) U_x^{-1}(\boldsymbol{k}_i + \boldsymbol{\delta}y) U_y^{-1}(\boldsymbol{k}_i)\right). \tag{5.30}$$

As the lattice field strength combines bra- and ket-vectors at the same point, it is invariant under the random phases appearing during numerical diagonalization. The Chern number of the n-th band is then the sum of the lattice field strength over the discretized Brillouin zone

$$\tilde{C}_n = \frac{1}{2\pi i} \sum_i \tilde{F}_{12}(\boldsymbol{k}_i). \tag{5.31}$$

This discretized Chern number converges to the continuum version in the limit of $N_x \times N_y \to \infty$ and requires a relatively small number of points in practical applications.

A similar algorithm can be used to calculate the 2D $\mathbb{Z}_2$ index [109]. However, there also exists a simple theorem about odd-parity superconductors that allows to make statements about the topology of the superconducting state based on the Fermi surface of the normal state [35, 110, 111]. The relevant statement, used for the 2D $\mathbb{Z}_2$ invariant in class DIII in Paper II, is: *A weak coupling, odd-parity, time-reversal invariant superconductor has a nontrivial $\mathbb{Z}_2$ index in 2D, if the normal state Fermi surface encloses an odd number of time-reversal invariant momenta (TRIM)* [110, 9]. The TRIM points are defined as those $\boldsymbol{k}$-points $\boldsymbol{\Gamma}_i$ that satisfy $\boldsymbol{\Gamma}_i = -\boldsymbol{\Gamma}_i + \boldsymbol{G}$, where $\boldsymbol{G}$ is a reciprocal lattice vector. Similar statements can be made for time-reversal breaking superconductors and all dimensions $d = 1, 2, 3$ [110, 111, 9]. The theorems make use of the parity eigenvalues of the normal state Hamiltonian. This approach

can be extended to include other symmetries, which allows to determine the topology from so-called symmetry indicators [112, 113, 114, 115].

Finally, we evaluate 1D Berry phases using a numerical discretization of the Wilson loop operator in Papers III and V. The Wilson loop generalizes the integral over the Berry connection to the case of multiple occupied bands M with possible degeneracies [102]. It is defined as the path ordered matrix exponential

$$\mathcal{W}[\mathcal{C}] = \mathcal{P}e^{-\int_{\mathcal{C}} d\boldsymbol{k} \cdot \mathcal{A}_{\boldsymbol{k}}} \tag{5.32}$$

over the non-Abelian Berry connection

$$(\mathcal{A}_{\boldsymbol{k}})_{mn} = \langle u_{m,\boldsymbol{k}} | \partial_{\boldsymbol{k}} | u_{n,\boldsymbol{k}} \rangle, \tag{5.33}$$

where $m, n = 1, \ldots, M$ run over the occupied bands. The path ordering operator $\mathcal{P}$ ensures that operators at the beginning of the path occur to the right. I will reproduce how the Wilson loop can be evaluated numerically by discretizing the path $\mathcal{C}$ into L momenta $\boldsymbol{k}_i, i = 1, \ldots, L$, as shown by Neupert and Schindler [102]. Choosing a closed loop, $\boldsymbol{k}_1 = \boldsymbol{k}_{L+1}$, the integral can be replaced by the product

$$\tilde{\mathcal{W}}_{n_{L+1},n_1}[\mathcal{C}] = \sum_{n_2,\ldots,n_L=1}^{M} \prod_{i=L}^{1} \left(\exp(-(\boldsymbol{k}_{i+1} - \boldsymbol{k}_i) \cdot \mathcal{A}_{\boldsymbol{k}_{i+1}}) \right)_{n_{i+1},n_i}. \tag{5.34}$$

Expanding the exponential to first order

$$\tilde{\mathcal{W}}_{n_{L+1},n_1}[\mathcal{C}] = \sum_{n_2,\ldots,n_L=1}^{M} \prod_{i=L}^{1} \left(\delta_{n_{i+1},n_i} - (\boldsymbol{k}_{i+1} - \boldsymbol{k}_i) \cdot \left(\mathcal{A}_{\boldsymbol{k}_{i+1}} \right)_{n_{i+1},n_i} \right),$$
$$= \sum_{n_2,\ldots,n_L=1}^{M} \prod_{i=L}^{1} \left(\langle u_{n_{i+1},\boldsymbol{k}_{i+1}} | u_{n_i,\boldsymbol{k}_{i+1}} \rangle - (\boldsymbol{k}_{i+1} - \boldsymbol{k}_i) \langle u_{n_{i+1},\boldsymbol{k}_{i+1}} | \partial_{\boldsymbol{k}} | u_{n_i,\boldsymbol{k}_{i+1}} \rangle \right), \tag{5.35}$$

and using the definition of the derivative gives

$$\tilde{\mathcal{W}}_{n_{L+1},n_1}[\mathcal{C}] = \langle u_{n_1,\boldsymbol{k}_1} | \prod_{i=L}^{2} \left(\sum_{n_i=1}^{M} | u_{n_i,\boldsymbol{k}_i} \rangle \langle u_{n_i,\boldsymbol{k}_i} | \right) | u_{n_1,\boldsymbol{k}_1} \rangle, \tag{5.36}$$

which can be simplified to the matrix form

$$\tilde{\mathcal{W}}[\mathcal{C}] = \prod_{i=1}^{L} \hat{U}_{occ}^{\dagger}(\boldsymbol{k}_{i+1}) \cdot \hat{U}_{occ}(\boldsymbol{k}_i), \tag{5.37}$$

where $\hat{U}_{occ}(\boldsymbol{k})$ is the column matrix containing the eigenvectors of the occupied bands. As each matrix is always multiplied by its Hermitian conjugate, the random phases obtained during numerical evaluation vanish, which allows for efficient numerical computation of the Wilson loop. The total Berry phase of the occupied bands is then obtained from [116]

$$\gamma(\mathcal{C}) = \arg(\det \mathcal{W}[\mathcal{C}]). \tag{5.38}$$

5.5 Bulk-boundary correspondence and Majorana fermions

When a gapped Hamiltonian is classified by a non-trivial topological invariant, it cannot be smoothly transformed into a different topological phase. A special case of this argument happens when two systems with different topological invariants are put side by side, such that one can continuously move from one to the other. A particular example of this is a boundary between a topological superconductor and the vacuum, which is topologically trivial. Transforming a gapped Hamiltonian from one topological phase to another by some parameter requires that the band gap closes, as discussed in Sec. 5.1. Using the position as this parameter, a boundary between two systems of different topological invariants, that respects the protecting symmetry, in general has to yield a gap closing somewhere in between. This means that a boundary between a topological superconductor and the vacuum also guarantees the existence of a state crossing the gap. This principle is called bulk-boundary correspondence and yields some of the most important physical implications of the study of topology in condensed matter. It allows to study the topology of a system, which is a rather theoretical and abstract concept, through the appearance of gapless states on the surface. In fact, the number of surface states is equal to the difference of the topological indices [117]. For a boundary to the topologically trivial vacuum, the number of surface modes is therefore given by the topological invariant.

In topological superconductors, the excitations appearing in such gap closings can be realizations of Majorana fermions. Two conditions need to be satisfied [9]: The excitation needs to be described by the Dirac equation and it needs to be its own antiparticle,

$$\gamma^{\dagger} = \gamma. \tag{5.39}$$

Both conditions can be met in topological superconductors. As the boundary states appear from a band crossing, its low-energy Hamiltonian can be naturally expressed in terms of a massless Dirac equation in terms of band indices. And based on the expressions derived in Chapter 3, the Bogoliubov quasiparticles at zero energy are equal superpositions of particles and holes, which are transformed into each other under conjugation. However, not all zero energy Bogoliubov quasiparticles fulfill Eq. (5.39). The excitation needs to be non-degenerate to be mapped onto itself and spatially well-separated from other Majorana states. Nevertheless, all these conditions can be fulfilled for example in spinless 2D $p_x + i p_y$ superconductors [118], or 1D p-wave superconductors [119], and possible experimental signatures of Majorana quasiparticles have been detected [120]. In addition to the general interest in realizing Majorana quasiparticles, they have also been proposed as building blocks for quantum computation, since they exhibit non-trivial statistics [121, 10, 9,

122]. This yields a strong technological motivation to explore topological superconductors and to find new materials hosting Majoranas.

5.6 Twist states between $d \pm \mathrm{i}d'$ regions on the harmonic honeycomb lattices

In the following sections, I discuss the topological classification of the order parameters obtained on the different Kitaev materials, beginning with the large harmonic honeycomb lattices discussed in Paper I. When the honeycomb regions in between twists are large enough to approximately restore the six-fold rotational symmetry, the $d \pm \mathrm{i}d'$ superconducting state is stable in the harmonic honeycomb lattices. On a single graphene layer, the $d \pm \mathrm{i}d'$ superconducting state belongs to AZ class C, characterized by a broken time-reversal symmetry and $SU(2)$ spin rotation, as detailed in Sec. 5.2. It is therefore characterized by even Chern numbers. Indeed, the $d \pm \mathrm{i}d'$ is known to be yield a Chern number of ± 2, due to the winding of the superconducting order parameter. All edges should therefore host a pair of co-propagating, or chiral, edge states [117, 100]. In the large harmonic honeycomb lattices, which are actually 3D structures, the honeycomb sheets can be approximated as stacks of 2D layers, which should lead to the appearance of edge states. And indeed, the local density of states (LDOS) of a harmonic honeycomb with a single twist in the center shown in Figure 5.2 as a function of position features states appearing on the edges and at the twist. The edge states on the open outer boundaries behave as expected, but there are also subgap states visible at the twist, independently of the chiralities of the two joined regions. This can be motivated by the fact, that the twist connects two quasi 2D regions with different spatial orientations only in isolated points. As the $d \pm \mathrm{i}d'$ state is characterized by a Chern number of ± 2, there should be in total eight chiral edge states for such a slab with a single twist: two appearing at the left edge, two to the left and two to the right of twist, and two more at the right edge. Figure 5.3 displays the dispersion of the edge states along two cuts parallel to one of the reciprocal lattice vectors of the Brillouin zone shown in the inset. For both cuts there are four states crossing the gap. Two of them are the same for both parallel cuts, meaning that they only disperse along the edges corresponding to the direction of the cut. They must be located at the left outer edge. The corresponding edge states from the right outer edge should then not disperse along the cut, which means the horizontal line in the black spectrum is one of these edge states. The remaining states on the twist, however, have the possibility to hybridize and therefore disperse in both $\boldsymbol{k}$-space directions, forming a 2D band localized at the twist. These are the two states crossing the gap that change between the two cuts.

In summary, the twist acts similar to an outer edge of the 2D honeycomb sheets, without enforcing a preference on the chirality of the two regions
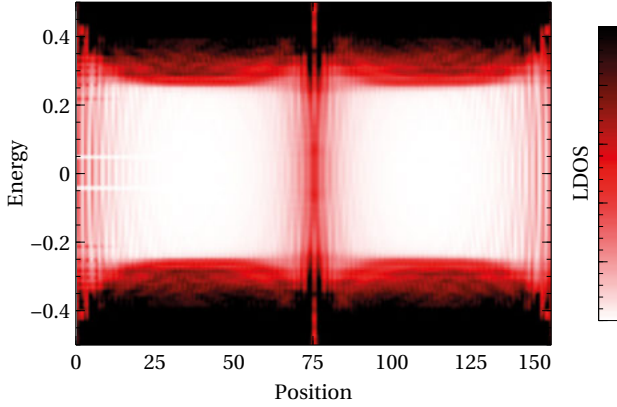
Figure 5.2. Local density of states as a function of position for an isolated twist in the in the center of a 150 sites long slab with open boundary conditions. The high densities shown in red and black reveal the existence of edge states near the open outer boundaries and along the twist that appear within the superconducting gap. Figure taken from Paper I.

joined at the twist. The four chiral edge states appearing at the twist are allowed to hybridize such that they form 2D bands localized to the twist, clearly different from regular 1D zigzag edges.

5.7 A multitude of topological phases from the extended Kitaev-Heisenberg interaction

The extended Kitaev-Heisenberg model on the 2D honeycomb lattice hosts several different superconducting phases, as discussed in Sec. 4.5. Here I present the relevant topological classification for those phases, beginning with the time-reversal symmetry breaking phase d_{chiral}. As time-reversal is broken, the only remaining non-spatial symmetry is particle-hole symmetry, which in the absence of $SU(2)$ symmetry squares to $+1$. The chiral state therefore belongs to class D in the periodic table and is characterized by a Chern number $C \in \mathbb{Z}$. Using the numerical algorithm for the Chern number discussed in Sec. 5.4, we determine the Chern number of the chiral state to be non-zero throughout the whole region in which the state is found self-consistently. We also determine the Chern number as a function of the order parameter strength $|d|$ for a fixed doping level. As plotted in Fig. 5.4 a), the Chern number evolves as a function of the strength of the order parameter, going from $C = \mp 4$ to $C = \mp 1$ and finally to $C = \pm 2$, where the two signs corresponds to the degenerate chiralities. In between each jump in the Chern number, the band gap closes at the three M points of the first Brillouin zone, explaining the jump
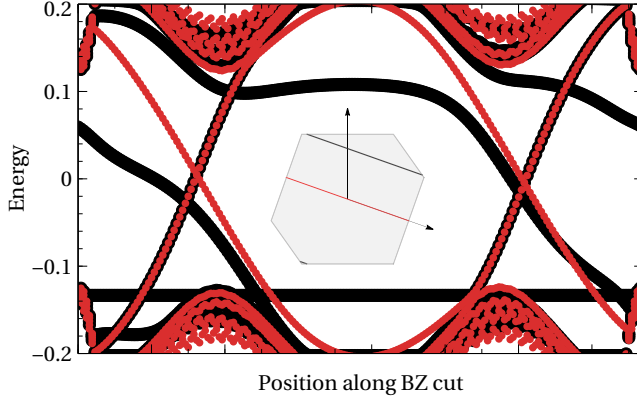
Figure 5.3. Quasiparticle spectrum of a single twist structure evaluated along two parallel cuts through the 2D Brillouin zone formed by the twist region (see inset for cuts). Four gapless states connecting the conduction and valence band appear for both cuts. The edge states along the open outer boundaries do not disperse along the direction perpendicular to the cuts and therefore do not change between them. The 2D band formed by hybridization of the edge states at the twist, however, clearly changes between the cuts. Figure taken from Paper I.
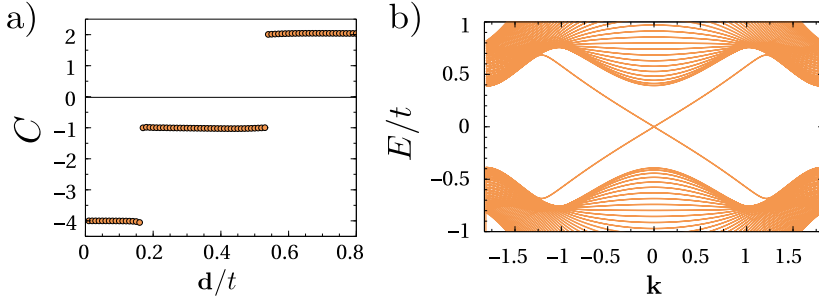
Figure 5.4. Topological properties of the chiral superconducting state d_{chiral} found at intermediate doping levels at $\Gamma < 0$. (a) Chern number C for non-self-consistently determined order parameter strength $|d|$ at doping level $\delta = 0.14$. The topological phase transitions as a function of order parameter strength are clearly visible by the jumps in the Chern number $\Delta C = 3$. (b) Quasiparticle spectrum of a honeycomb lattice with open boundary conditions along the zigzag edges for $|d| = 0.4t$ and $\delta = 0.14$. Each open boundary hosts a chiral mode crossing the band gap. Figure taken from Paper II.

by $\Delta C = 3$. The exact value of the order parameter strength for the topological phase transitions depends on the doping level. For the self-consistently determined solutions at $K = -t$, only the solution with $C = \mp 1$ is realized and the phase transition to the nematic superconducting phase happens simultaneously to the topological phase transition. However, this appears to be a fine-tuned effect, as the two transitions split when using smaller values of K. The finite Chern number of the chiral state should manifest in the appearance of chiral edge states due to the bulk-boundary correspondence. As Fig. 5.4(b) illustrates, the state with $|C| = 1$ indeed produces one chiral mode crossing the band gap on a finite strip with open boundary conditions along the zigzag edge. The same is found for the armchair edge.

The two time-reversal symmetric states $\boldsymbol{d}_{\Gamma > 0}$ and $\boldsymbol{d}_{\text{nematic}}$ found for positive and negative values of the off-diagonal exchange Γ, respectively, are actually topologically equivalent, even though they differ in the symmetry classification. Both states obey the spinful time-reversal symmetry squaring to -1 and the particle-hole symmetry squaring to $+1$. This means they are also chiral symmetric and belong to class DIII, which is characterized by a $\mathbb{Z}_2$ invariant in 2D. Referring to the theorem discussed in Sec. 5.4, the invariant is trivial for low doping, when the Fermi surface encloses the K and K' points of the Brillouin zone [33]. When the doping exceeds $\delta = 0.25$, the Fermi surface undergoes a Lifshitz transition and now forms a circle around the Γ point. This means only a single TRIM point is enclosed by the normal state Fermi surface and the $\mathbb{Z}_2$ index is then non-trivial, as long as the state is continuously connected to a weak pairing state as shown by Hyart et al. [33]. Below this critical doping, both states actually belong to a topological phase protected by a spin rotation [68]. Using this symmetry, the Hamiltonian can be block diagonalized into the form

$$\hat{h}(\boldsymbol{k}) = \begin{pmatrix} \hat{h}_\uparrow(\boldsymbol{k}) & 0 \\ 0 & \hat{h}_\downarrow(\boldsymbol{k}) \end{pmatrix}. \tag{5.40}$$

While particle-hole symmetry acts within each block, time-reversal relates the two blocks to each other. Each subblock is thus in class C (characterized by particle-hole symmetry and SU(2) symmetry) and can be classified by an even spin Chern number, which turns out to be nonzero $C_{\uparrow/\downarrow} = \pm 2$. The whole situation changes when including the spin-orbit coupled hopping introduced in Sec. 3.4. The symmetry protecting the spin Chern number is immediately broken for any finite value of t_{SO}, which gaps out the edge states appearing in this phase, as illustrated in Fig. 5.5 a) for parameters deep in the $\boldsymbol{d}_{\Gamma > 0}$ phase. However, the effect of the spin-orbit hopping on the band structure leads to a new topological phase transition into the $\mathbb{Z}_2$ nontrivial phase even below $\delta = 0.25$. Fig. 5.5 b) shows the evolution of the Fermi surface at $\delta = 0.2$ as a function of the spin-orbit hopping strength. The Fermi pockets around the K and K' points at $t_{SO} = 0$ evolve into first a circle enclosing the Γ point and then further into pockets around the three M points. During the first of these two
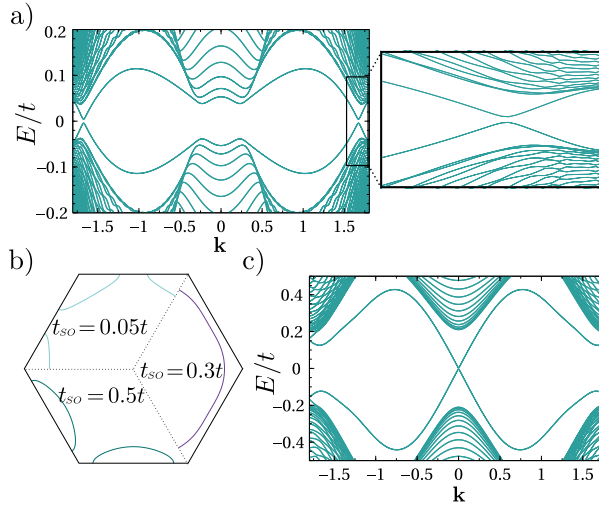
Figure 5.5. The spin-orbit hopping term H_{SO} influences the topological classification of the time-reversal symmetric superconducting states, illustrated by the state $d_{\Gamma>0}$. (a) Quasiparticle spectrum of a zigzag nanoribbon including $t_{SO} = 0.02t$ at $\delta = 0.2$. The edge states no longer cross the gap and are gapped, see zoom-in inset. (b) Normal state Fermi surface for three different values of the spin-orbit hopping plotted within one Brillouin zone. Two Lifshitz transitions occur at constant filling $\delta = 0.2$ when tuning the spin-orbit hopping t_{SO}. (c) Helical edge states visible in the quasiparticle spectrum of $d_{\Gamma>0}$ at $\Gamma = 0.5$, $\delta = 0.2$, and $t_{SO} = 0.3$ are a signature that the system is in a $\mathbb{Z}_2$ non-trivial state driven by t_{SO} even at $\delta < 0.25$. Figure taken from Paper II.

sequential Lifshitz transitions the number of enclosed TRIM points changes from even to odd. Because the order parameter stays the same for all values of t_{SO} along this evolution, the criterion discussed above remains valid and $\boldsymbol{d}_{\Gamma>0}$ is characterized by a non-trivial $\mathbb{Z}_2$ invariant for large enough t_{SO}, even below the threshold of $\delta = 0.25$. This is illustrated by the appearance of a pair of helical edge modes crossing the superconducting gap in Fig. 5.5 c). The same argument can be made for the topologically equivalent $\boldsymbol{d}_{\text{nematic}}$ state.

The superconducting phase diagram of the doped extended Kitaev-Heisenberg interaction on the honeycomb lattice thus features several topological phases. The time-reversal breaking state is characterized by a non-zero Chern number that changes as a function of order parameter strength. The time-reversal symmetric states, regardless of their behavior under the lattice symmetries, feature non-trivial $\mathbb{Z}_2$ indices at large doping or strong spin-orbit coupling or symmetry-protected finite spin Chern numbers at low doping in the absence of spin-orbit coupling. Each topological phase gives rise to a distinct edge spectrum that leaves a specific experimental fingerprint.

5.8 Nodal phases on the hyperhoneycomb lattice

The topological classification of the superconducting phases on the hyperhoneycomb lattice focuses on possible topological protection of the spin triplet nodal phases presented in Paper V and discussed in Sec. 4.6. The classification of the nodes appearing in the spin singlet phases in Paper III is not presented here, because it was carried out by my co-author.

In the absence of spin-orbit coupling, the two spin triplet superconducting phases discussed in Sec. 4.6 feature a pair of line nodes away from high symmetry planes, i.e. accidental nodes, as shown in Fig. 5.6 a). The first step to the topological classification is then to identify the relevant non-spatial symmetries of the Hamiltonian. Each of the nodes is spin degenerate, and the superconducting pairing giving rise to the nodes is of equal spin pairing type ($\boldsymbol{d}_{x/y}$), such that the Hamiltonian is already block diagonalized into spin up and spin down blocks

$$H = \begin{pmatrix} H_\uparrow & 0 \\ 0 & H_\downarrow \end{pmatrix}. \tag{5.41}$$

Each block obeys a spinless time-reversal symmetry squaring to $+1$ and a particle-hole plus $SU(2)$ symmetry, such that the relevant AZ class is class CI. A topological stability of nodal lines in 3D is then inherited from class AIII, because time-reversal does not trivialize it [12, 116]. The classification for each spin block is thus identical to that of the line nodes in the spin singlet superconducting state discussed in Paper III. The nodes are found to be topologically protected by virtue of a Berry phase of π picked up along a loop $\mathcal{L}$ enclosing one of the nodes, as pictured in Fig. 5.6 a), and calculated using the
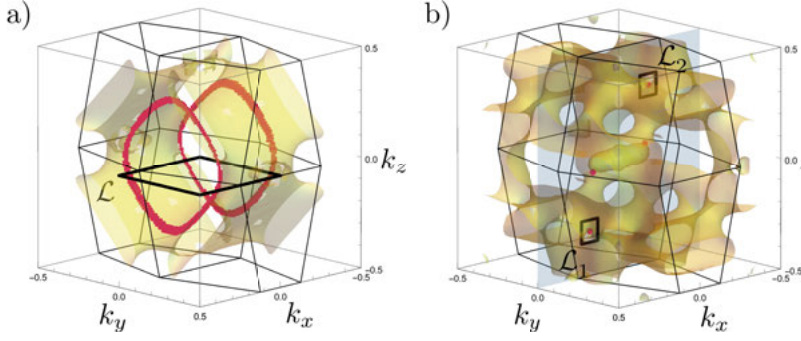
Figure 5.6. Topological classification of the nodes appearing in the spin triplet superconducting states on the hyperhoneycomb lattice. The Fermi surface of each case is shown in opaque yellow and the boundary of the first Brillouin zone is sketched with black lines. a) The pair of nodal lines (red) is protected by spin-symmetry and classified by a non-trivial Berry phase of π along the loop $\mathcal{L}$ circling a node. b) Two of the nodal points (red) on the $k_y = 0$ mirror plane (blue) are protected by the mirror σ_{xz} and the loops $\mathcal{L}_1$ and $\mathcal{L}_2$ surrounding the nodes gives rise to a Berry phase of $\pm\pi$, respectively. The remaining two nodal points are not topologically protected. Figure taken from Paper V.

Wilson loop technique presented in Sec. 5.4. The two nodes are then partners of opposite topological charge, which can annihilate each other. Furthermore, the classification relies on the block diagonalization into spin sectors, which means that any finite spin-orbit coupled hopping or pairing in the equal spin triplet channel lifts the topological protection and should gap out the nodes.

Indeed, in the presence of strong spin-orbit coupled hopping, the superconducting state characterized by $\boldsymbol{d}_{SO}$ features point nodes, as shown in Fig. 5.6 b). In contrast to the point nodal spin singlet state discussed in Sec. 4.4, and Papers I and III, this state preserves time-reversal symmetry and the nodes are therefore not characterized by a non-zero Chern number. Instead, the point nodes occur along the $k_y = 0$ plane of the Brillouin zone, so the nodes are protected by the σ_{xz} mirror symmetry. The symmetry operator acting on the BdG Hamiltonian can be constructed from

$$\hat{\sigma}_{xz} = (1 \rightarrow 3, 2 \rightarrow 4, 3 \rightarrow 1, 4 \rightarrow 2) \otimes \hat{\sigma}_x \otimes \hat{t}_0, \tag{5.42}$$

where $i \rightarrow j$ means that orbital i is mapped onto orbital j due to the non-symmorphic action of the mirror operator, and $\hat{\sigma}_i$ and $\hat{t}_i$ are Pauli matrices acting on spin and particle-hole space, respectively. Using the unitary matrix $\hat{U}_{xz}$ that diagonalizes the mirror operator, the BdG Hamiltonian can be decomposed into a block diagonal form for $k_y = 0$,

$$H = \begin{pmatrix} H_+ & 0 \\ 0 & H_- \end{pmatrix}, \tag{5.43}$$

where each block $\pm$ corresponds to an eigensector of the mirror operator. The classification of the mirror protected point nodes is then in terms of a mirror Chern number according to class DIII with mirror symmetry, and the topological nature of the point nodes can be determined by calculating the Berry phase along a 1D loop in the $k_y = 0$ plane enclosing the nodal points [12]. Fig. 5.6 b) shows the loops $\mathcal{L}_1$ and $\mathcal{L}_2$, enclosing two of the nodal points in the Brillouin zone, which give rise to a non-trivial Berry phase of $\pm\pi$ around them. The remaining two nodes are topologically trivial and can be gapped out by additional terms in the Hamiltonian. The topological nature of the point nodes can also be determined by calculating the Berry phase along a family of loops $\mathcal{L}_\parallel(k_z)$ running parallel to the k_x axis. These loops are closed due to the periodic nature of the Brillouin zone. For $|k_z| < k_z^0$ ($|k_z| > k_z^0$), where $\pm k_z^0$ is the position of the two point nodes, the Berry phase evaluates to 0 (π). This confirms the topological protection and also implies the appearance of Fermi arc states on a (001) surface, that connect the projections of the topologically protected nodal points [12].

The hyperhoneycomb lattice is thus a natural host for topologically protected line and point nodes. Notably, the classification of the line nodes falls into the same topological class for both spin singlet and triplet pairing, while the point nodes are protected by different symmetries.

Part II:
Odd-frequency pairing and the Meissner effect
in doped Bi_2Se_3

6. Odd-frequency superconductivity in doped Bi$_2$Se$_3$

Leaving behind the Kitaev materials, this second part of the thesis focuses on odd-frequency superconductivity in Bi$_2$Se$_3$ and its manifestation in the Meissner effect, as presented in Paper IV. In this chapter, I focus on a general introduction to odd-frequency pairing and its appearance in the nematic or chiral superconducting state of doped Bi$_2$Se$_3$. I begin by presenting the general idea and discussing the possible symmetry classes of odd-frequency pairing, which is based on a symmetry classification of the superconducting pairing correlations, going beyond the superconducting order parameter discussed in the first part of the thesis. Thereafter, I detail how odd-frequency pairing appears ubiquitously in multiorbital superconductors, following the argumentation in a recent review [16]. Thereafter I briefly review previous research on superconductivity in doped Bi$_2$Se$_3$, before the section concludes with a summary of the odd-frequency pairing in this material.

6.1 Symmetry classification of odd-frequency pairing

In addition to the symmetry classification of the superconducting order parameter presented in Chapter 4, a more general analysis of the symmetries of a superconductor can be formulated in terms of the pairing correlations. These are encoded in the anomalous Green's function, which for a generic multiorbital superconductor is given by the time-ordered expectation value

$$F_{\sigma_1\sigma_2, \boldsymbol{r}_1\boldsymbol{r}_2, o_1 o_2}(t_1, t_2) = -\left\langle \mathcal{T} \psi_{\sigma_1, \boldsymbol{r}_1, o_1}(t_1) \psi_{\sigma_2, \boldsymbol{r}_2, o_2}(t_2) \right\rangle, \tag{6.1}$$

where $\mathcal{T}$ is the time-ordering operator and σ_i, $\boldsymbol{r}_i$, o_i, and t_i label the spin, position, orbital, and time degrees of freedom of the two electrons ψ forming a Cooper pair. As the expectation value is made up of fermions, the Pauli exclusion principle restricts the symmetry properties of the anomalous Green's function at equal times $t_1 = t_2$. In particular, it requires that the wave function describing the state of two identical fermions must be odd under exchange of the particles at equal times [19]

$$F_{\sigma_1\sigma_2, \boldsymbol{r}_1\boldsymbol{r}_2, o_1 o_2}(t_1, t_1) = -F_{\sigma_2\sigma_1, \boldsymbol{r}_2\boldsymbol{r}_1, o_2 o_1}(t_1, t_1). \tag{6.2}$$

A key idea behind odd-frequency pairing is to postulate an extension of this to pairing at unequal times [13, 19]. Introducing the generalized parity operators

Parity	1	2	3	4	5	6	7	8
Spin S	-	+	+	-	+	-	-	+
Parity P	+	-	+	-	+	-	+	-
Orbital O	+	+	-	-	+	+	-	-
Time T	+	+	+	+	-	-	-	-

Table 6.1. *Complete list of the eight symmetry classes of the anomalous Green's function obeying Eq. (6.3) required by Fermi statistics. The behaviour under the generalized parity operations S, P, O, and T for spin, position, orbital, and time exchange, respectively, is characterized by the acquired sign $\pm$.*

S, P, O, and T, exchanging spin, position, band, and time coordinates of the two particles, respectively, interchanging the two particles can be considered as a combined exchange of all individual degrees of freedom. The extension of the Pauli principle then requires the combined action

$$SPOTF_{\sigma_1\sigma_2,r_1r_2,o_1o_2}(t_1,t_2) = -F_{\sigma_1\sigma_2,r_1r_2,o_1o_2}(t_1,t_2), \qquad (6.3)$$

which can be symbolically captured by the expression $SPOT = -1$. Considering that the anomalous Green's function can be even or odd under each individual parity operation, there are in total eight combinations that satisfy Eq. (6.3) [15], which are listed in Table 6.1. The first two classes include the cases of single band spin singlet even parity and spin triplet odd parity pairing, respectively, that were already discussed in Sec. 3.1. The four classes $5-8$ that pick up a minus sign under the time exchange operation T,

$$TF_{\sigma_1\sigma_2,r_1r_2,o_1o_2}(t_1,t_2) = -F_{\sigma_1\sigma_2,r_1r_2,o_1o_2}(t_2,t_1), \qquad (6.4)$$

are called odd-frequency (odd-ω) pairing. This constraint immediately requires that the anomalous Green's function vanishes at equal times $t_1 = t_2$.

The nomenclature becomes clearer, if the superconductor described by the anomalous Green's function only depends on the relative position and time coordinates

$$\boldsymbol{r} = \boldsymbol{r}_1 - \boldsymbol{r}_2 \qquad \text{and} \qquad t = t_1 - t_2, \qquad (6.5)$$

and can therefore be Fourier transformed in both coordinates to obtain the frequency dependent anomalous Green's function

$$F_{\sigma_1\sigma_2,\boldsymbol{k},o_1o_2}(\omega) = \int_{-\infty}^{\infty} d\boldsymbol{r}e^{-i\boldsymbol{k}\cdot\boldsymbol{r}} \int_{-\infty}^{\infty} dt e^{-i\omega t} F_{\sigma_1\sigma_2,\boldsymbol{r},o_1o_2}(t). \qquad (6.6)$$

The Pauli principle at equal times $t_1 = t_2$ then corresponds to $t = 0$, dictating

$$\int_{-\infty}^{\infty} d\omega F_{\sigma_1\sigma_2,\boldsymbol{k},o_1o_2}(\omega) = -\int_{-\infty}^{\infty} d\omega F_{\sigma_2\sigma_1,-\boldsymbol{k},o_2o_1}(\omega). \qquad (6.7)$$

This equation is satisfied by either even-frequency correlations obeying

$$F_{\sigma_1\sigma_2,\boldsymbol{k},o_1o_2}(\omega) = -F_{\sigma_2\sigma_1,-\boldsymbol{k},o_2o_1}(\omega) \tag{6.8}$$

or by odd-frequency pairing transforming as

$$F_{\sigma_1\sigma_2,\boldsymbol{k},o_1o_2}(\omega) = -F_{\sigma_2\sigma_1,-\boldsymbol{k},o_2o_1}(-\omega). \tag{6.9}$$

From the definition of the Fourier transform in Eq. (6.6) it is clear that an anomalous Green's function that is odd under the exchange of time T is also odd under the inversion of frequency, motivating the nomenclature. Instead of working with real frequencies, the anomalous Green's functions can be obtained in Matsubara representation, as well. The connection between the two is then made via analytical continuation. It can then be shown that the constraint in Eq. (6.7) yields a similar restriction for the Matsubara Green's functions [19],

$$F_{\sigma_1\sigma_2,o_1o_2}(\boldsymbol{k}, i\omega) = -F_{\sigma_2\sigma_1,o_2o_1}(-\boldsymbol{k}, -i\omega), \tag{6.10}$$

where $i\omega$ are the imaginary Matsubara frequencies.

6.2 Odd-frequency pairing in multiorbital superconductors

Even though odd-frequency superconductivity was first discussed in the context of He^3 [13] and later in terms of an odd-frequency order parameter [123, 124, 125], odd-frequency anomalous Green's functions appear ubiquitously in multiorbital systems described by standard BCS Hamiltonians. This can be illustrated by a simple two-band model [15, 16]

$$H_{\mathrm{MF}} = \frac{1}{2}\sum_{\boldsymbol{k}} \boldsymbol{\Psi}_{\boldsymbol{k}}^\dagger \begin{pmatrix} \hat{h}_0(\boldsymbol{k}) & \hat{\Delta}(\boldsymbol{k}) \\ \hat{\Delta}^\dagger(\boldsymbol{k}) & -\hat{h}_0^*(-\boldsymbol{k}) \end{pmatrix} \boldsymbol{\Psi}_{\boldsymbol{k}}, \tag{6.11}$$

with the Nambu spinor $\boldsymbol{\Psi}_{\boldsymbol{k}} = \left(\boldsymbol{\psi}_{\boldsymbol{k}}, \boldsymbol{\psi}_{-\boldsymbol{k}}^\dagger\right)^T$, where $\boldsymbol{\psi}_{\boldsymbol{k}} = \left(c_{\boldsymbol{k}1\uparrow}, c_{\boldsymbol{k}1\downarrow}, c_{\boldsymbol{k}2\uparrow}, c_{\boldsymbol{k}2\downarrow}\right)^T$, as defined in Sec. 3.2. The normal state and gap function are given by

$$\hat{h}_0(\boldsymbol{k}) = \begin{pmatrix} \xi_1(\boldsymbol{k}) & \Gamma \\ \Gamma^* & \xi_2(\boldsymbol{k}) \end{pmatrix} \otimes \hat{\sigma}_0 \quad \text{and} \quad \hat{\Delta}(\boldsymbol{k}) = \begin{pmatrix} \Delta_1(\boldsymbol{k}) & 0 \\ 0 & \Delta_2(\boldsymbol{k}) \end{pmatrix} \otimes i\hat{\sigma}_y, \tag{6.12}$$

respectively. Here, $\xi_i(\boldsymbol{k})$ is the dispersion of band i, Γ describes a band hybridization and $\Delta_i(\boldsymbol{k})$ is a (spin singlet) superconducting order parameter in band i. ξ and Γ can also be considered in terms of an orbital basis, describing intra- and interorbital processes, respectively.

The anomalous Green's functions containing the information about even and odd-frequency pairing can be obtained from the equation of motion

$$
\begin{pmatrix} i\omega - \hat{h}_0(\boldsymbol{k}) & -\hat{\Delta}(\boldsymbol{k}) \\ -\hat{\Delta}^\dagger(\boldsymbol{k}) & i\omega + \hat{h}_0^*(-\boldsymbol{k}) \end{pmatrix} \cdot \begin{pmatrix} \hat{G}(\boldsymbol{k}, i\omega) & \hat{F}(\boldsymbol{k}, i\omega) \\ \hat{\bar{F}}(\boldsymbol{k}, i\omega) & \hat{\bar{G}}(\boldsymbol{k}, i\omega) \end{pmatrix} = \mathbb{1}, \qquad (6.13)
$$

where $\hat{G}(\boldsymbol{k}, i\omega)$ and $\hat{F}(\boldsymbol{k}, i\omega)$ are the normal and anomalous Matsubara Green's functions, respectively, and a bar marks the corresponding hole Green's function. Assuming an inversion symmetric dispersion, $\xi_i(-\boldsymbol{k}) = \xi_i(\boldsymbol{k})$, and $\Gamma \in \mathbb{R}$, the anomalous Green's function is given by

$$
\hat{F}(i\omega) = \frac{1}{D[\boldsymbol{k}, (i\omega)^2]} i\hat{\sigma}_y \otimes
$$
$$
\begin{pmatrix} \Delta_1\left((i\omega)^2 - E_2^2\right) - \Delta_2\Gamma^2 & \Gamma(-i\omega(\Delta_1 - \Delta_2) + \Delta_1\xi_2 + \Delta_2\xi_1) \\ \Gamma(i\omega(\Delta_1 - \Delta_2) + \Delta_1\xi_2 + \Delta_2\xi_1) & \Delta_2\left((i\omega)^2 - E_1^2\right) - \Delta_1\Gamma^2 \end{pmatrix}.
$$
$$(6.14)$$

The denominator $D\left[(i\omega)^2\right]$ is an even polynomial in the Matsubara frequencies, $E_i = \sqrt{\xi_i^2 + \Delta_i^2}$ is the quasiparticle dispersion, and all momentum dependencies have been suppressed for legibility. While the intraband pairing in $\hat{F}(i\omega)$ is proportional to $(i\omega)^2$ and $(i\omega)^0$ and therefore completely even in frequency, the interband pairing contains the odd-frequency term [15, 16]

$$
\hat{F}_{odd}(\boldsymbol{k}, i\omega) = \frac{i\omega}{D(\boldsymbol{k}, (i\omega)^2)} \Gamma(\Delta_1(\boldsymbol{k}) - \Delta_2(\boldsymbol{k})) i\hat{\tau}_y \otimes i\hat{\sigma}_y, \qquad (6.15)
$$

belonging to class 7 in Tab. 6.1. This simple two-band model thus gives rise to odd-frequency pairing as long as there is a finite interband hybridization Γ and a difference between the two superconducting gaps $\Delta_1 \neq \Delta_2$. Relaxing the condition on the interband hybridization and allowing complex terms $\Gamma = |\Gamma|e^{i\phi}$, the odd-frequency pairing term appears even more generically [21, 16].

A more rigorous result signaling the presence of odd-frequency pairing in multiorbital superconductors, that generalizes the results of the simple two-band model, can be obtained from the generic multiorbital Hamiltonian

$$
H_{\text{MF}} = \frac{1}{2} \sum_{\boldsymbol{k}} \boldsymbol{\Psi}_{\boldsymbol{k}}^\dagger \begin{pmatrix} \hat{h}_0(\boldsymbol{k}) & \hat{\Delta}(\boldsymbol{k}) \\ \hat{\Delta}^\dagger(\boldsymbol{k}) & -\hat{h}_0^*(-\boldsymbol{k}) \end{pmatrix} \boldsymbol{\Psi}_{\boldsymbol{k}}, \qquad (6.16)
$$

where now the multiorbital Nambu spinor $\boldsymbol{\Psi}_{\boldsymbol{k}} = \left(\boldsymbol{\psi}_{\boldsymbol{k}}, \boldsymbol{\psi}_{-\boldsymbol{k}}^\dagger\right)^T$ includes a number of orbitals n, $\boldsymbol{\psi}_{\boldsymbol{k}} = \left(c_{\boldsymbol{k}1\uparrow}, c_{\boldsymbol{k}1\downarrow}, \ldots, c_{\boldsymbol{k}n\uparrow}, c_{\boldsymbol{k}n\downarrow}\right)^T$, and the normal state and gap function contain arbitrary intra- and interorbital terms. Generalizing the equations of motion in Eq. (6.13), the anomalous Green's function can be ob-

tained from [126]

$$\hat{F}(i\omega) = \left(\left(i\omega - \hat{h}_0(\boldsymbol{k})\right) - \hat{\Delta}(\boldsymbol{k}) \left(i\omega + \hat{h}_0^*(-\boldsymbol{k})\right)^{-1} \hat{\Delta}(\boldsymbol{k})^{\dagger} \right)^{-1} \times$$
$$\hat{\Delta}(\boldsymbol{k})(i\omega + \hat{h}_0^*(-\boldsymbol{k}))^{-1}. \tag{6.17}$$

The anomalous Green's function will then generically contain several even- and odd-frequency terms. Linearizing the right hand side in terms of $\hat{\Delta}$, the even- and odd-frequency pair amplitudes are given by [16]

$$\hat{F}_{even}(i\omega) = -\left(\omega^2 + \hat{h}_0(\boldsymbol{k})^2\right)^{-1} \times$$
$$\left(\left[\hat{h}_0(\boldsymbol{k}), \hat{\Delta}(\boldsymbol{k})\right]^* \hat{h}_0^*(-\boldsymbol{k}) \left(\omega^2 + \hat{h}_0^*(-\boldsymbol{k})^2\right)^{-1} - \hat{\Delta}(\boldsymbol{k}) \right), \quad (6.18)$$
$$\hat{F}_{odd}(i\omega) = i\omega \left(\omega^2 + \hat{h}_0(\boldsymbol{k})^2\right)^{-1} \left[\hat{h}_0(\boldsymbol{k}), \hat{\Delta}(\boldsymbol{k})\right]^* \left(\omega^2 + \hat{h}_0^*(-\boldsymbol{k})^2\right)^{-1}, \quad (6.19)$$

where $\left[\hat{h}_0(\boldsymbol{k}), \hat{\Delta}(\boldsymbol{k})\right]^*$ has been defined as the superconducting fitness $\hat{F}_C i \hat{\sigma}_y$ in Sec. 3.2. Clearly, the odd-frequency component vanishes, when $\hat{F}_C$ vanishes. Odd-frequency pairing thus appears generally in multiorbital superconductors as soon as there is a finite interband pairing in the band basis, as signaled by a finite superconducting fitness, and is therefore connected to a suppression of the critical temperature [16]. Nevertheless, a superconducting order parameter giving rise to finite odd-frequency pairing can be the most stable solution, depending on the specific interaction and orbital structure of a certain material. Correspondingly, finite odd-frequency pairing has been found in Sr_2RuO_4 [127], UPt_3 [126], and buckled honeycomb materials, such as Silicene [15, 128].

6.3 Application to doped Bi_2Se_3

In Paper IV, we analyze the odd-frequency pairing in the prominent multiorbital superconductor, $M_x Bi_2 Se_3$, where the dopant M can be Cu, Sr, or Nb. The undoped compound Bi_2Se_3 is a 3D topological insulator [129, 130] made up of Se-Bi-Se-Bi-Se quintuple layers that are weakly van der Waals coupled. The quintuple layers feature a three fold rotation symmetry about the stacking direction, and the full symmetry is described by the point group D_{3d}. Bulk superconductivity with a critical temperature of about 3 K was first discovered upon doping with Cu [34]. Later studies revealed superconductivity with similar critical temperatures also for doping with Sr and Nb [131, 132]. A symmetry classification of possible $\boldsymbol{k}$-independent superconducting pairing states yields a number of odd-parity order parameters that could be realized even with simple pair interactions due to the nontrivial topology of the normal state [35]. One particular possibility is the pairing transforming according to the two-dimensional E_u irreducible representation, often labeled $(\Delta_{4x}, \Delta_{4x})$,

which consists of unconventional interorbital spin triplet pairing. All odd-parity pairing states would give rise to topological superconductivity due to the structure of the normal state Fermi surface [35], as discussed in Sec. 5.4. Experimental support for the Δ_4 pairing state has come from the appearance of nematic superconductivity in doped Bi_2Se_3 [36, 133, 134, 135, 37]. The rotational symmetry breaking of the order parameter manifested in strong two-fold symmetric behavior as a function of in-plane angle of, among others, specific heat, Knight shift, or magnetoresistance, can be explained by the formation of a real linear combination of the two basis functions of the two-dimensional irreducible representation [101, 136]. Doped Bi_2Se_3 therefore represents an experimentally verified multiorbital superconductor with unconventional interorbital spin triplet pairing. Based on the discussion in Sec. 6.2, odd-frequency pairing should naturally appear in the anomalous Green's function.

The normal state Hamiltonian of doped Bi_2Se_3 can be based on the undoped compound, as ARPES measurements show that the band structure of Bi_2Se_3 remains unchanged under doping [130, 137] and features conduction and valence band separated by a band gap of around $0.3\,\mathrm{eV}$. The bands are formed by two p orbitals of Se (with intermixing of Bi p orbitals) at the top and bottom of the quintuple layer [129]. This allows to introduce a two orbital continuum model describing the bands near the Γ point [35, 138, 139]

$$H_0 = \sum_{\boldsymbol{k}} \boldsymbol{\psi}_{\boldsymbol{k}}^{\dagger} \hat{h}_0(\boldsymbol{k}) \boldsymbol{\psi}_{\boldsymbol{k}}, \tag{6.20}$$

with

$$
\begin{aligned}
\hat{h}_0(\boldsymbol{k}) &= m\hat{\sigma}_x + v(k_x\hat{s}_y - k_y\hat{s}_x) \otimes \hat{\sigma}_z + v_z k_z \hat{\sigma}_y - \mu \\
&= \begin{pmatrix}
-\mu & -i(k_x - ik_y)v & m - ik_z v_z & 0 \\
i(k_x - ik_y)v & -\mu & 0 & m - ik_z v_z \\
m + ik_z v_z & 0 & -\mu & i(k_x - ik_y)v \\
0 & m + ik_z v_z & -i(k_x + ik_y)v & -\mu
\end{pmatrix}
\end{aligned} \tag{6.21}
$$

in the basis $\boldsymbol{\psi}_{\boldsymbol{k}} = \left(c_{\boldsymbol{k}1\uparrow}, c_{\boldsymbol{k}1\downarrow}, c_{\boldsymbol{k}2\uparrow}, c_{\boldsymbol{k}2\downarrow}\right)^T$. Here, $c_{\boldsymbol{k}i\sigma}$ annihilates an electron in orbital i of spin σ. The Pauli matrices $\hat{\sigma}_i$ and $\hat{s}_i$ act in orbital and spin spaces, respectively, v and v_z denote the in- and out-of-plane Fermi velocities of the electrons, respectively, m is an interorbital hybridization, and μ is the chemical potential. Diagonalizing the Hamiltonian yields a gapped 3D Dirac dispersion of the form $\varepsilon_{\pm}^0 = \pm\sqrt{m^2 + v^2(k_x^2 + k_y^2) + v_z^2 k_z^2} - \mu$. The two-fold degenerate valence and conductions bands are separated by a band gap of $2m$, such that the doping regime relevant for superconductivity is given by $\mu \geq m$ [137].

To reproduce the experimentally verified nematic superconductivity, the pairing matrix $\hat{\Delta}$ is made up of a linear combination $\hat{\Delta} = A_x\hat{\Delta}_{4x} + A_y\hat{\Delta}_{4y}$ of the $\boldsymbol{k}$-independent basis functions of the aforementioned two-dimensional E_u irreducible representation of the D_{3d} point group, $(\hat{\Delta}_{4x}, \hat{\Delta}_{4y}) = \Delta(s_0 \otimes i\sigma_y, s_z \otimes$

$i\sigma_y$) [35, 101]. The complex coefficients $A_{x/y}$ allow to form a nematic superconducting state for the choice of real coefficients $(A_x, A_y) = (\cos(\theta), \sin(\theta))$, where θ determines the angle of the headless nematic vector, or a chiral superconducting state for the coefficients $(A_x, A_y) = \left(1/\sqrt{2}, i/\sqrt{2}\right)$. The full BdG Hamiltonian is then written in terms of the Nambu spinor $\boldsymbol{\Psi}_k = \left(\boldsymbol{\psi}_k, \boldsymbol{\psi}^{\dagger}_{-k}\right)^T$ as

$$H = \boldsymbol{\Psi}^{\dagger}_k \begin{pmatrix} \hat{h}_0(\boldsymbol{k}) & \hat{\Delta} \\ \hat{\Delta}^{\dagger} & -\hat{h}^*_0(-\boldsymbol{k}) \end{pmatrix} \boldsymbol{\Psi}^{\dagger}_k, \tag{6.22}$$

where

$$\hat{\Delta} = \begin{pmatrix} 0 & 0 & (iA_x + A_y)\Delta & 0 \\ 0 & 0 & 0 & (-iA_x + A_y)\Delta \\ (-iA_x - A_y)\Delta & 0 & 0 & 0 \\ 0 & (iA_x - A_y)\Delta & 0 & 0 \end{pmatrix}. \tag{6.23}$$

As described in Sec. 6.2, the even- and odd-frequency pair amplitudes are determined by calculating the Matsubara anomalous Green's function from Eq. (6.13). Assuming a nematic pairing state $A_x, A_y \in \mathbb{R}$ yields the following odd- and even-frequency parts $\hat{F}(i\omega) = \hat{F}^o(i\omega) + \hat{F}^e(i\omega)$

$$\hat{F}^o(i\omega) = \frac{2\omega\Delta_0}{D_- D_+} \begin{pmatrix} A_- m & 0 & 0 & -A \times k \\ 0 & -A_+ m & A \times k & 0 \\ 0 & -A \times k & -A_- m & 0 \\ A \times k & 0 & 0 & A_+ m \end{pmatrix}, \tag{6.24}$$

and

$$\hat{F}^e(i\omega) = \frac{2\Delta_0}{D_- D_+} \times$$
$$\begin{pmatrix} A_- k_z \mu & mA \cdot k + k_z A \times k & \frac{i}{2}(A_- \gamma_- - A_+ k^2_-) & \mu A \cdot k \\ mA \cdot k - k_z A \times k & -A_+ k_z \mu & \mu A \cdot k & -\frac{i}{2}(A_+ \gamma_- - A_- k^2_+) \\ -\frac{i}{2}(A_- \gamma_+ - A_+ k^2_-) & \mu A \cdot k & A_- k_z \mu & mA \cdot k - k_z A \times k \\ \mu A \cdot k & \frac{i}{2}(A_+ \gamma_+ - A_- k^2_+) & mA \cdot k + k_z A \times k & -A_+ k_z \mu \end{pmatrix}, \tag{6.25}$$

where $k_{x,y} \equiv v k_{x,y}$, $k_z \equiv v_z k_z$, $\gamma_{\pm} = \left((m \pm i k_z)^2 - \mu^2 - \omega^2 - \Delta^2\right)$, $A_{\pm} = A_x \pm i A_y$, $A \times k = A_x k_y - A_y k_x$, and $A \cdot k = A_x k_x + A_y k_y$. The denominator is even in frequency and given by $D_{\pm} = \left((i\omega)^2 - \xi^2_{\pm}\right)$, with the eigenvalues of the BdG Hamiltonian $\xi_{\pm} = \sqrt{\varepsilon^2 + \Delta^2 + \mu^2 \pm \sqrt{\Delta^2(m^2 + (A \times k)^2) + \varepsilon^2 \mu^2}}$. To also obtain expressions for chiral pairing, the anomalous Green's function has to be determined perturbatively. Treating the superconducting order parameter Δ as a small quantity, the anomalous Green's function can be expanded to first

#	Pairing $\left(\hat{F}^{(1)}/D\right)$	Spin	Parity	Orbital	Frequency
1	$2iA_{\pm}m\omega\Delta$	$\uparrow\uparrow,\downarrow\downarrow$	s	intra	odd
2	$2i(A\times k)v\omega\Delta$	$\uparrow\downarrow-\downarrow\uparrow$	$p_{x,y}$	even-inter	odd
3	$2A_{\pm}k_z v_z\mu\Delta$	$\uparrow\uparrow,\downarrow\downarrow$	p_z	intra	even
4	$2(A\cdot k)vm\Delta$	$\uparrow\downarrow+\downarrow\uparrow$	$p_{x,y}$	intra	even
5	$2(A\times k)vk_z v_z\Delta$	$\uparrow\downarrow-\downarrow\uparrow$	d	intra	even
6	$iA_{\pm}(m^2-\mu^2+\omega^2)\Delta$	$\uparrow\uparrow,\downarrow\downarrow$	s	odd-inter	even
7	$iA_{\pm}k_z^2 v_z^2\Delta$	$\uparrow\uparrow,\downarrow\downarrow$	d	odd-inter	even
8	$2A_{\pm}k_z v_z\Delta$	$\uparrow\uparrow,\downarrow\downarrow$	p_z	even-inter	even
9	$2(A\cdot k)v\mu\Delta$	$\uparrow\downarrow+\downarrow\uparrow$	$p_{x,y}$	even-inter	even

Table 6.2. *Symmetry classification of the full pairing correlations in $\hat{F}^{(1)}$ for general (A_x,A_y) according to spin, parity, orbital, and frequency, using the shorthand notations $A_{\pm}=A_x\pm iA_y$, $A\cdot k=A_x k_x+A_y k_y$, $A\times k=A_x k_y-A_y k_x$, and $D=\prod_i((i\omega)^2-(\varepsilon_i^0)^2)$, with ε_i^0 the eigenvalues of $\hat{h}_0$. Table adapted from Paper IV.*

order in Δ

$$\hat{F}^{(1)}=\hat{G}_0\hat{\Delta}\hat{\bar{G}}_0, \tag{6.26}$$

where $\hat{G}_0$ is the Green's functions of the normal state Hamiltonian $\hat{h}_0$. The structure of $\hat{F}^{(1)}$ is identical to that of Eqs. 6.24 and 6.25, with the replacements $\gamma_{\pm}\rightarrow\left((m\pm ik_z)^2-\mu^2-\omega^2\right)$ and $\xi_{\pm}\rightarrow\varepsilon_{\pm}^0$.

All the pairing correlations contained in $\hat{F}^{(1)}$ then appear for both chiral and nematic pairing and are summarized in Tab. 6.2. The table also lists the classification according to spin, parity, orbital, and frequency. In total, there are eight different terms, one of which shares the same spin triplet, s-wave, interorbital, even-frequency symmetry as the order parameter (# 6 in Tab. 6.2). The only other s-wave pairing is of odd-frequency: A spin triplet, s-wave, intraorbital, odd-frequency pairing proportional to the interorbital hybridization m, labeled by # 1 in Tab. 6.2. Odd-frequency pairing therefore allows for a rather conventional s-wave intraorbital pairing, even though the superconducting order parameter is of unconventional interorbital type. The second odd-frequency pairing identified in $\hat{F}^o$, # 2 in Tab. 6.2, is a spin singlet, p-wave, even interorbital, odd-frequency pairing. Comparing odd- and even-frequency pairing amplitudes shows that odd-frequency pairing dominates over even-frequency pairing of the same parity for a large range of frequencies. In the relevant regime of bulk doping, i.e. $\mu>|m|$, the s-wave odd-frequency pairing
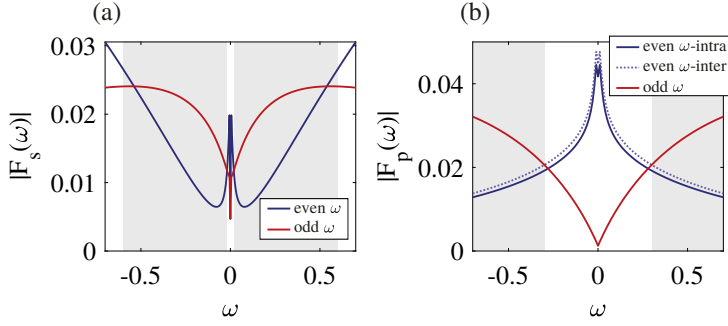
Figure 6.1. Comparison between the absolute value $|\hat{\mathcal{F}}(\omega)|$ integrated over $\boldsymbol{k}$ as a function of frequency for odd- and even-frequency pairing in the nematic state for a) *s*-wave and b) in-plane *p*-wave pairing. The shaded areas mark the frequency windows at which the odd-frequency exceeds the even-frequency pairing obtained analytically to first order. The nematic angle is set to $\pi/6$. Figure taken from Paper IV.

is larger than the even-frequency *s*-wave pairing for $m+\mu < |\omega| < -m+\mu$. Performing a similar comparison of the odd- and even-frequency in plane *p*-wave ($p_{x,y}$) pairing correlations (# 2, 4, and 9 in Tab. 6.2) , the odd-frequency term exceeds the even-frequency pair amplitudes for $|\omega| > m$, and $|\omega| > \mu$, respectively. Figure 6.1 shows numerical data to infinite order in Δ supporting the perturbative analytical results. Using parameters obtained from fitting to DFT and STM [138, 140], the pair amplitudes can be integrated over $\boldsymbol{k}$ using the usual replacement $i\omega \to \omega \pm i0^+$. The *p*-wave pairing correlations are multiplied by the corresponding form factors to give a finite value after integration. The frequency ranges in which the odd-frequency pair amplitudes dominate the respective even-frequency ones are clearly visible and in good agreement with the analytical results marked by the shading in Fig. 6.1 a) and b).

In summary, the multiorbital superconductivity in doped Bi_2Se_3 is characterized by dominant odd-frequency pairing. The odd-frequency pairing allows for *s*-wave, intraorbital pairing, even though the superconducting order parameter unconventionally forms interorbital Cooper pairs.

7. Meissner effect

Given the appearance of large odd-frequency pairing correlations in doped Bi_2Se_3, the question for an experimental signature arises. A commonly proposed detectable signature of odd-frequency pairing is a paramagnetic Meissner effect, which would be detrimental to the superconducting order by attracting instead of expelling external magnetic fields. In this chapter, I present how the Meissner response of the odd-frequency pairing in doped Bi_2Se_3 is actually diamagnetic, opening a possibility for designing stable odd-frequency superconductors. I begin by reviewing the phenomenological picture of the Meissner effect, based on the London equation. After that, I introduce the microscopic approach based on calculating response functions in linear response and recapitulate some of the evidence for a paramagnetic odd-frequency Meissner response. Finally, I discuss the complications arising for doped Bi_2Se_3 and summarize the results obtained in Paper IV.

7.1 Phenomenological equations

The Meissner effect is one of the core properties of a superconductor. It describes the suppression of an external magnetic field in the bulk of a superconductor. A phenomenological description of the Meissner effect can be derived from the London equation,

$$\boldsymbol{j} = -\frac{n_s e^2}{m}\boldsymbol{A},\tag{7.1}$$

which relates the superconducting current density $\boldsymbol{j}$ to an external vector potential $\boldsymbol{A}$. Here, n_s is the superconducting particle density, m and e are the mass and charge of the electron, respectively. Applying a curl and using the definition of the vector potential $\nabla \times \boldsymbol{A} = \boldsymbol{B}$ yields $\nabla \times \boldsymbol{j} = -\frac{n_s e^2}{m}\boldsymbol{B}$, which together with Ampere's law $\nabla \times \boldsymbol{B} = \mu_0 \boldsymbol{j}$ can be used to derive a differential equation for the magnetic field in the bulk of the superconductor

$$\nabla^2 \boldsymbol{B} = \frac{1}{\lambda^2}\boldsymbol{B}.\tag{7.2}$$

The constant $\lambda = \sqrt{\frac{m}{n_s e^2 \mu_0}}$ is called the London penetration depth. For a geometry where the superconductor has a boundary at $z = 0$ and is infinite in all other directions, Eq. (7.2) has the solution

$$\boldsymbol{B}(z) = \boldsymbol{B}_0 \mathrm{e}^{-\frac{z}{\lambda}},\tag{7.3}$$

which describes an exponentially decaying field inside the superconductor, where the London penetration depth sets the characteristic length scale of the decay. An external magnetic field therefore only penetrates the superconductor along the surface, but is expelled from the bulk. Essential for the expulsion is the minus sign in front of the positive coefficient $\frac{n_s e^2}{m}$ in the London equation Eq. (7.1).

7.2 Microscopic theory

In a microscopic approach, the London equation is replaced by [141]

$$j_\mu(\boldsymbol{q}, \omega_e) = -K_{\mu\nu}(\boldsymbol{q}, \omega_e) A_\nu(\boldsymbol{q}, \omega_e), \tag{7.4}$$

where the response of the current $\boldsymbol{j}$ to the external vector potential $\boldsymbol{A}(\boldsymbol{q}, \omega_e)$ with wave vector $\boldsymbol{q}$ and angular frequency ω_e is described by the response function $K_{\mu\nu}(\boldsymbol{q}, \omega_e)$. The response function is not guaranteed to be positive, opening the possibility for a paramagnetic Meissner effect, which attracts a magnetic field, for the case that $K < 0$. The traditional Meissner effect, as derived from the London equation and recovered for $K > 0$, is then called diamagnetic Meissner effect to highlight the suppression of the magnetic field.

A paramagnetic Meissner effect is considered a possible experimental evidence for odd-frequency superconductivity [19]. Quasiclassical calculations have predicted a paramagnetic Meissner response for proximity induced odd-frequency pairing in heterostructures [17, 18, 19], which has even been experimentally observed in Nb/Ho/Au heterostructures [20] and recently in Bi_2Se_3 in proximity to Nb [142]. A paramagnetic Meissner response has also been predicted for odd-frequency pairing arising in a general multiband superconductor [21]. The appearance of a paramagnetic Meissner response leads to questions of thermodynamic stability of an odd-frequency superconducting order [125, 143, 19] and would also prove detrimental for the even-frequency order inducing odd-frequency pairing in multiorbital superconductors [21, 16].

The response function determining the Meissner response can be calculated in linear response theory by treating the vector potential as a perturbation [141, 144],

$$K_{\mu\nu}(\boldsymbol{q}, \omega_e) = \langle j_\mu^P(\boldsymbol{q}, \omega_e) j_\nu^P(-\boldsymbol{q}, \omega_e) \rangle + \langle j_{\mu\nu}^D(\boldsymbol{q}, \omega_e) \rangle, \tag{7.5}$$

where all expectation values are taken with respect to the unperturbed Hamiltonian. The operators j^P and j^D are the second quantized paramagnetic and diamagnetic current operators, which are obtained from including the vector potential in the Hamiltonian through the Peierl's substitution $\boldsymbol{k} \rightarrow \boldsymbol{k} - \boldsymbol{A}$. After expanding to second order in $\boldsymbol{A}$ and differentiating with respect to the vector potential, the constant and linear terms in $\boldsymbol{A}$ can be identified with the param-

agnetic and diamagnetic current, respectively [141, 144]:

$$-\frac{\partial H_0(\boldsymbol{A})}{\partial A_\mu} = j_\mu^P + j_{\mu\nu}^D A_\nu + \mathcal{O}(A^2). \tag{7.6}$$

The Meissner effect is the response to a static, uniform field, which is expressed through the limit $\lim_{\boldsymbol{q}\to 0} \lim_{\omega_e \to 0} K_{\mu\nu}(\boldsymbol{q}, \omega_e)$, where the order of the limits is of importance [141]. The expectation values of the second quantized operators can be rewritten with the help of the Green's functions and the first quantized current operators as

$$K_{\mu\nu} = \lim_{\boldsymbol{q}\to 0} \lim_{\omega_e \to 0} K_{\mu\nu}(\boldsymbol{q}, \omega_e) = T \sum_{\boldsymbol{k}, i\omega} \mathrm{Tr}[\hat{G}\hat{j}_\mu^P \hat{G}\hat{j}_\nu^P + \hat{F}\hat{j}_\mu^P \hat{\bar{F}}\hat{j}_\nu^P] + T \sum_{\boldsymbol{k}, i\omega} \mathrm{Tr}[\hat{G}\hat{j}_\mu^D], \tag{7.7}$$

where the frequency and momentum dependence are suppressed for legibility. In the limit of $\Delta \to 0$, the diamagnetic and paramagnetic contributions cancel and the Meissner response disappears, as can be demonstrated for a simple quadratic band $h_0(k) = k^2 - \mu$. The anomalous Green's function vanishes in the normal state and the normal Green's function reduces to

$$G = G_0 = (i\omega - h_0(k))^{-1} = \frac{1}{i\omega - k^2 + \mu}. \tag{7.8}$$

The currents are determined from

$$j_\mu = -\frac{\partial h_0(k-A)}{\partial A_\mu} = 2k - 2A, \tag{7.9}$$

such that $j^P = 2k$ and $j^D = -2$. The Meissner kernel then reduces to

$$K_{\mu\nu} = T \sum_{\boldsymbol{k}, i\omega} \frac{4k^2}{(i\omega - k^2 + \mu)^2} - T \sum_{\boldsymbol{k}, i\omega} \frac{2}{i\omega - k^2 + \mu}. \tag{7.10}$$

Performing the Matsubara summation and taking the zero temperature limit $T \to 0$ yields

$$K_{\mu\nu} = \int_{-\infty}^{\infty} dk\, 4k^2 \delta(k^2 - \mu) - 2\int_{-\infty}^{\infty} dk\, (1 - \theta(k^2 - \mu)), \tag{7.11}$$

where $\delta(\varepsilon)$ is the Dirac-Delta function and $\theta(\varepsilon)$ is the Heaviside function. The Delta function can be split in two and the Heaviside function can be used to limit the integration boundaries, giving

$$K_{\mu\nu} = \int_{-\infty}^{\infty} dk\, 4k^2 \left(\frac{\delta(k - \sqrt{\mu})}{2\sqrt{\mu}} + \frac{\delta(k + \sqrt{\mu})}{2\sqrt{\mu}} \right) - 2\int_{-\sqrt{\mu}}^{\sqrt{\mu}} dk$$
$$= 4\sqrt{\mu} - 4\sqrt{\mu} = 0, \tag{7.12}$$

and the Meissner effect indeed vanishes in the normal state.

7.3 Meissner effect in doped Bi_2Se_3

In the case of Bi_2Se_3 discussed in Paper IV, the Hamiltonian presented in Sec. 6.3 is only linear in $\boldsymbol{k}$. Introducing the vector potential thus also does not yield a term quadratic in $\boldsymbol{A}$. This means that the current operator for the Hamiltonian, given by

$$\hat{j}_\mu = -\frac{\delta \hat{h}_0(\boldsymbol{A})}{\delta A_\mu}, \tag{7.13}$$

$$\hat{j}_x = -\hat{\bar{j}}_x^* = vs_y \otimes \sigma_z \quad \hat{j}_y = -\hat{\bar{j}}_y^* = -vs_x \otimes \sigma_z \quad \hat{j}_z = -\hat{\bar{j}}_z^* = v_z\sigma_y, \tag{7.14}$$

only consists of a paramagnetic current. The vanishing diamagnetic current operator means that the Meissner kernel then reduces to

$$K_{\mu\nu} = \lim_{\boldsymbol{q}\to 0}\lim_{\omega_e\to 0} K_{\mu\nu}(\boldsymbol{q},\omega_e) = T\sum_{\boldsymbol{k},i\omega}\mathrm{Tr}[\hat{G}\hat{j}_\mu^P\hat{G}\hat{j}_\nu^P + \hat{F}\hat{\bar{j}}_\mu^P\hat{\bar{F}}\hat{j}_\nu^P], \tag{7.15}$$

which does not vanish in the limit $\Delta \to 0$, giving rise to a non-physical non-zero Meissner response in the normal state. Furthermore, due to the linear dispersion, the first term in Eq. (7.15) even diverges at high energies. Both problems are caused by the unphysical assumption of a linear spectrum at higher energies, as actual materials will have a finite bandwidth with terms of higher powers in $\boldsymbol{k}$. However, introducing a regularization through subtracting the normal state response $Tr[\hat{G}_0\hat{j}_\mu\hat{G}_0\hat{j}_\nu]$ circumvents these issues [145, 146] and yields the same results as adding a small k^2 term to allow cancellation from the diamagnetic current [146]. In our case, we checked that the difference $Tr[\hat{G}\hat{j}_\mu\hat{G}\hat{j}_\nu] - Tr[\hat{G}_0\hat{j}_\mu\hat{G}_0\hat{j}_\nu]$ numerically vanishes for the parameters used in our model, even if Δ is small, but non-zero. The remaining superconducting contribution to the Meissner kernel is then given by

$$K_{\mu\nu}^{(S)} = T\sum_{\boldsymbol{k},\omega_n} Tr[\hat{F}\hat{\bar{j}}_\mu\hat{\bar{F}}\hat{j}_\nu], \tag{7.16}$$

which contains the full influence from the even- and odd-frequency correlations in the anomalous Green's function. Recalling the splitting $\hat{F} = \hat{F}^e + \hat{F}^o$, the Meissner kernel can be separated into even and odd-frequency contributions

$$K_{\mu\nu}^{(S)} = K_{\mu\nu}^e + K_{\mu\nu}^o = T\sum_{\boldsymbol{k},\omega_n} Tr[\hat{F}^e\hat{\bar{j}}_\mu\hat{\bar{F}}^e\hat{j}_\nu] + T\sum_{\boldsymbol{k},\omega_n} Tr[\hat{F}^o\hat{\bar{j}}_\mu\hat{\bar{F}}^o\hat{j}_\nu], \tag{7.17}$$

where the mixed terms $\hat{F}^e\hat{\bar{j}}_\mu\hat{\bar{F}}^o\hat{j}_\mu$ and $\hat{F}^o\hat{\bar{j}}_\mu\hat{\bar{F}}^e\hat{j}_\mu$ both are traceless and therefore do not contribute. Assuming nematic pairing, the expressions for the anomalous Green's functions Eqs. (6.24) and (6.24) and the paramagnetic current operators in Eq. (7.14) can be used to derive the following odd-frequency contribution the the Meissner kernel

$$K_{xx}^o = T\sum_{\boldsymbol{k},\omega_n} \frac{8\Delta_0^2\omega^2}{D_-^2 D_+^2}\left(2(A\times k)^2 + (A_+^2 + A_-^2)m^2\right), \tag{7.18}$$

making use of the shorthand notations introduced in Sec. 6.3. The even-frequency contributions are very lengthy expressions, so that I will not reproduce them here. Importantly, all the Meissner kernels for the nematic pairing follow the general form

$$K = T \sum_{\mathbf{k},\omega_n} \frac{a + b(i\omega)^2 + c(i\omega)^4}{(i\omega - \xi_+)^2 (i\omega + \xi_+)^2 (i\omega - \xi_-)^2 (i\omega + \xi_-)^2}, \qquad (7.19)$$

where a, b, and c are different frequency independent coefficients depending on the parameters of the model, and therefore functions of $\mathbf{k}$. The energies $\xi_{\pm}$ are the eigenvalues of the full BdG Hamiltonian as expressed in Sec. 6.3. The product of two anomalous Green's functions in the Meissner kernel guarantees that the expressions do not contain odd powers of $i\omega$, but the coefficient a is necessarily zero for the odd-frequency combination. The kernel can be split into intra- and interband processes as

$$K = K^{intra} + K^{inter}, \qquad (7.20)$$

$$K^{intra} = T \sum_{\mathbf{k},\omega_n} \left\{ \frac{\alpha}{\left((i\omega)^2 - \xi_+^2\right)^2} + \frac{\beta}{\left((i\omega)^2 - \xi_-^2\right)^2} \right\}, \qquad (7.21)$$

$$K^{inter} = T \sum_{\mathbf{k},\omega_n} \left\{ \frac{\gamma}{\left((i\omega)^2 - \xi_+^2\right) \left((i\omega)^2 - \xi_-^2\right)} \right\}. \qquad (7.22)$$

The new coefficients α, β, and γ are written in terms of a, b, c, and the band energies as

$$\alpha = \frac{a + b\xi_+^2 + c\xi_+^4}{(\xi_+^2 - \xi_-^2)^2}, \qquad \beta = \frac{a + b\xi_-^2 + c\xi_-^4}{(\xi_+^2 - \xi_-^2)^2}, \qquad (7.23)$$

$$\gamma = -\frac{2a + b(\xi_+^2 + \xi_-^2) + 2c(\xi_+^2 \xi_-^2)}{(\xi_+^2 - \xi_-^2)^2}. \qquad (7.24)$$

The Matsubara summation of the intra and interband kernels can be performed using the identities

$$T \sum_{i\omega} \frac{1}{\left((i\omega)^2 - \xi^2\right)^2} = \frac{1}{2\xi^2} \left(\mathcal{C}(\xi) + n'(\xi)\right), \qquad (7.25)$$

$$T \sum_{i\omega} \frac{1}{\left((i\omega)^2 - \xi_1^2\right) \left((i\omega)^2 - \xi_2^2\right)} = -\frac{\mathcal{C}(\xi_1) - \mathcal{C}(\xi_2)}{\xi_1^2 - \xi_2^2}, \qquad (7.26)$$

with the Fermi-Dirac distribution $n(\xi)$, its derivative $n'(\xi)$, and the combination $\mathcal{C}(\xi) = (n(-\xi) - n(\xi))/2\xi$. At finite temperature, these are given by $n(\xi) = \frac{1}{2}\left(1 - \tanh\left(\frac{\beta\xi}{2}\right)\right), n'(\xi) = -\frac{\beta}{4}\mathrm{sech}\left(\frac{\beta\xi}{2}\right)$, and $\mathcal{C}(\xi) = \frac{1}{2\xi}\tanh\left(\frac{\beta\xi}{2}\right)$. The Meissner response from intra and interband processes is then determined

118

from the $\mathbf{k}$ integrals

$$K^{intra} = \int d\mathbf{k} \left\{ \frac{a + b\xi_+^2 + c\xi_+^4}{2\left(\xi_+^2 - \xi_-^2\right)^2 \xi_+^2} \left(\mathcal{C}\left(\xi_+\right) + n'\left(\xi_+\right)\right) \right.$$

$$\left. + \frac{a + b\xi_-^2 + c\xi_-^4}{2\left(\xi_+^2 - \xi_-^2\right)^2 \xi_-^2} \left(\mathcal{C}\left(\xi_-\right) + n'\left(\xi_-\right)\right) \right\} \qquad (7.27)$$

$$K^{inter} = \int d\mathbf{k} \left\{ \frac{2a + b\left(\xi_+^2 + \xi_-^2\right) + 2c\left(\xi_+^2 \xi_-^2\right)}{\left(\xi_+^2 - \xi_-^2\right)^3} \left(\mathcal{C}\left(\xi_+\right) - \mathcal{C}\left(\xi_-\right)\right) \right\}. \qquad (7.28)$$

The resulting Meissner response after integration for odd- and even-frequency pairing in the nematic state is presented in panels a) and b) of Figure 7.1. The total Meissner response is dominated by the even-frequency pairing and diamagnetic. The much smaller odd-frequency contribution is, however, not paramagnetic as expected, but diamagnetic, too. This is the result of a cancellation of the intra- and interband contributions, whose magnitude close to the onset of the conduction band and sign are displayed in Fig. 7.1 c) and d), respectively. Panel d) shows that the intraband processes contribute as expected, with a diamagnetic even-frequency and a paramagnetic odd-frequency contribution. The interband processes, however, come with the opposite sign, such that the total Meissner response is the result of a competition between intra- and interband processes. The even-frequency pairing is dominated by the intraband contribution, as clearly visible in Fig. 7.1 c), which is driven by the frequency independent coefficient a. For the odd-frequency pairing, intra- and interband processes are of the same order of magnitude, yielding the reduced, but diamagnetic odd-frequency Meissner response shown in Fig. 7.1 b).

In summary, the odd-frequency pairing in doped Bi_2Se_3 gives rise to a reduced, but diamagnetic Meissner response. Even though the contribution is small and therefore not likely to be experimentally detectable, the competition between intra- and interband processes could in principle be used to tune or discover other odd-frequency materials with a stable diamagnetic Meissner response.
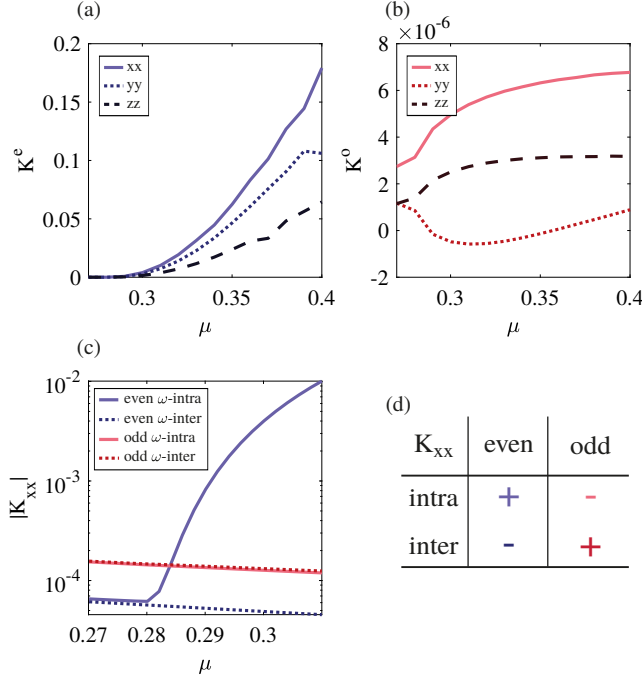
Figure 7.1. Even- and odd-frequency contributions to the Meissner effect in the nematic state as a function of chemical potential. a) and b) show the $K_{xx}^{(S)}$, $K_{yy}^{(S)}$, and $K_{zz}^{(S)}$ Meissner responses from even- and odd-frequency pairing, respectively. The even-frequency pairing gives rise to the dominant diamagnetic Meissner response, while the odd-frequency contributions are smaller, but also diamagnetic for most parameters. c) The intra- and interband processes for even- and odd-frequency contributions near the onset of the conduction band. Intraband processes dominate the even-frequency response, while intra- and interband processes are of equal order of magnitude for odd-frequency pairing. d) Overview over the different signs of even- and odd-frequency intra- and interband contributions to $K_{xx}^{(S)}$ displayed in c). The signs of the intraband processes are as expected, but opposite to those of the interband processes. The nematic angle is set to $\pi/6$ throughout. Figure reproduced from Paper IV.

8. Conclusion and Outlook

This thesis contributes to the study of superconductivity in multiorbital materials by studying two exemplary systems. Investigating superconductivity in the Kitaev materials, which made up the first part of the thesis, we try to answer two main questions: What is the influence of the 3D lattice structures in the harmonic honeycomb lattices? And what role does the off-diagonal exchange play for the arising order parameters? The first question can be answered from the symmetry analysis of the spin singlet superconductivity originating from the simplified interactions we used in Paper I. The fact that the bond order parameters split into groups, which transform independently under the symmetries of the lattice, allows for sign changes between these groups of bonds even in the trivial irreducible representation. This leads to the appearance of nodal superconducting phases. The topological protection of these nodal states subsequently gives rise to surface excitations, such as flat bands or Fermi arcs. The off-diagonal exchange, in turn, enriches the spin triplet pairing appearing in the Kitaev materials. On the 2D honeycomb lattice, a simple change of the sign of Γ discriminates between distinct superconducting states with different symmetries. Negative values of the off-diagonal exchange, in particular, give rise to chiral superconductivity at higher doping than previously observed for the experimentally relevant ferromagnetic Kitaev interaction. They also support the formation of nematic superconductivity, which had previously only been discussed in 3D systems. When combining the two effects by studying the extended Kitaev-Heisenberg model on the hyperhoneycomb lattice, the role of the lattice structure is more pronounced and again gives rise to topologically protected nodal phases. The off-diagonal exchange is not as influential as in the 2D case, although it drives a competition between different superconducting states in the absence of spin-orbit coupling by apparently lifting an accidental degeneracy.

Nevertheless, there are still several open questions for future research. First of all, a proper symmetry classification of the basis functions for spin triplet superconductivity in the presence of spin-orbit coupling is needed to fully understand the pairing obtained on the hyperhoneycomb lattice. The results could then also give possible trends for spin triplet pairing on the whole harmonic honeycomb series, similar to the spin singlet case. Another future research direction would be to study the competition between chiral and nematic superconductivity observed on the honeycomb lattice. The question why nematic superconductivity is stabilized at all is not fully understood and the situation seems to be rather intricate in the case of the extended Kitaev-Heisenberg

interaction. While the connection to the topological transition appears to be due to a fine-tuning of the parameters, the phase diagram in Paper II already reveals that the competition can be driven by doping and interaction strength. There are also hints that temperature could also lead to a transition between the two different topological states. Finally, it might be worthwhile to analyze the interplay of the superconducting states with other ordered states, such as the complex magnetic orderings observed in experiments, and the connection to the spin liquid phases present in certain limits of the model. This might require using more involved slave-boson approaches and going beyond mean-field theory [32, 69, 70].

Our work on the doped topological insulator Bi_2Se_3 summarized in Part II of this thesis reveals the importance of odd-frequency pairing for the already intricate superconductivity emerging upon doping. The odd-frequency pairing correlations are actually dominant in specific frequency ranges and are therefore expected to influence the superconducting properties. Bi_2Se_3 is also the first instance of an intraorbital odd-frequency pairing, which is possible due to the proposed interorbital order parameter. Finally, our calculations of the Meissner response show that the observed small, but diamagnetic odd-frequency Meissner response actually stabilizes superconductivity. This also implies that the assumption of a paramagnetic Meissner effect caused by odd-frequency pairing needs to be revisited and cannot be considered as a unique smoking gun for odd-frequency superconductivity in multiorbital superconductors.

To further clarify this situation, a first step would be to use a model beyond the linear dispersion for Bi_2Se_3 to understand the role of the diamagnetic current operator. Another question is whether the diamagnetic odd-frequency Meissner response is specific for Bi_2Se_3 or if it can be extended to other multiorbital odd-frequency superconductors. In particular, what is the difference to the generic multiband model that gives rise to a paramagnetic Meissner response [21]? On more general terms, what is the connection between a detrimental paramagnetic Meissner effect and the superconducting fitness function $\hat{F}_C$ discussed in Sec. 3.2 [5] and can the superconducting fitness be used to uncover trends in the Meissner response? Finally, the general search to find clear signatures of odd-frequency pairing, both in doped Bi_2Se_3 and in general multiorbital superconductors, remains a future challenge.

Altogether, the articles compiled and summarized in this thesis offer a glimpse into the complexity of the superconducting states arising at the intersection of multiorbital, topological, and odd-frequency superconductivity. In the Kitaev materials complex strong interactions yield superconducting orders that break a variety of different symmetries and belong to a several distinct topological classes. The multiorbital nature of superconductivity in Bi_2Se_3 leads to odd-frequency pairing with unexpected consequences on the Meissner response. Even though the underlying materials play an important role in the observed diversity, it is still possible to draw generalizations beyond them.

Overall, the study of topological superconductivity in multiorbital materials is still in its beginning and many new discoveries are going to extend the research field of superconductivity even further in the next one hundred years.

Acknowledgements

During the more than five years I have worked on this thesis, a lot of people have contributed to it directly or indirectly, by supporting the work or by supporting my well-being. Many of you should be named several times and for many things I did not even list below, please feel included every time I did not name you. And if I forgot to mention you at all, it's because I am scrambling this together at the last minute. Thanks for shared memories and pleasant times together, you made PhD life a great experience! I am very grateful to all of you.

Special thanks belong of course to my supervisor, Annica, for your guidance and support. You always had time for a meeting, and you were always super quick and on point with commenting anything I wrote. Thank you for being exactly the supervisor I needed.

Thank you also to Jonas for being my second supervisor, even though that was very little work for you. You are setting a great example of how you can be a great scientist staying true to your values.

A big thanks goes out to all of my co-authors. Adrien, you showed me how to really dig into a topic and become an expert. Thanks for all your support when I just got started on the first projects. Daniel, thank you for all the support during my master work. You set the bar for what it means to work in condensed matter physics. I am sorry we never got more out of our fRG projects. Fariborz, thank you for reminding me of the importance of taking a piece of paper and a pen. Getting the Meissner effect to work was stressful at times, but I think we had a good outcome in the end!

Thank you to my office mates. Anna, you are great at always bringing people together by planning activities at someone else's place. Thank you for not reading your emails. Kristofer, thank you for the warm welcome and for sharing all that enthusiasm about your every project. Mahroo and Suhas, it was only for a short time we shared our new office, but I always enjoyed our time together. Tomas, thank you for all the deep and less deep discussions starting from innocent questions. You have become a huge influence on how I view science, teaching, coding, and life in general.

My PhD brothers Ola and Francesco, brought together by starting the PhD at the same time, thanks for sharing this ride with all its ups and downs.

A big shout out to the extended Villa people, Henning, Andreas, Jorge, Chris, Umberto, Juan David, Lucia, Mahdi, Dushko, Debmalya, Charlotta, Paramita, Iman, Peter, Ramon, Seif, Johan, Anders, Erik, Manuel, and everyone I forgot. Thank you for stimulating discussions at lunch or in the corridor,

for barbecues, and in general for making the Villa a place to enjoy and to miss. The thesis cover is for you.

Thank you also to the wider circle of the Materials theory division. It is a place full of great people from the more senior like Olle (let's meet again in the mountains) or Susanne (thanks for everything you do in the countless boards and positions that we met), to the more junior like Yaroslav and Pablo (thanks for sharing goals and beers), to the youngsters like Raquel, Johan, Samara, Fabian, Iulia, Vancho, Alex, Leandro, Paul, Sebastian, Rafael. Emel. Lots of names to add, thanks for conversations at fika or over lunch.

Thanks for everyone who shared the burden and joy of teaching with me, Tobi (world's best lab teacher), Agne, Jakob, Ida, Marek, Walter, Björn-Erik, John, Franz, Thomas, and everyone I forgot. Thanks Gabriella, Ulf, and Elin for trusting us (more or less). A shoutout also to the Green grinches with rockwishes.

Thank you to my co-ombud Maciej for all the time spent frustrated about the teaching compensation, but also to all the other people on the physics council, like Sara, Sofie, Georgii, Svenja, Henry, Rebecca, Fredrik. Another thank you for all of you who took the time to join TNDR to improve life for PhD students, especially my co-social organizers Jakob and Tobi (you get named twice), Tatyana, Rasmus, Anna, Mohsen, Frauke, Ruben, Warren, Belinda, George, Charlotte, Angeliki, and everyone else who came to the council meetings. And all of you who came to a TNDR social event, like Babis, Elisabetta, Lukas, thank you for making each of them a great time.

Thank you to all the football people who came out to do something about that bad posture from sitting too much, I enjoyed all those Mondays and Wednesdays: Victor, Ola, Taha, Theo, Remi, Mohammed, Edgar, Gustav, Moustafa, Fikret, Shewan and kids, Dana, Lars, Paer, Rafael, Thomas, and many, many others. It was great to see football bring us all together, across disciplines, jobs, cultures, languages.

Here I run out of reasons to thank you for, so thank you to everyone else I met during the last five plus years who made the time in Uppsala so very pleasant, including but not restricted to Sara, Sven, Xiaomeng and Malcolm, Asta and Patrik, the whole team of Uppsala Inter, Siv and Ove, Shirin and Sotiris.

Vielen Dank an meine Eltern, Schwiegereltern und Großeltern. Ihr habt uns immer unterstützt, habt euch mit Anrufen und Skypetelefonaten begnügt und nur wenig geklagt, dass wir so weit weg waren. Danke für euer Interesse und die Besuche. Danke auch an die erweiterte Rudisch-Schmidt Familie für eure Unterstützung, die interessierten Nachfragen, und ganz besonders für alle Besuche. Danke an Christian, Franzi, Tian und Gustav, die Siedler, Tristan und Vinc (soo viele Pilze) und alle anderen.

Thank you to all my friends from down in Germany who visited, called, wrote, and stayed in touch, Hendrik, Malte, Manu, Emanuel, Fredy und Gregor, Elli und Gerrit, Luise, Sabrina und Andreas, Caro und Philipp, Anika,

Caro, Clara und Felix, and many more. Sorry for not coming to see you more often.

Thanks to Paul Dirac for incredible fluffiness.

Simon, thank you for being such a wonderful little person. It is amazing to see you grow. You make me happy every day.

And the biggest thank you of all belongs to you, Katha, for being with me through the whole time. And what a time it was, full of bike rides up the hill to the office, long working hours, conference visits, Swingkatten evenings, PartyBusGefährt journeys, hiking adventures, paddling trips, weddings, funerals, birthdays, baptisms, lazy Sundays on the couch, almost not having an apartment and having three apartments, travels to Sweden, Germany and the world, a pandemic, and finally two PhD theses. Through all of this, you knew when to build me up when I was down and when to push me when I was just not moving forward. Thank you for everything. I love you!

Bibliography

[1] H. K. Onnes. "The resistance of pure mercury at helium temperatures". In: *Commun. Phys. Lab. Univ. Leiden* 12 (1911), pp. 120+.

[2] Leon N. Cooper. "Bound Electron Pairs in a Degenerate Fermi Gas". In: *Phys. Rev.* 104 (4 1956), pp. 1189–1190.

[3] J. Bardeen, L. N. Cooper, and J. R. Schrieffer. "Theory of Superconductivity". In: *Phys. Rev.* 108 (5 1957), pp. 1175–1204.

[4] Manfred Sigrist and Kazuo Ueda. "Phenomenological Theory of Unconventional Superconductivity". In: *Rev. Mod. Phys.* 63 (2 1991), pp. 239–311.

[5] Aline Ramires and Manfred Sigrist. "Identifying detrimental effects for multiorbital superconductivity: Application to Sr_2RuO_4". In: *Phys. Rev. B* 94 (10 2016), p. 104501.

[6] Aline Ramires, Daniel F. Agterberg, and Manfred Sigrist. "Tailoring T_c by symmetry principles: The concept of superconducting fitness". In: *Phys. Rev. B* 98 (2 2018), p. 024501.

[7] Lionel Andersen et al. "Generalized Anderson's theorem for superconductors derived from topological insulators". In: *Sci. Adv.* 6.9 (2020), eaay6502.

[8] D. C. Cavanagh and P. M. R. Brydon. "Robustness of unconventional s-wave superconducting states against disorder". In: *Phys. Rev. B* 101 (5 2020), p. 054509.

[9] Masatoshi Sato and Yoichi Ando. "Topological superconductors: a review". In: *Rep. Prog. Phys.* 80.7 (2017), p. 076501.

[10] C.W.J. Beenakker. "Search for Majorana Fermions in Superconductors". In: *Annu. Rev. Cond. Matt. Phys.* 4.1 (2013), pp. 113–136.

[11] Andreas P. Schnyder et al. "Classification of topological insulators and superconductors in three spatial dimensions". In: *Phys. Rev. B* 78 (19 2008), p. 195125.

[12] Ching-Kai Chiu et al. "Classification of topological quantum matter with symmetries". In: *Rev. Mod. Phys.* 88 (3 2016), p. 035005.

[13] VL Berezinskii. "New model of the anisotropic phase of superfluid He3". In: *JETP Lett.* 20.9 (1974), pp. 287–289.

[14] F. S. Bergeret, A. F. Volkov, and K. B. Efetov. "Odd triplet superconductivity and related phenomena in superconductor-ferromagnet structures". In: *Rev. Mod. Phys.* 77 (4 2005), pp. 1321–1373.

[15] Annica M. Black-Schaffer and Alexander V. Balatsky. "Odd-frequency superconducting pairing in multiband superconductors". In: *Phys. Rev. B* 88 (10 2013), p. 104514.

[16] Christopher Triola, Jorge Cayao, and Annica M. Black-Schaffer. "The Role of Odd-Frequency Pairing in Multiband Superconductors". In: *Ann. Phys.* 532.2 (2020), p. 1900298.

[17] Y. Tanaka et al. "Anomalous features of the proximity effect in triplet superconductors". In: *Phys. Rev. B* 72 (14 2005), p. 140503.

[18] S. Mironov, A. Mel'nikov, and A. Buzdin. "Vanishing Meissner effect as a Hallmark of in–Plane Fulde-Ferrell-Larkin-Ovchinnikov Instability in Superconductor–Ferromagnet Layered Systems". In: *Phys. Rev. Lett.* 109 (23 2012), p. 237002.

[19] Jacob Linder and Alexander V. Balatsky. "Odd-frequency superconductivity". In: *Rev. Mod. Phys.* 91 (4 2019), p. 045005.

[20] A. Di Bernardo et al. "Intrinsic Paramagnetic Meissner Effect Due to s-Wave Odd-Frequency Superconductivity". In: *Phys. Rev. X* 5 (4 2015), p. 041021.

[21] Yasuhiro Asano and Akihiro Sasaki. "Odd-frequency Cooper pairs in two-band superconductors and their magnetic response". In: *Phys. Rev. B* 92 (22 2015), p. 224508.

[22] Jeffrey G. Rau, Eric Kin-Ho Lee, and Hae-Young Kee. "Spin-Orbit Physics Giving Rise to Novel Phases in Correlated Systems: Iridates and Related Materials". In: *Annu. Rev. Cond. Matt. Phys.* 7.1 (2016), pp. 195–221.

[23] Simon Trebst. *Topological Matter - Topological Insulators, Skyrmions and Majoranas, Chapter D3 - Kitaev Materials*. Ed. by Stefan Blügel and Yuriy Mokrousov and Thomas Schäpers and Yoichi Ando. Schriften des FZ Jülich - Key Technologies, 2017.

[24] G. Jackeli and G. Khaliullin. "Mott Insulators in the Strong Spin-Orbit Coupling Limit: From Heisenberg to a Quantum Compass and Kitaev Models". In: *Phys. Rev. Lett.* 102 (1 2009), p. 017205.

[25] Jiri Chaloupka, George Jackeli, and Giniyat Khaliullin. "Kitaev-Heisenberg Model on a Honeycomb Lattice: Possible Exotic Phases in Iridium Oxides A_2IrO_3". In: *Phys. Rev. Lett.* 105 (2 2010), p. 027204.

[26] Jeffrey G. Rau, Eric Kin-Ho Lee, and Hae-Young Kee. "Generic Spin Model for the Honeycomb Iridates beyond the Kitaev Limit". In: *Phys. Rev. Lett.* 112 (7 2014), p. 077204.

[27] Yogesh Singh and P. Gegenwart. "Antiferromagnetic Mott Insulating State in Single Crystals of the Honeycomb Lattice material Na_2IrO_3". In: *Phys. Rev. B* 82 (6 2010), p. 064412.

[28] J. A. Sears et al. "Magnetic order in $\alpha - RuCl_3$: A honeycomb-lattice quantum magnet with strong spin-orbit coupling". In: *Phys. Rev. B* 91 (14 2015), p. 144420.

[29] S. C. Williams et al. "Incommensurate counterrotating magnetic order stabilized by Kitaev interactions in the layered honeycomb $\alpha - Li_2IrO_3$". In: *Phys. Rev. B* 93 (19 2016), p. 195158.

[30] A. Biffin et al. "Unconventional magnetic order on the hyperhoneycomb Kitaev lattice in β-Li_2IrO_3: Full solution via magnetic resonant x-ray diffraction". In: *Phys. Rev. B* 90 (20 2014), p. 205116.

[31] A. Biffin et al. "Noncoplanar and Counterrotating Incommensurate Magnetic Order Stabilized by Kitaev Interactions in γ-Li_2IrO_3". In: *Phys. Rev. Lett.* 113 (19 2014), p. 197201.

[32] Yi-Zhuang You, Itamar Kimchi, and Ashvin Vishwanath. "Doping a Spin-Orbit Mott insulator: Topological Superconductivity from the Kitaev-Heisenberg Model and Possible Application to Na_2IrO_3". In: *Phys. Rev. B* 86 (8 2012), p. 085145.

[33] Timo Hyart et al. "Competition Between d-Wave and Topological p-Wave Superconducting Phases in the Doped Kitaev-Heisenberg Model". In: *Phys. Rev. B* 85 (14 2012), p. 140510.

[34] Y. S. Hor et al. "Superconductivity in $Cu_xBi_2Se_3$ and its Implications for Pairing in the Undoped Topological Insulator". In: *Phys. Rev. Lett.* 104 (5 2010), p. 057001.

[35] Liang Fu and Erez Berg. "Odd-Parity Topological Superconductors: Theory and Application to $Cu_xBi_2Se_3$". In: *Phys. Rev. Lett.* 105 (9 2010), p. 097001.

[36] K. Matano et al. "Spin-rotation symmetry breaking in the superconducting state of $Cu_xBi_2Se_3$". In: *Nat. Phys.* 12.9 (2016), pp. 852–854.

[37] Shingo Yonezawa. "Nematic Superconductivity in Doped Bi_2Se_3 Topological Superconductors". In: *Condens. Matter* 4.1 (2018).

[38] Alexei Kitaev. "Anyons in an exactly solved model and beyond". In: *Ann. Phys. (NY)* 321.1 (2006), pp. 2 –111.

[39] Hidenori Takagi et al. "Concept and realization of Kitaev quantum spin liquids". In: *Nature Reviews Physics* 1.4 (2019), pp. 264–280.

[40] B. J. Kim et al. "Novel $J_{eff} = 1/2$ Mott State Induced by Relativistic Spin-Orbit Coupling in Sr_2IrO_4". In: *Phys. Rev. Lett.* 101 (7 2008), p. 076402.

[41] Yogesh Singh et al. "Relevance of the Heisenberg-Kitaev Model for the Honeycomb Lattice Iridates A_2IrO_3". In: *Phys. Rev. Lett.* 108 (12 2012), p. 127203.

[42] K. W. Plumb et al. "$\alpha - RuCl_3$: A spin-orbit assisted Mott insulator on a honeycomb lattice". In: *Phys. Rev. B* 90 (4 2014), p. 041112.

[43] K. A. Modic et al. "Realization of a Three-Dimensional Spin-Anisotropic Harmonic Honeycomb Iridate". In: *Nat. Commun.* 5.4203 (June 2014), p. 4203.

[44] T. Takayama et al. "Hyperhoneycomb Iridate β-Li_2IrO_3 as a Platform for Kitaev Magnetism". In: *Phys. Rev. Lett.* 114 (7 Feb. 2015), p. 077202.

[45] S.E. Barnes. "New Method for Anderson Model". In: *Journal of Physics F – Metal Physics* 6.7 (1976), 1375–1383.

[46] Piers Coleman. "New approach to the mixed-valence problem". In: *Phys. Rev. B* 29 (6 1984), pp. 3035–3044.

[47] Patrick A. Lee, Naoto Nagaosa, and Xiao-Gang Wen. "Doping a Mott insulator: Physics of High-Temperature Superconductivity". In: *Rev. Mod. Phys.* 78 (1 2006), pp. 17–85.

[48] G. Baskaran, Z. Zou, and P.W. Anderson. "The resonating valence bond state and high-Tc superconductivity — A mean field theory". In: *Solid State Commun.* 63.11 (1987), pp. 973–976.

[49] Gabriel Kotliar and Andrei E. Ruckenstein. "New Functional Integral Approach to Strongly Correlated Fermi Systems: The Gutzwiller Approximation as a Saddle Point". In: *Phys. Rev. Lett.* 57 (11 1986), pp. 1362–1365.

[50] Frank Lechermann et al. "Rotationally Invariant Slave-Boson Formalism and Momentum Dependence of the Quasiparticle Weight". In: *Phys. Rev. B* 76 (15 2007), p. 155102.

[51] F. C. Zhang et al. "A renormalised Hamiltonian approach to a resonant valence bond wavefunction". In: *Supercond. Sci. Technol.* 1.1 (1988), pp. 36–46.

[52] B. Edegger, V. N. Muthukumar, and C. Gros. "Gutzwiller-RVB Theory of High Temperature Superconductivity: Results from Renormalised Mean Field Theory and Variational Monte Carlo Calculations". In: *Adv. Phys.* 56 (July 6, 2007), p. 927.

[53] Stephen M. Winter et al. "Models and Materials for Generalized Kitaev Magnetism". In: *J. Phys. Condens. Matter* (2017).

[54] Yuriy Sizyuk et al. "Importance of Anisotropic Exchange Interactions in Honeycomb Iridates: Minimal Model for Zigzag Antiferromagnetic Order in Na_2IrO_3". In: *Phys. Rev. B* 90 (15 2014), p. 155126.

[55] Heung-Sik Kim et al. "Kitaev magnetism in honeycomb $RuCl_3$ with intermediate spin-orbit coupling". In: *Phys. Rev. B* 91 (24 2015), p. 241110.

[56] Stephen M. Winter et al. "Challenges in design of Kitaev materials: Magnetic interactions from competing energy scales". In: *Phys. Rev. B* 93 (21 2016), p. 214431.

[57] Itamar Kimchi, James G. Analytis, and Ashvin Vishwanath. "Three-dimensional quantum spin liquids in models of harmonic-honeycomb iridates and phase diagram in an infinite-*D* approximation". In: *Phys. Rev. B* 90 (20 2014), p. 205126.

[58] Itamar Kimchi, Radu Coldea, and Ashvin Vishwanath. "Unified theory of spiral magnetism in the harmonic-honeycomb iridates α, β, and $\gamma - Li_2IrO_3$". In: *Phys. Rev. B* 91 (24 2015), p. 245134.

[59] Eric Kin-Ho Lee and Yong Baek Kim. "Theory of magnetic phase diagrams in hyperhoneycomb and harmonic-honeycomb iridates". In: *Phys. Rev. B* 91 (6 2015), p. 064407.

[60] A. Banerjee et al. "Proximate Kitaev quantum spin liquid behaviour in a honeycomb magnet". In: *Nat. Mater.* (Apr. 2016).

[61] J. Nasu et al. "Fermionic response from fractionalization in an insulating two-dimensional magnet". In: *Nat. Phys.* 12.10 (2016). Letter, pp. 912–915.

[62] A. Glamazda et al. "Raman spectroscopic signature of fractionalized excitations in the harmonic-honeycomb iridates β- and γ-Li_2IrO_3". In: *Nature Communications* 7.1 (2016).

[63] K. Kitagawa et al. "A spin–orbital-entangled quantum liquid on a honeycomb lattice". In: *Nature* 554.7692 (2018), pp. 341–345.

[64] S.-H. Baek et al. "Evidence for a Field-Induced Quantum Spin Liquid in α-$RuCl_3$". In: *Phys. Rev. Lett.* 119 (3 2017), p. 037201.

[65] Y. Kasahara et al. "Majorana quantization and half-integer thermal quantum Hall effect in a Kitaev spin liquid". In: *Nature* 559.7713 (2018), pp. 227–231.

[66] O. Tanaka et al. "Thermodynamic evidence for field-angle dependent Majorana gap in a Kitaev spin liquid". In: (July 14, 2020). arXiv: 2007. 06757v1.

[67] Masao Ogata and Hidetoshi Fukuyama. "The *t-J* Model for the Oxide High- T_c Superconductors". In: *Rep. Prog. Phys.* 71.3 (2008), p. 036501.

[68] Timo Hyart, Anthony R. Wright, and Bernd Rosenow. "Zeeman-field-induced topological phase transitions in triplet superconductors". In: *Phys. Rev. B* 90 (6 2014), p. 064507.

[69] Satoshi Okamoto. "Global Phase Diagram of a doped Kitaev-Heisenberg Model". In: *Phys. Rev. B* 87 (6 2013), p. 064508.

[70] Daniel D. Scherer et al. "Unconventional Pairing and Electronic Dimerization Instabilities in the Doped Kitaev-Heisenberg Model". In: *Phys. Rev. B* 90 (4 2014), p. 045135.

[71] Annica M Black-Schaffer and Carsten Honerkamp. "Chiral *d*-Wave Superconductivity in Doped Graphene". In: *J. Phys.: Condens. Matter* 26.42 (2014), p. 423201.

[72] Bin-Bin Wang et al. "Particle–hole fluctuations and possible superconductivity in doped α-RuCl$_3$". In: *Chin. Phys. B* 28.5 (2019), p. 057402.

[73] Tianhan Liu et al. "Triplet FFLO superconductivity in the doped Kitaev-Heisenberg honeycomb model". In: *Phys. Rev. B* 94 (18 2016), p. 180506.

[74] Urban F. P. Seifert, Tobias Meng, and Matthias Vojta. "Fractionalized Fermi liquids and exotic superconductivity in the Kitaev-Kondo lattice". In: *Phys. Rev. B* 97 (8 2018), p. 085118.

[75] Wonjune Choi et al. "Topological superconductivity in the Kondo-Kitaev model". In: *Phys. Rev. B* 98 (15 2018), p. 155123.

[76] R. Comin et al. "Na$_2$IrO$_3$ as a Novel Relativistic Mott Insulator with a 340-meV Gap". In: *Phys. Rev. Lett.* 109 (26 2012), p. 266406.

[77] A. Koitzsch et al. "Nearest-neighbor Kitaev exchange blocked by charge order in electron-doped $\alpha - $RuCl$_3$". In: *Phys. Rev. Materials* 1 (5 2017), p. 052001.

[78] Xiaoqing Zhou et al. "Angle-resolved photoemission study of the Kitaev candidate $\alpha - $RuCl$_3$". In: *Phys. Rev. B* 94 (16 2016), p. 161106.

[79] P. Lampen-Kelley et al. "Destabilization of Magnetic Order in a Dilute Kitaev Spin Liquid Candidate". In: *Phys. Rev. Lett.* 119 (23 2017), p. 237203.

[80] Seung-Hwan Do et al. "Short-range quasistatic order and critical spin correlations in $\alpha - Ru_{1-x}Ir_xCl_3$". In: *Phys. Rev. B* 98 (1 2018), p. 014407.

[81] Yoshinori Imai et al. "Hydrated lithium intercalation into the Kitaev spin liquid candidate material $\alpha - $RuCl$_3$". In: *Phys. Rev. B* 99 (24 2019), p. 245141.

[82] Sananda Biswas et al. "Electronic Properties of $\alpha - $RuCl$_3$ in Proximity to Graphene". In: *Phys. Rev. Lett.* 123 (23 2019), p. 237201.

[83] Eli Gerber et al. "Ab Initio Mismatched Interface Theory of Graphene on $\alpha - $RuCl$_3$: Doping and Magnetism". In: *Phys. Rev. Lett.* 124 (10 2020), p. 106804.

[84] Daniel Weber et al. "Magnetic Properties of Restacked 2D Spin $\frac{1}{2}$ honeycomb RuCl$_3$ Nanosheets". In: *Nano Lett.* 16.6 (2016). PMID: 27176463, pp. 3578–3584.

[85] Boyi Zhou et al. "Evidence for charge transfer and proximate magnetism in graphene–$\alpha-$RuCl$_3$ heterostructures". In: *Phys. Rev. B* 100 (16 2019), p. 165426.

[86] Soudabeh Mashhadi et al. "Spin-Split Band Hybridization in Graphene Proximitized with α-RuCl3 Nanosheets". In: *Nano Lett.* 19.7 (2019), pp. 4659–4665.

[87] Yiping Wang et al. "Modulation Doping via a 2d Atomic Crystalline Acceptor". In: (July 13, 2020). arXiv: 2007.06603v2.

[88] R. Balian and N. R. Werthamer. "Superconductivity with Pairs in a Relative *p* Wave". In: *Phys. Rev.* 131 (4 1963), pp. 1553–1564.

[89] Mark H Fischer. "Gap symmetry and stability analysis in the multi-orbital Fe-based superconductors". In: *New J. Phys.* 15.7 (2013), p. 073006.

[90] Annica M. Black-Schaffer and Sebastian Doniach. "Resonating Valence Bonds and Mean-Field *d*-Wave Superconductivity in Graphite". In: *Phys. Rev. B* 75 (13 2007), p. 134512.

[91] Tomas Löthman and Annica M. Black-Schaffer. "Defects in the $d+id$-Wave Superconducting State in Heavily Doped Graphene". In: *Phys. Rev. B* 90 (22 2014), p. 224504.

[92] Oladunjoye A. Awoga, Adrien Bouhon, and Annica M. Black-Schaffer. "Domain walls in a chiral *d*-wave superconductor on the honeycomb lattice". In: *Phys. Rev. B* 96 (1 2017), p. 014521.

[93] Atsuo Shitade et al. "Quantum Spin Hall Effect in a Transition Metal Oxide Na$_2$IrO$_3$". In: *Phys. Rev. Lett.* 102 (25 2009), p. 256403.

[94] I. I. Mazin et al. "Na$_2$IrO$_3$ as a Molecular Crystal". In: *Phys. Rev. Lett.* 109 (19 2012), p. 197201.

[95] Kateryna Foyevtsova et al. "Ab Initio Analysis of the Tight-Binding Parameters and Magnetic Interactions in Na$_2$IrO$_3$". In: *Phys. Rev. B* 88 (3 2013), p. 035107.

[96] Eric Kin-Ho Lee et al. "Topological and Magnetic Phases with Strong Spin-Orbit Coupling on the Hyperhoneycomb Lattice". In: *Phys. Rev. B* 89 (20 2014), p. 205132.

[97] Mildred S. Dresselhaus, Gene Dresselhaus, and Ado Jorio. *Group Theory*. Springer Berlin Heidelberg, 2008.

[98] Enberg, Rikard and Araujo, Moyses. *Symmetry and Group Theory*. Uppsala University Lecture Series. 2015.

[99] Andrei Bernevig and Titus Neupert. "Topological Superconductors and Category Theory". In: (June 18, 2015). arXiv: 1506.05805v2.

[100] Annica M. Black-Schaffer. "Edge Properties and Majorana Fermions in the Proposed Chiral *d*-Wave Superconducting State of Doped Graphene". In: *Phys. Rev. Lett.* 109 (19 2012), p. 197001.

[101] Liang Fu. "Odd-parity topological superconductor with nematic order: Application to $Cu_xBi_2Se_3$". In: *Phys. Rev. B* 90 (10 2014), p. 100509.

[102] Titus Neupert and Frank Schindler. "Lecture Notes on Topological Crystalline Insulators". In: (Oct. 8, 2018). arXiv: 1810.03484v1.

[103] Alexei Kitaev. "Periodic table for topological insulators and superconductors". In: *AIP Conf. Proc.* 1134.1 (2009), pp. 22–30.

[104] Shinsei Ryu et al. "Topological insulators and superconductors: tenfold way and dimensional hierarchy". In: *New J. Phys.* 12.6 (2010), p. 065010.

[105] Alexander Altland and Martin R. Zirnbauer. "Nonstandard symmetry classes in mesoscopic normal-superconducting hybrid structures". In: *Phys. Rev. B* 55 (2 1997), pp. 1142–1161.

[106] D. N. Sheng et al. "Quantum Spin-Hall Effect and Topologically Invariant Chern Numbers". In: *Phys. Rev. Lett.* 97 (3 2006), p. 036808.

[107] Xiao-Liang Qi, Taylor L. Hughes, and Shou-Cheng Zhang. "Topological field theory of time-reversal invariant insulators". In: *Phys. Rev. B* 78 (19 2008), p. 195424.

[108] Takahiro Fukui, Yasuhiro Hatsugai, and Hiroshi Suzuki. "Chern Numbers in Discretized Brillouin Zone: Efficient Method of Computing (Spin) Hall Conductances". In: *J. Phys. Soc. Jpn.* 74.6 (2005), pp. 1674–1677.

[109] Takahiro Fukui and Yasuhiro Hatsugai. "Quantum Spin Hall Effect in Three Dimensional Materials: Lattice Computation of $\mathbb{Z}_2$ Topological Invariants and Its Application to Bi and Sb". In: *J. Phys. Soc. Jpn.* 76.5 (2007), p. 053702.

[110] Masatoshi Sato. "Topological Properties of Spin-Triplet Superconductors and Fermi Surface Topology in the Normal State". In: *Phys. Rev. B* 79 (21 2009), p. 214526.

[111] Masatoshi Sato. "Topological Odd-Parity Superconductors". In: *Phys. Rev. B* 81 (22 2010), p. 220504.

[112] Seishiro Ono, Youichi Yanase, and Haruki Watanabe. "Symmetry indicators for topological superconductors". In: *Phys. Rev. Research* 1 (1 2019), p. 013012.

[113] Anastasiia Skurativska, Titus Neupert, and Mark H. Fischer. "Atomic limit and inversion-symmetry indicators for topological superconductors". In: *Phys. Rev. Research* 2 (1 2020), p. 013064.

[114] Max Geier, Piet W. Brouwer, and Luka Trifunovic. "Symmetry-based indicators for topological Bogoliubov–de Gennes Hamiltonians". In: *Phys. Rev. B* 101 (24 2020), p. 245128.

[115] Seishiro Ono, Hoi Chun Po, and Haruki Watanabe. "Refined symmetry indicators for topological superconductors in all space groups". In: *Sci. Adv.* 6.18 (2020), eaaz8367.

[116] Adrien Bouhon, Johann Schmidt, and Annica M. Black-Schaffer. "Topological nodal superconducting phases and topological phase transition in the hyperhoneycomb lattice". In: *Phys. Rev. B* 97 (10 2018), p. 104508.

[117] G. E. Volovik. "On edge states in superconductors with time inversion symmetry breaking". In: *JETP Lett.* 66.7 (1997), pp. 522–527.

[118] N. Read and Dmitry Green. "Paired states of fermions in two dimensions with breaking of parity and time-reversal symmetries and the fractional quantum Hall effect". In: *Phys. Rev. B* 61 (15 2000), pp. 10267–10297.

[119] A Yu Kitaev. "Unpaired Majorana fermions in quantum wires". In: *Physics-Uspekhi* 44.10S (2001), pp. 131–136.

[120] S. Nadj-Perge et al. "Observation of Majorana fermions in ferromagnetic atomic chains on a superconductor". In: *Science* 346.6209 (2014), pp. 602–607.

[121] Jason Alicea. "New directions in the pursuit of Majorana fermions in solid state systems". In: *Rep. Prog. Phys.* 75.7 (2012), p. 076501.

[122] Ramon Aguado. "Majorana quasiparticles in condensed matter". In: *Riv. del Nuovo Cim.* 40.11 (2017), pp. 523–593.

[123] Alexander Balatsky and Elihu Abrahams. "New class of singlet superconductors which break the time reversal and parity". In: *Phys. Rev. B* 45 (22 1992), pp. 13125–13128.

[124] P. Coleman, E. Miranda, and A. Tsvelik. "Odd-frequency pairing in the Kondo lattice". In: *Phys. Rev. B* 49 (13 1994), pp. 8955–8982.

[125] Elihu Abrahams et al. "Properties of odd-gap superconductors". In: *Phys. Rev. B* 52 (2 1995), pp. 1271–1278.

[126] Christopher Triola and Annica M. Black-Schaffer. "Odd-frequency pairing and Kerr effect in the heavy-fermion superconductor UPt_3". In: *Phys. Rev. B* 97 (6 2018), p. 064505.

[127] L. Komendová and A. M. Black-Schaffer. "Odd-Frequency Superconductivity in Sr_2RuO_4 Measured by Kerr Rotation". In: *Phys. Rev. Lett.* 119 (8 2017), p. 087001.

[128] Dushko Kuzmanovski and Annica M. Black-Schaffer. "Multiple odd-frequency superconducting states in buckled quantum spin Hall insulators with time-reversal symmetry". In: *Phys. Rev. B* 96 (17 2017), p. 174509.

[129] Haijun Zhang et al. "Topological insulators in Bi_2Se_3, Bi_2Te_3 and Sb_2Te_3 with a single Dirac cone on the surface". In: *Nat. Phys.* 5.6 (2009), pp. 438–442.

[130] Y. Xia et al. "Observation of a large-gap topological-insulator class with a single Dirac cone on the surface". In: *Nat. Phys.* 5.6 (2009), pp. 398–402.

[131] Zhongheng Liu et al. "Superconductivity with Topological Surface State in SrxBi2Se3". In: *J. Am. Chem. Soc.* 137.33 (2015), pp. 10512–10515.

[132] Yunsheng Qiu et al. "Time reversal symmetry breaking superconductivity in topological materials". In: (Dec. 11, 2015). arXiv: `1512.03519v1`.

[133] Shingo Yonezawa et al. "Thermodynamic evidence for nematic superconductivity in $Cu_xBi_2Se_3$". In: *Nat. Phys.* 13.2 (2016), pp. 123–126.

[134] Y. Pan et al. "Rotational symmetry breaking in the topological superconductor $Sr_xBi_2Se_3$ probed by upper-critical field experiments". In: *Sci. Rep.* 6.1 (2016).

[135] Tomoya Asaba et al. "Rotational Symmetry Breaking in a Trigonal Superconductor Nb-doped Bi_2Se_3". In: *Phys. Rev. X* 7 (1 2017), p. 011009.

[136] Jörn W. F. Venderbos, Vladyslav Kozii, and Liang Fu. "Odd-parity superconductors with two-component order parameters: Nematic and chiral, full gap, and Majorana node". In: *Phys. Rev. B* 94 (18 2016), p. 180504.

[137] E. Lahoud et al. "Evolution of the Fermi surface of a doped topological insulator with carrier concentration". In: *Phys. Rev. B* 88.19 (2013), p. 195107.

[138] G. Rosenberg and M. Franz. "Surface magnetic ordering in topological insulators with bulk magnetic dopants". In: *Phys. Rev. B* 85 (19 2012), p. 195119.

[139] Annica M. Black-Schaffer and Alexander V. Balatsky. "Proximity-induced unconventional superconductivity in topological insulators". In: *Phys. Rev. B* 87 (22 2013), p. 220506.

[140] Ran Tao et al. "Direct Visualization of the Nematic Superconductivity in $Cu_xBi_2Se_3$". In: *Phys. Rev. X* 8 (4 2018), p. 041024.

[141] D. J. Scalapino, S. R. White, and S. C. Zhang. "Superfluid density and the Drude weight of the Hubbard model". In: *Phys. Rev. Lett.* 68 (18 1992), pp. 2830–2833.

[142] Jonas A. Krieger et al. "Proximity-Induced Odd-Frequency Superconductivity in a Topological Insulator". In: *Phys. Rev. Lett.* 125 (2 2020), p. 026802.

[143] R. Heid. "On the thermodynamic stability of odd-frequency superconductors". In: *Z. Phys. B* 99.1 (Mar. 1995), pp. 15–18.

[144] Long Liang et al. "Band geometry, Berry curvature, and superfluid weight". In: *Phys. Rev. B* 95 (2 2017), p. 024515.

[145] N. B. Kopnin and E. B. Sonin. "BCS Superconductivity of Dirac Electrons in Graphene Layers". In: *Phys. Rev. Lett.* 100 (24 2008), p. 246808.

[146] Tomonari Mizoguchi and Masao Ogata. "Meissner Effect of Dirac Electrons in Superconducting State Due to Inter-Band Effect". In: *J. Phys. Soc. Jpn* 84.8 (2015), p. 084704.

Acta Universitatis Upsaliensis

Digital Comprehensive Summaries of Uppsala Dissertations from the Faculty of Science and Technology 1973

Editor: The Dean of the Faculty of Science and Technology

A doctoral dissertation from the Faculty of Science and Technology, Uppsala University, is usually a summary of a number of papers. A few copies of the complete dissertation are kept at major Swedish research libraries, while the summary alone is distributed internationally through the series Digital Comprehensive Summaries of Uppsala Dissertations from the Faculty of Science and Technology. (Prior to January, 2005, the series was published under the title "Comprehensive Summaries of Uppsala Dissertations from the Faculty of Science and Technology".)

ACTA
UNIVERSITATIS
UPSALIENSIS
UPPSALA
2020